

EFFECT OF VANADIUM ON FRACTURE OF DP1300 STEELS

**EFFECT OF VANADIUM ADDITION ON DEFORMATION AND FRACTURE
BEHAVIOR OF DP1300 DUAL PHASE STEELS**

By LINFENG ZHOU, B. ENG.

A Thesis Submitted to the School of Graduate Studies in Partial Fulfillment of the
Requirement for the Degree Master of Applied Science

McMaster University @ Copyright by Linfeng Zhou. April 2018

Master of Applied Science (2018)
(Materials Science and Engineering)

McMaster University
Hamilton, Ontario, Canada

TITLE: Effect of Vanadium Addition on
Deformation and Fracture Behavior of
DP1300 Dual Phase Steels

AUTHOR: Linfeng Zhou, B. Eng. (McMaster
University)

SUPERVISOR: Dr. David S. Wilkinson
Dr. Jidong Kang

NUMBER OF PAGES: xv,138

Abstract

Advanced high strength steel (AHSS) provides a lightweight material solution in response to the stringent regulation on fuel economy and greenhouse gas emissions in the automotive industry. Dual phase (DP) steels that consist of a hard martensite phase embedded in a soft ferrite matrix are the most widely used AHSS due to their simple microstructure, robust thermo-mechanical processing and attractive mechanical properties. However, DP steels are prone to deform heterogeneously with strong strain partitioning between phases. The addition of Vanadium in DP steels can form nano-precipitates of vanadium carbonitrides (V (C,N)) that strengthen the ferrite and thus reduce the strain partitioning. This study considered the influence of V (C,N) on the deformation and damage behavior of ferrite-martensite DP1300 steels at the microscopic level. The hardness of the embedded ferrite and martensite regions are determined through nano-hardness testing. In-situ uniaxial tension tests were conducted on DP steels with similar martensite volume fractions within a scanning electron microscope (SEM) chamber. Microscopic-digital image correlation (μ DIC) was then employed to analyze the local strain partitioning between ferrite and martensite. Local damage events such as void formation at ferrite martensite island interfaces and in the martensite islands were observed and rationalized with the μ DIC results. X-ray computed tomography (XCT) were conducted to quantitatively analyze the microstructure damage.

It was found that vanadium addition helps refine the microstructure and improve mechanical compatibility between the two phases. The overall ductility of the steel is enhanced especially in terms of post-uniform elongation and true strain to fracture.

Acknowledgements

Firstly, I would like to express my sincere gratitude to both my supervisors Dr. David Wilkinson and Dr. Jidong Kang for their invaluable guidance and generous support for my research. Their knowledge and expertise always enlighten me for deeper understanding of my project.

I would also like to express my thanks to Dr. Javad Samei to who performed the nano-indentation and X-ray CT scans. I learned a lot from the fruitful discussions about my experiments and data analysis.

I also appreciate the assistance of all the following people very much:

- Mr. Chris Butcher for metallography and SEM training at Canadian Centre for Electron Microscopy
- Dr. Mike Bruhis and Dr. Anantheshwara Kommunje for mechanical testing and ARAMIS software operation
- Mrs. Connie Barry and Dr. Elizabeth McNally for their help in the lab at McMaster Automotive Research Center
- Mr. Andy M. Duft for assistance of tensile stage maintenance
- Dr. Xiaogang Li and Mr. Doug Culley for their help in the MSE labs
- Dr. Collin Scott at CanmetMATERIALS for providing the sheet materials used in this study
- Dr. Babak Shalchi-Amirkhiz at CanmetMATERIALS for performing TEM experiments.
- Dr. Waqas Muhammad for performing mechanical testing at CanmetMATERIALS.
- Mr. Jim Cleaver at the Faculty of Engineering machine shop and Mr. Jean-Paul Talon at CanmetMATERIALS for machining samples
- Mr. Ed McCaffery for solving my computer problems

My sincere thanks also go to my friends: Zhulin Xu, Madhumanti Bhattacharyya,

Yicheng Chen, Michelia Alba, Khaled Abu Samk, He Ming. Finally, the support and blessing from my family are very appreciated.

Table of Content

Abstract	iv
Acknowledgements	v
Table of Content	vii
List of Figures	ix
List of Tables	xiii
List of symbols	xiv
1 Introduction	1
1.1 Background	1
1.2 Objectives and Thesis Outline	2
2 Literature Review	4
2.1 Dual phase Steels	4
2.1.1 Introduction	4
2.1.2 Processing Methods	4
2.1.3 Alloying Elements in DP steels	6
2.1.4 Mechanical Behaviour of DP steels	8
2.2 Grain Refinement of BCC Steels	34
2.2.1 Methods of Producing Ultrafine-grained (UFG) Steels	34
2.2.2 Microstructure Characterization of Ultrafine-grained (UFG) Steels	35
2.2.3 Mechanical Properties of Ultrafine-grained (UFG) Steels	36
2.3 Two Dimensional (2D) Digital Image Correlation (DIC)	37
2.3.1 Brief Introduction of Full-field Optical Methods	37
2.3.2 Digital Image Correlation Method	39
3 Materials Processing	57
4 Experimental Procedure	59
4.1 Metallography	59
4.2 Transmission Electron Microscopy (TEM)	59
4.3 DIC Tensile Test	60
4.3.1 Macroscopic uniaxial DIC Tensile Tests	60
4.3.2 Microscopic In-situ Tensile Tests through Scanning Electron Microscope (SEM)	61

4.4 Fractography	66
4.5 Quantitative Methods	66
4.5.1 Microstructural Analysis	66
4.5.2 Nano-hardness Measurements	68
4.5.3 Strain Analysis of In-situ Tensile Test Coupled with SEM	69
4.5.4 X-ray Computed Tomography (X-ray CT) Scans	69
5 Results and Discussion	71
5.1 Microstructures	71
5.2 Macroscopic Stress-strain Behaviour	78
5.3 Nano-indentation Study	84
5.3.1 Nano-hardness of Ferrite	85
5.3.2 Nano-hardness of Martensite	87
5.4 Microstructure Evolution during In-situ Tensile Test	89
5.4.1 SEM Selection	89
5.4.2 Strain Analysis	91
5.5 Micro-mechanisms of damage	112
5.5.1 Microscopic deformation characterization	112
5.5.2 Correlation between microscopic and macroscopic deformation	121
5.6 Fracture Surface analysis	121
5.6.1 Fractography	122
5.6.2 X-ray Computed Tomography (XCT) Scans	123
6 Conclusions	129
Reference	130

List of Figures

Figure 1-1 Steel strength-ductility diagram. Abbreviations: AHSS: advanced high strength steel; BH: bake hardened; CP: complex phase; DP: dual phase; FB: ferritic bainitic; HF: hot formed (and quenched); HS: high speed; HSLA: high-strength, low-alloy; IF: interstitial free; MS: martensitic; TRIP: transformation-induced plasticity; TWIP: twinning-induced plasticity. [3]	1
Figure 2-1 Schematic diagram indicating processing methods to produce α/α' DP steels. Abbreviations: A : austenite; F : ferrite; M : martensite; A_{C1} : the temperature when austenite begins to form during heating; A_{C3} : the temperature when the transformation of ferrite to austenite is completed during heating. (A_{C1} and A_{C3} depend on alloy chemistry.) [4]	4
Figure 2-2 Schematic representations of the microstructures for an iron-carbon alloy of hypo-eutectoid composition in different phase region in $Fe - Fe_3C$ phase diagram. (A_{C1} : the temperature when austenite begins to form during heating) [12]	6
Figure 2-3 Solubilities of microalloy carbides and nitrides in austenite [14].....	7
Figure 2-4 Schematic quasi-static tensile stress-strain curves at similar ultimate tensile strength levels for pearlite-ferrite steel, HSLA steel, DP steel, TRIP steel, and TWIP steel. Abbreviations: HSLA: high-strength, low-alloy; TRIP: transformation-induced plasticity; TWIP: twinning-induced plasticity. [4].....	9
Figure 2-5 Schematic plot showing the intersection of the true stress-strain curve and strain-hardening curve that defines the mechanical instability or necking condition during tensile testing [25].	12
Figure 2-6 Schematic illustration of diffuse necking and localized necking of a thin strip [28].....	14
Figure 2-7 Crystal structure of the body-centered tetragonal unit cell and octahedral interstitial sites of carbon of martensite in iron-carbon alloys and carbon steels [25]	15
Figure 2-8 Effect of carbon content on M_s in iron-carbon alloys [25].....	16
Figure 2-9 hardness of martensite microstructure as a function of carbon content [29]	16
Figure 2-10 Different morphologies of martensite with similar martensite volume fraction obtained from varied heat treatment. (a) Laths of martensite; (b) Grain boundary growth; (c) Bulk growth [27].....	17
Figure 2-11 Effect of volume fraction of martensite on YS of Cr-Mn-Si-B steel with varied carbon content quenched from 760 to 820°C [20]	18

Figure 2-12 Effect of Mn and C concentration in steels on the YS/UTS ratio depending on the ultimate tensile strength of steel (after water quenching from different temperatures): (a) the effect of Mn in steel with ~0.08% C; (b) the effect of C in steel with ~1.5% Mn [30].....	20
Figure 2-13 Effects of the volume fraction of martensite on the ultimate tensile strength of DP CrMnSiB steels with different carbon content: dashed lines correspond to calculations using rules of mixtures. (A-0.18% C; B-0.10% C; C: 0.07% C) [31] 21	21
Figure 2-14 Relationship between work hardening rate at strain $\epsilon_{pl} = 0.20$, and the size of martensite particles. f_v and λ_{M-A} refer to the volume fraction and average particle diameter of the martensite-austenite (M-A) constituent, respectively [35]	24
Figure 2-15 Effect of martensite volume fraction on the uniform elongation and total elongation of DP steels [37].....	25
Figure 2-16 Grain size dependence of yield and tensile strength. (MVF represents volume fraction of martensite) [39]	27
Figure 2-17 Grain size dependence of uniform and total elongation. (MVF represents volume fraction of martensite) [39]	28
Figure 2-18 Cleavage fracture surface showing the segmentation of the cleavage crack front into four facets separated by risers in the grain [42].....	30
Figure 2-19 Dimpled fracture surface of ultra-fine grained IF steel [42]	31
Figure 2-20 Schematic representation of two types modes if ductile failure (a) by micro-voids coalescence; (b) by plastic instability [42]	31
Figure 2-21 Process of micro-void coalescence failure corresponding to the macroscopic mechanical response [43]	32
Figure 2-22 A summary of void nucleation mechanism for DP steel [4]	33
Figure 2-23 Grain size dependence of ductility for bcc steels [44]	36
Figure 2-24 Typical optical image acquisition system for the 2D DIC method [50]...	40
Figure 2-25 Comparison between specimens with different stochastic pattern [55]...	41
Figure 2-26 The default facet (15x15 pixels) with a facet step of 13 pixels corresponding to 2 pixels overlapping area [55].....	43
Figure 2-27 Facets in the undeformed and the deformed state [50]	44
Figure 2-28 Matching of 3x3 facets [56]	49
Figure 2-29 Translation (\mathbf{u}) and strain of a line element [55]	50
Figure 2-30 Schematic of a typical SEM and imaging process [63]	55
Figure 2-31 Schematic of typical image formation process in a SEM [65].....	56
Figure 3-1 Schematic diagram of processing routes to produce DP steels in CANMET	58
Figure 4-1 Dimensions of micro-tensile specimen	60
Figure 4-2 Photos of micro-tensile specimen with stochastic pattern	61
Figure 4-3. Dimension of micro-tensile hourglass-shape test specimen	61

Figure 4-4 Strain distribution along the proposed specimen geometry through finite element analysis. The strain presented here is the von Mises effective strain (a) Reference steel, (b) Vanadium added steel	62
Figure 4-5 Micro-tensile specimens on automatic polishing jigs	63
Figure 4-6 SEM images showing micro-hardness indents on specimen surface.....	64
Figure 4-7 Manual tensile jig for in-situ tensile test coupled with SEM.....	65
Figure 4-8 Manual tensile jig in FE-SEM chamber.....	65
Figure 4-9 Optical image of the nano-indented region in both steels: (a) DP steels; (b) DPV steels.....	69
Figure 5-1 SEM micrographs of ferrite-martensite DP steels. (F: ferrite; M: martensite; ND: normal direction; RD: rolling direction)	72
Figure 5-2 SVEs in SEM micrographs	74
Figure 5-3 Martensite volume fraction distribution through sample thickness	75
Figure 5-4 TEM Bright field (BF) images	76
Figure 5-5 TEM observations, including HAADF images, EELS map of elements, and EDS spectrum.....	77
Figure 5-6 Images exported from ARAMIS software: (a) Specimen surface with mapping in project mode; (b) True strain map of DP-ref-RD-1	78
Figure 5-7 True stress v.s. strain curves of DP-ref and DP-V steels: (a) All of the materials; (b) DP-ref-RD; (c) DP-ref-TD; (d) DP-V-RD; (e) DP-V-TD	81
Figure 5-8 Plotting of the evolution of the work hardening against the true strain	82
Figure 5-9 Investigated DP steels mechanical properties overlapping with global formability diagram [3] (DP: V-free steel; DPV: V-added steel).....	84
Figure 5-10 Cumulative distribution of ferrite and martensite island hardness of both steels from nano-indentation measurements.	85
Figure 5-11 SEM images under similar resolution and strain maps of DP-V steels obtained from DIC analysis (a) Micrographs taken from JEOL JSM-7000, (b) Micrographs taken from JEOL 6610LV. (facet size x step size = 27x21 pixels).....	91
Figure 5-12 SEM images of heavily deformed or fractured micro-tensile specimens at low magnifications showing relative locations of micro-indents and image locations. (a) DP-ref along RD; (b) DP-V along RD; (c) DP-ref along TD; (b) DP-V along TD. Capital letters A-B represents locations where images were taken; Arabic numbers 1-13 represents locations of micro-indents. The selected regions to perform DIC are highlighted by boxes with a yellow outline	92
Figure 5-13 Engineering strain measurements of indents. Red dash line: strain measurements of two indents where the main crack went through; Blue dash line: strain measurements of two indents which are away from the fractured part.	93
Figure 5-14 Schematic drawing showing selected lines	96
Figure 5-15 Strain maps before and after interpolation	96
Figure 5-16 Strain measurements comparison.....	97
Figure 5-17 Schematic diagram showing the relationships between the micro-indents	

strain measurements and DIC average strain.....	98
Figure 5-18 Typical examples of the deformation of the steels: SEM images (left) and equivalent strain maps overlapping with microstructures.	100
Figure 5-19 DIC Effective strain ε measurements comparison	101
Figure 5-20 Equivalent strain maps comparison between steels along RD directions. The legend is set to be same for all the stages.	103
Figure 5-21 Cumulative equivalent strain distribution between ferrite and martensite for DP-ref and DP-V steels along RD directions.	105
Figure 5-22 Equivalent strain maps comparison between steels along TD directions. The legend is set to be same for all the stages	106
Figure 5-23 Cumulative equivalent strain distribution between ferrite and martensite for DP-ref and DP-V steels along TD directions.	108
Figure 5-24 Partitioned strain between ferrite and martensite phases (median value), as a function of local average strain. Both strain along tensile directions (ε_x) and the von Mises equivalent strain ($\bar{\varepsilon}$) are plotted.	111
Figure 5-25 Damage accumulation process. (1) DP-ref steels along RD; (2) DP-ref steels along TD; (3) DP-V steels along RD; (4) DP-V steels along TD. Yellow arrow: interfacial damage; red arrow: martensite cracking	116
Figure 5-26 Selected locations to magnify microstructural damage evolution. (a) DP-ref steel along RD direction at a magnification of x2700; (b) DP-V steel along RD direction at a magnification of x7500. The selected locations are heightened with blue boxes.	117
Figure 5-27 SEM images revealing damage development in steels. (1) DP-ref steels (2) DP-V steels.....	120
Figure 5-28 Fracture map for DP1300 along RD	121
Figure 5-29 Fracture surface of the DP-ref steel.	122
Figure 5-30 Fracture surface of the DP-V steels.....	123
Figure 5-31 3D representation of the population of dimples or voids in fractured samples of DP-ref steel (a) fracture surface, (b) dimples on the fracture surface in green, and (c) voids beneath the fracture surface in red. The 3D model is presented from varied views in the second row and 3D perspectives are shown in the third row.	124
Figure 5-32 3D representation of the population of dimples or voids in fractured samples of DP-V steel (a) fracture surface, (b) dimples on the fracture surface in green, and (c) voids beneath the fracture surface in red. The 3D model is presented from varied views in the second row and 3D perspectives are shown in the third row.	125
Figure 5-33 Quantitative analysis of voids in the necked area of the fractured samples obtained from XCT scans	128

List of Tables

Table 2-1 Summary of various full-field optical measurement techniques [49].....	38
Table 2-2 Influence of facet size and facet step on calculation in Aramis software [55]	43
Table 2-3 Commonly used correlation criterion [50].....	46
Table 2-4 Summary of patterning techniques for μ -DIC SEM [60]	54
Table 3-1 Chemical compositions of studied DP steels (in wt%)	57
Table 5-1 Microstructure parameters obtained from SEM micrographs	73
Table 5-2 V_M inside each SVE of DP-ref and DP-V steels.....	74
Table 5-3 Parameters setting in ARAMIS software for macroscopic tensile tests	79
Table 5-4 Mechanical properties of the steels.....	82
Table 5-5 Yield stress increment derived from Hall-Petch relationship	87
Table 5-6 Ferrite (α) and martensite (α') strengths obtained from nano-indentation measurements compared with the calculated hardness.....	89
Table 5-7 Parameters of microscopic strain calculation in ARAMIS	95
Table 5-8 Quantitative data for voids and dimples obtained from XCT scans	125

List of symbols

α	Ferrite
α'	Martensite
A_0	Tensile sample cross-sectional area before fracture
A_F	Tensile sample cross-sectional area before fracture area after fracture
% <i>RA</i>	Percent relative accuracy
<i>CI</i>	Confidence intervals
C_M	Carbon concentration in martensite
e	True strain
ε_e	Engineering strain
ε_F	True fracture strain
ε_u	Maximum uniform elongation
ε_T	True strain
H_n	Nano-hardness
H_v	Vickers hardness
M_s	Martensite start temperature
N	Number of measured grains
n	Number of observation fields
$\overline{P_P}$	Mean value of measured volume fraction
σ_e	Engineering stress
σ_u	True stress at maximum loading
σ_T	True stress
σ_y	Yield strength
$\sigma_{0.2}$	0.2% offset yield strength
RA	Reduction of cross-sectional area
s	Standard deviation
$\overline{S_F}$	Mean value of measured grain size

t	Confidence intervals interval multiplier
TE	Total elongation
UE	Uniform elongation
UST	Ultimate tensile strength
V_F	Volume fraction of ferrite
V_M	Volume fraction of martensite
YS	Yield strength

1 Introduction

1.1 Background

In order to reduce energy consumption and gas emission, there is a growing demand for the automotive industry to develop weight-reduced sheet metal components without losing the safety performance of vehicles [1]. Due to the combination of high strength and good ductility, modern advanced high strength steels (AHSS) are widely used in automotive industry for manufacturing of body-in-white (BIW) components [2]. Figure 1-1 demonstrates the broad range of properties of steels. The general trend for the development of steels is to move towards the upper right in the strength-ductility plot.

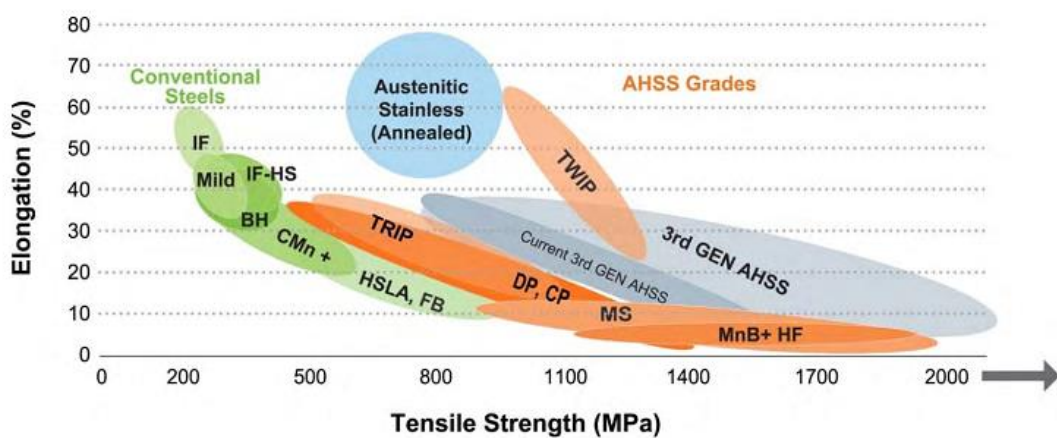


Figure 1-1 Steel strength-ductility diagram. Abbreviations: AHSS: advanced high strength steel; BH: bake hardened; CP: complex phase; DP: dual phase; FB: ferritic bainitic; HF: hot formed (and quenched); HS: high speed; HSLA: high-strength, low-alloy; IF: interstitial free; MS: martensitic; TRIP: transformation-induced plasticity; TWIP: twinning-induced plasticity. [3]

As one of the earliest developed and most important examples of AHSS, dual phase

(DP) steel has successfully gained considerable attention in recent years [4]. The thermomechanical processing of DP steels is relatively simple and involves lean alloying requirements, which makes DP steels stand out among AHSS. Ferrite-martensite (α/α') DP steels are composed of a soft ferrite matrix and hard martensite islands. The typical mechanical characteristics of α/α' DP steels include continuous yielding, high initial work-hardening rate, low initial yield stress, high ultimate tensile strength (UTS), and good ductility [5]–[7].

Grain refinement has been proved a promising method to strengthen DP steels without sacrificing ductility [8]. The addition of microalloying elements is one of the solutions to realize grain refinement of DP steels. Small additions of micro-alloying elements, such as Ti, V, Mo, and Nb in DP steels can strengthen the materials by several strengthening mechanisms, including grain refinement, solid solution, and precipitation hardening [9]. Compared to other microalloying elements, the solute drag ability of vanadium is relatively lower, which can facilitate austenite recrystallization. Hence the austenite recrystallization can be accomplished through the thickness of the slab during rolling [10].

Despite many studies having been performed on the microstructural characteristics and mechanical properties of DP steels in the last decade, systematic studies on the influence of vanadium addition on modifying the strain partitioning between ferrite and martensite of cold-rolled ultrafine-grained (UFG) α/α' DP steels have not yet been done. In the present work, a reference steel with 0.003 wt. % V and a Vanadium added steel 0.14 wt. % V are investigated.

1.2 Objectives and Thesis Outline

The objective of the present study is to develop a good understanding of the impact of Vanadium addition on microstructural evolutions, mechanical properties, deformation, and damage behavior of UFG α/α' DP1300 steels. In-situ uniaxial tensile tests are

performed within a scanning electron microscope (SEM) chamber coupled with microscopic-digital image correlation (μ DIC) for strain analysis.

The layout of the thesis is as follows. Chapter 1 introduces the background information and objectives of the research. Chapter 2 presents a review of the microstructure and mechanical properties of DP steels. Also, relevant damage and failure studies on DP steels are described. Finally, there is a brief review of digital image correlation (DIC) technique used for strain analysis. The materials processing procedure provided by CanmetMATERIALS is presented in Chapter 3. Chapter 4 describes the experimental procedures used in this work. The experimental results, including tensile data, microstructure analysis and fracture characterization and related discussion are shown in Chapter 5. The conclusions arising from the current study are presented in Chapter 6.

2 Literature Review

2.1 Dual phase Steels

2.1.1 Introduction

Dual phase (DP) steels have been used in the automotive industry since the 1970s due to the unique combination of strength and ductility [11]. DP steels are characterized by a microstructure composed of hard martensite islands dispersed in a soft, ductile ferrite matrix. However, DP steels usually contain more than two phases suggested by their name. Retained austenite, pearlite, and bainite also might be present in DP steels [5].

2.1.2 Processing Methods

As illustrated in Figure 2-1, there are mainly two basic heat treatment approaches to produce α/α' DP steels, which can generate different microstructures and properties.

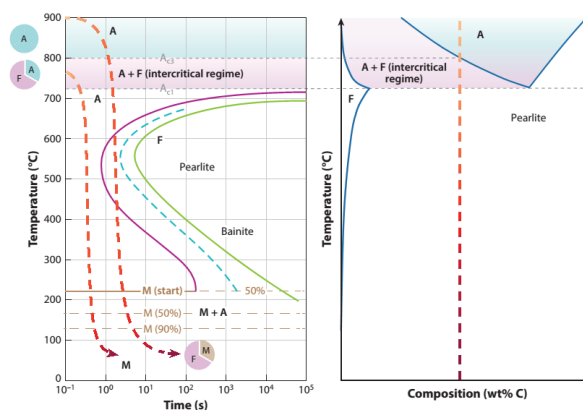


Figure 2-1 Schematic diagram indicating processing methods to produce α/α' DP steels. Abbreviations: A : austenite; F : ferrite; M : martensite; A_{C1} : the temperature when austenite begins to form during heating; A_{C3} : the temperature when the transformation of ferrite to austenite is completed during heating. (A_{C1} and A_{C3} depend on alloy chemistry.) [4]

The first method refers to cooling the hot-rolled steels from the fully austenitic regime by selecting an appropriate quenching rate, to enable most of the undercooled austenite to transform to ferrite and the rest to become martensite.

Another method is called intercritical annealing. During this process, the initial cold-rolled ferrite-pearlite or ferrite-bainite microstructure is reheated into the range of intercritical annealing, followed by quenching below the martensite start temperature (M_s) [4].

Because the transformation starts in the ferrite-austenite ($\alpha+\gamma$) region, intercritical annealing makes it easier to control the volume fraction of martensite (V_M). Once the steel is heated above the temperature when austenite begins to form (A_{C1}), non-equilibrium austenite forms at the carbide locations. The carbon content and volume fraction of austenite are determined by the intercritical temperature. When sufficient time is given at the intercritical temperature, the austenite nuclei grow until the equilibrium composition is reached and the volume fraction of austenite can be determined by the lever rule [5]. The austenite will transform to martensite after quenching. Figure 2-2 schematically presents varied microstructures at different temperatures. According to the phase diagram, at higher intercritical annealing temperature, there is higher volume fraction of austenite and lower carbon content in austenite. Similarly, the carbon content in ferrite is lower at higher intercritical temperature. Therefore, the volume fraction of martensite (V_M) in DP steels can be controlled by adjusting the intercritical temperature during production.

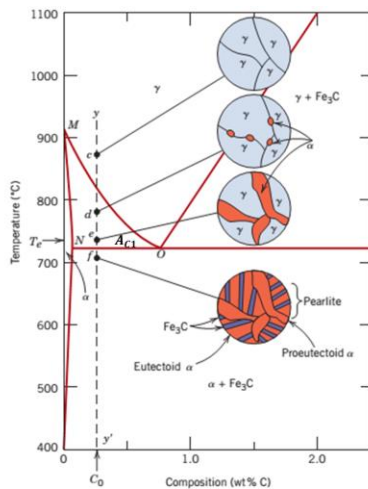


Figure 2-2 Schematic representations of the microstructures for an iron-carbon alloy of hypo-eutectoid composition in different phase region in $Fe - Fe_3C$ phase diagram.

(A_{C1} : the temperature when austenite begins to form during heating) [12]

2.1.3 Alloying Elements in DP steels

To achieve the desired microstructures, several alloying elements are added in DP steels, including V, N, Mn, Si, Al, Mo, and Cr.

2.1.3.1 Vanadium

Vanadium has a body cubic centered (BCC) crystal structure and is a strong ferrite stabilizer. However, it has a high affinity for carbon and nitrogen, resulting in forming of face cubic centered (FCC) NaCl cubic crystal structure carbide, nitride and carbonitrides (V(C, N)), which exhibit solubility both in austenite and ferrite [13].

Ti, Nb, and V can all strengthen steels by several mechanisms, such as precipitation hardening, solid solution, and grain refinement. Compared with Ti and Nb, vanadium enjoys a higher solubility of carbonitrides in austenite even at temperatures as low as 1050 °C (Figure 2-3) There are lots of benefits generated from high solubility of V(C, N) in the steel making process, including superior castability with minimal cracking, reduced reheat temperature requirements, and predictable strengthening over a large

alloy range. The high solubility of V(C, N) results in little or no precipitation at grain boundaries after solidification and thus crack sensitivity is minimized.

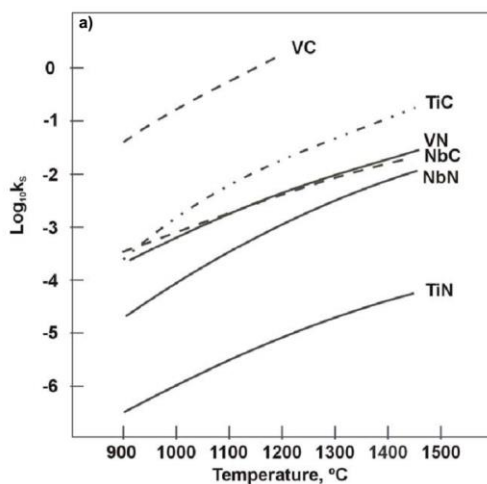


Figure 2-3 Solubilities of microalloy carbides and nitrides in austenite [14]

Vanadium presents a relatively low solute drag coefficient compared to other microalloying elements, which promotes the recovery and recrystallization of austenite during rolling. As a result, more uniform austenite grains in size from the surface to center are generated and thus more uniform mechanical properties are obtained. In addition, due to the high solubility of V(C, N) and small solute drag effect, vanadium steels are rarely found to recrystallize during rolling, and thus a gradual refinement of austenite and the subsequent ferrite microstructure is formed. Figure 2-3 also shows that the solubility of vanadium carbides in austenite is much greater than vanadium nitrides. Therefore, as a cost-effective element, nitrogen can enhance the driving force for precipitation in V-microalloyed steels and it changes from an undesired element to an essential part of the alloy system. In addition, the preferred precipitation with nitrogen reduces the risk of nitrogen strain aging. However, in the steel with Al present, coarse AlN precipitates tends to form, so Al content should be minimized (less than 0.03 wt.%).

V(C, N) can precipitate from austenite grain boundaries or pre-existing particles in the austenite (MnS). The precipitation of V(C, N) provides a proper condition for intragranular ferrite grains nucleation, which results in a very significant ferrite grain refinement [14]–[16].

Furthermore, hydrogen trapping behavior by VC, investigated by Asahi et al. [17], helps to improve the delayed fracture resistance of steel. According to He et al. [18], vanadium addition can promote acicular ferrite microstructure formation and thus improve toughness.

2.1.3.2 Other alloying elements

Carbon is known as an austenite stabilizer and it is capable of strengthening martensite and determining the phase distribution. Manganese also stabilizes austenite, and promotes high hardenability. Manganese is a solid solution strengthener of ferrite and it can suppress ferrite formation. Silicon can accelerate carbon migration from ferrite to the austenite and thus it helps facilitate ferritic transformation. It can also retard the pearlite transformation [19], [20]. As a ferrite-forming element, aluminum can suppress the pearlite transformation and enhance the hardenability. Molybdenum and chromium are known to promote the hardenability of austenite by retarding the pearlite and lowering the bainite transformation temperature [19].

2.1.4 Mechanical Behaviour of DP steels

α/α' DP steels present a series of unique mechanical properties in comparison to those of other steels. As shown in Figure 2-4, DP steels exhibit early and continuous yielding (no sharp yield point), high initial hardening rate, a low yield strength to ultimate tensile strength (YS/UTS) ratio, superior strength, and high uniform and total elongation; also Lüders bands are absent.

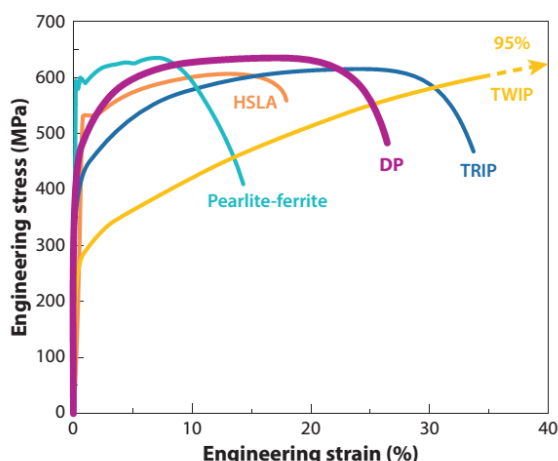


Figure 2-4 Schematic quasi-static tensile stress-strain curves at similar ultimate tensile strength levels for pearlite-ferrite steel, HSLA steel, DP steel, TRIP steel, and TWIP steel. Abbreviations: HSLA: high-strength, low-alloy; TRIP: transformation-induced plasticity; TWIP: twinning-induced plasticity. [4]

The combination of early-stage yielding and high strain hardening allows DP steels to provide excellent sheet-forming and component performance properties for components applied in automotive industries. All of those mechanical properties characteristics of α/α' DP steels come from the deformation behaviour of microconstituents in α/α' DP steels. There are many microstructure parameters which can affect the mechanical properties of DP steels, including martensite volume fraction (V_M), martensite grain size, martensite carbon content, martensite/ferrite morphology, ferrite grain size, ferrite texture, density of transformation-induced geometrically necessary dislocations (GNDs), micro- and mesoscale segregations, and the mechanical behaviour of DP steels [4].

Numerous studies have been performed to understand how those parameters influence mechanical properties of α/α' DP steels. However, due to varied processing conditions of DP steels, for example, hot rolling finishing and coiling temperatures, cold

reductions, temperature and holding time of annealing, heating/cooling rates, etc., it is difficult to summarize the existing research data [20].

2.1.4.1 Strengthening Mechanisms in DP Steels

There are numerous mechanisms which contribute to strengthening of DP steels, including: hard martensite particles strengthening, solid solution strengthening of martensite by carbon atoms, solid solution strengthening of ferrite, strengthening of ferrite by grain boundaries, precipitation hardening of ferrite, and strain aging. The influence of those mechanisms on DP steels is complex. The detailed description illustrating how they evolve during deformation can be illustrated as follows:

1. The strength of α/α' DP steels is fundamentally determined by the distributions of stresses and strains between ferrite and martensite. Any factors which can affect the distribution of martensite (e.g. martensite geometry) are responsible for the hardening role of martensite, including the ratio of martensite and ferrite strengths, martensite phase continuity, and the total deformation of the steel.
2. The two phases in α/α' DP steels tend to interact with each other and they behave differently from those in the single-phase conditions. Koo et al. found that α' in a DP steel has lower hardness in comparison of those of 100% α' and the strength of α in DP steels is higher than ferritic steels of the same composition in cases where the second phase particles (martensite islands) are spaced at distances less than the mean dislocation slip length [21].
3. The residual stress introduced by austenite-to-martensite transformation exerts enormous influence on the properties of DP steels. The magnitude of residual stresses is determined by V_M , the carbon content of α' which determines martensite start temperature (M_s), and the cooling rate from M_s to room temperature, which determines the possible extent of relaxation of the residual

stresses [20].

It should be noted that alterations in microstructure or intercritical annealing conditions tend to result in simultaneous changes in many microstructural parameters and phase properties of DP steels. For instance, according to the phase diagram depicted in Figure 2-2, raising the intercritical annealing temperature will reduce the strength of α' by reducing C_M and the strength of ferrite by decreasing interstitial concentrations. Precipitation hardening of ferrite by carbides usually cause a decrease in V_M and/or a drop in C_M , because some of the carbon atoms are tied up in carbides [20].

More in-depth analysis of the influence of martensite and ferrite on strength properties will be elaborated in 2.1.4.3 and 2.1.4.4, respectively.

2.1.4.2 Strain Hardening of DP Steels

DP steels present a relatively high work hardening rate compared to other low-alloy steels. The low initial yield strength helps cold forming. The high strain-hardening rate allows high uniform elongation and guarantees an increase in strength during deformation. To optimize the microstructures of DP steels, it is important to understand the factors influencing strain-hardening behaviors.

Several theoretical models based on various constitutive equations are used to analyze the strain-hardening behaviors of DP steels. The most common methods are the Hollomon analysis, the Crussard–Jaoul (C-J) analysis, and the modified C-J analysis, which are based on the Hollomon equation, the Ludwik equation, and the Swift equation, respectively [22]. Unlike most cases, the deformation behavior of DP steels usually cannot be fitted by a simple parabolic function over the uniform strain range. The stress-strain curve of DP steels can be divided into as many as three stages and each of them can be described by a different n value. The number of stages depends

on microstructural parameters of DP steels.

Theoretical Models

The Hollomon equation ($\sigma = k\varepsilon^n$) is the most commonly used constitutive equations to describe a single stage of strain hardening behavior.

During a uniaxial tensile test, when the increase in the load-carrying ability of the metal due to strain hardening is no longer be able to compensate for the increase in stress due to the decrease in the cross-section area of the specimen, necking is initiated, and plastic instability develops. Necking instability occurs at the intersection of the strain-hardening and strengthening curves as a function of strain (Figure 2-5) [23]. The work hardening rate is described as $\frac{d\sigma}{d\varepsilon}$ [24]. The work hardening parameter n is of great importance in controlling the maximum uniform tensile strain ε_u .

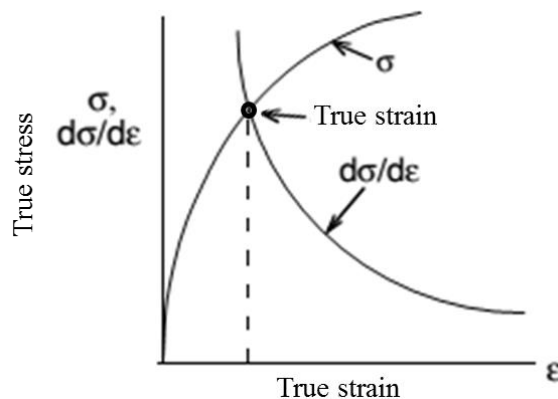


Figure 2-5 Schematic plot showing the intersection of the true stress-strain curve and strain-hardening curve that defines the mechanical instability or necking condition during tensile testing [25].

Korzekwa et al. [26] suggested that C-J analysis is more suitable for analyzing the work hardening behavior of DP steels. This C-J analysis use the power-law Ludwik relation

$$\sigma = \sigma_0 + k\varepsilon^n \quad (2.1.1)$$

Characteristics of Work-Hardening Process of DP steels

The process of work hardening of DP steels can be defined in three stages of plastic deformation [26-27].

- 1) At the beginning, the work hardening rate of DP steels is very high. Because of the plastic incompatibility of two phases, back stress builds up rapidly. The glide of mobile dislocations near martensite and the elimination of residual stresses facilitate the deformation process.
- 2) Then, the work hardening rate is reduced with increasing strain due to the constrained ferrite deformation in the presence of hard, undeforming martensite particles.
- 3) Finally, dislocations pile up at the α/α' interfaces, and dislocation cell structures are formed. Further deformation in the ferrite is dominated by dynamic cross-slip and yielding of martensite.

2.1.4.3 Ductility of DP Steels

One of the greatest advantages of DP steels is the high ductility at given strength level. Uniform elongation (UE), total elongation (TE), and reduction of area (RA) are important parameters of ductile behavior.

As mentioned previously, UE is closely related to strain hardening rate ($d\sigma/d\varepsilon$). Any parameters which can increase strain hardening exponent (n-value) or $d\sigma/d\varepsilon$ can provide higher UE.

Total elongation (TE) includes both UE and the post-necking strain (TE-UE). The duration of the post-necking deformation is limited by damage and flow localization (e.g. due to shear banding). When the material fails due to damage accumulation, the duration of the post-necking deformation depends on the rate of nucleation and growth of microvoids, and the moment of their coalescence to form the main crack. In DP

steels this is determined by the distance between martensite islands and ductile ferrite matrix properties [20].

Diffuse Necking and Localized Necking

Necking for flat samples is more complicated than samples with circular cross-sections. For thin flat samples, two kinds of necking or flow instability should be considered, including diffuse necking and localized necking. Figure 2-6 schematically illustrates diffuse necking and localized necking. Diffuse necking starts when the tensile load reaches the maximum point. The second type is called localized necking. In this mode, the neck is a narrow band inclined at an angle to the sample axis. Once localized necking starts, the width of the sample contracts little, but the thickness along the necking band reduces rapidly. Fracture occurs soon thereafter [28].

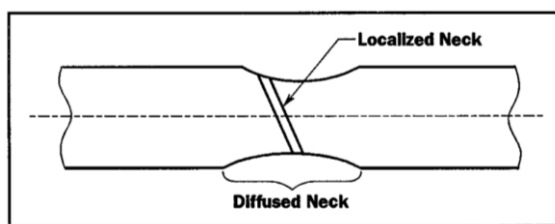


Figure 2-6 Schematic illustration of diffuse necking and localized necking of a thin strip [28]

A more detailed discussion about the influence of martensite and ferrite on ductile properties will be elaborated in the following sections.

2.1.4.4 The Role of Martensite in DP steels

Introduction to Martensite

Martensite is a metastable phase generated from rapid cooling of austenite, which is a supersaturated solid solution of carbon in ferrite [25]. Figure 2-7 illustrates the crystal structure of the martensite body-centered tetragonal unit cell with the octahedral interstitial sites occupied by carbon atoms. The c axis is longer than the other two

axes, which are named a axes and the higher carbon content, the greater the tetragonality, (c/a) [25].

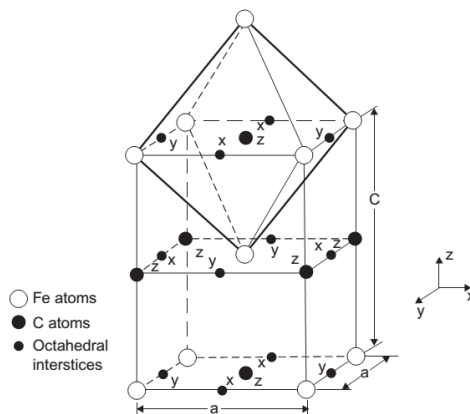


Figure 2-7 Crystal structure of the body-centered tetragonal unit cell and octahedral interstitial sites of carbon of martensite in iron-carbon alloys and carbon steels [25]

The term hardenability refers to the capacity of a steel to transform partially or completely from austenite to some percentage martensite at a given depth when cooled under given conditions [25]. The mechanical strength of martensite is influenced by its structure and its carbon content. There are two major morphologies of martensite, lath and plate. The temperature below which martensite starts to form in a given alloy is termed as martensite start temperature (M_s). The amount of thermodynamic driving force needed to initiate the shear transformation of austenite to martensite is reflected by M_s . Austenite with higher carbon content enjoys higher strength of shear resistance of the austenite, which results in a lower M_s . As shown in Figure 2-8, with the increase of carbon content, M_s decreases, and the martensite morphologies are also dependent on carbon content [25].

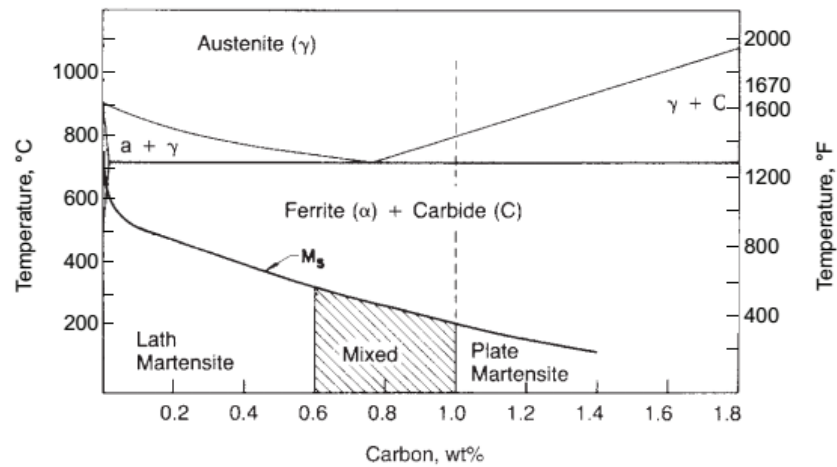


Figure 2-8 Effect of carbon content on M_s in iron-carbon alloys [25]

Carbon content in steel also influences the strength of martensite. Figure 2-9 shows that the hardness of martensite is affected by carbon content. These micro-hardness data can be converted to approximate the strength of martensite [29]. The strength of martensite increases with carbon content.

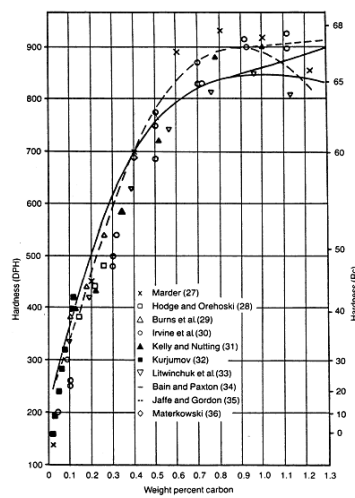


Figure 2-9 hardness of martensite microstructure as a function of carbon content [29]

As mentioned earlier, the role of martensite in DP steels during deformation is different from those in the single-phase conditions due to the interaction between the

two phases. The following section will elaborate the influence of martensite composition and content on mechanical behaviors of DP steels, including yielding behavior, strength and work hardening.

Martensite Morphology in DP steels

There are various martensite morphologies present in DP steels. Ahmad et al. [27] produced martensite with three different morphologies, including laths of martensite, grain boundary growth and bulk growth through different heat treatment. (Figure 2-10)

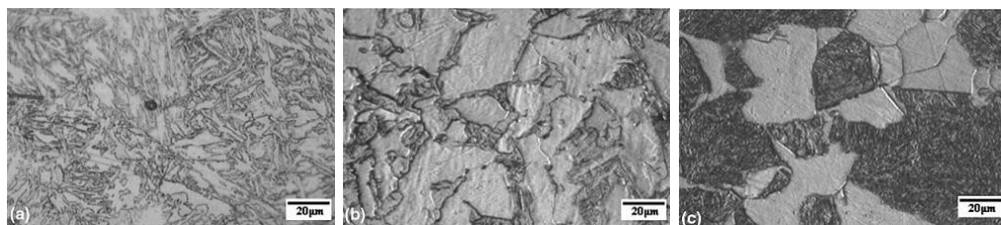


Figure 2-10 Different morphologies of martensite with similar martensite volume fraction obtained from varied heat treatment. (a) Laths of martensite; (b) Grain boundary growth; (c) Bulk growth [27]

Austenite-to-martensite Transformation Effect on DP Steels

Because the specific volume of martensite (α') is greater than that of austenite (γ), the martensite transformation of austenite during cooling from $\alpha+\gamma$ introduces a volume expansion on the microscale, which generates a high density of free mobile dislocations in the neighbouring ferrite matrix. In addition, the martensite transformation also induces pronounced internal stress in the ferrite phase [20].

Because of volume expansion, the adjacent ferrite grains have to deform plastically during the austenite–martensite transformation to accommodate the transformation strain. During this process, geometrically necessary dislocations (GNDs) are required to maintain lattice continuity and statistically stored dislocations (SSDs) are generated

from work hardening of ferrite [5].

Due to the relatively low temperature of martensite transformation and high cooling rate, there are few interstitial solutes in untransformed ferrite, which pronouncedly reduce solute-dislocation interactions [20]. The high level of residual stress also contributes to reducing the stress required for dislocations sliding. Therefore, DP steels do not require an initial threshold stress to separate the dislocation from the solute, and thus no yield point is present.

The Effect of Martensite on Yield Strength of DP Steels

The absence of yield point elongation and low YS/UTS ratio (0.4-0.5) is an intrinsic characteristic of DP steels. The high density of free mobile locations is responsible for the low yield strength in DP steels [20].

Figure 2-11 depicts the effect of V_M on YS of cylindrical samples of Cr-Mn-Si-B steels with carbon content varied from 0.07% to 0.18% quenched from different temperature in the intercritical region. There is an initial decrease in YS and then YS begins to increase once V_M is larger than 0.2.

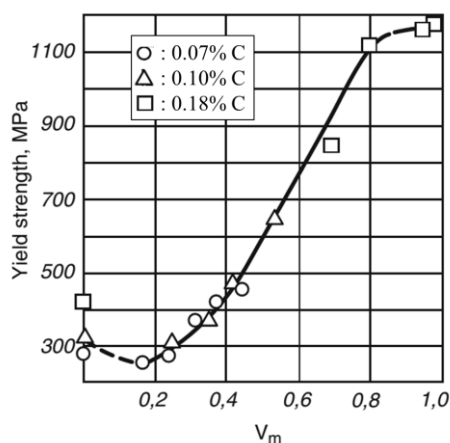


Figure 2-11 Effect of volume fraction of martensite on YS of Cr-Mn-Si-B steel with varied carbon content quenched from 760 to 820°C [20]

It should be emphasized that those DP steels with TS up to 1200 MPa and V_M up to 75% cannot be directly compared with those DP steels with TS below 600-700 MPa and V_M below 30-35%. When martensite volume fraction rises to 45%, martensite starts to dominate the strength of DP steel, because higher V_M allows martensite to form a skeleton structure and the actual ability of the steel to bear load depends increasingly on martensite strength [20].

As mentioned previously, residual stresses and GND are generated from the austenite-to-martensite transformation, and they are closely related to the YS of DP steels.

Therefore, any factors which can affect residual stresses and GND are able to influence YS; for example, the annealing temperature, M_s , and the cooling rate.

Fonstein et al. [30] performed a large number of experiments on steels with different manganese and carbon content to compare the behavior of those DP steels with various V_M and M_s . It is possible to assume that steels with equal strength have an equal volume fraction of martensite. The experimental results indicated that decreasing M_s by increasing C or Mn concentrations can result in a reduction in YS/UTS ratio (Figure 2-12). This is because lower M_s offers shorter time for dislocations generated to be annihilated during the cooling process. In the case of decreasing M_s by increasing carbon content in austenite, higher residual stresses tend to be introduced into ferrite due to an increase in the volume change during austenite-to-martensite- transformation [20].

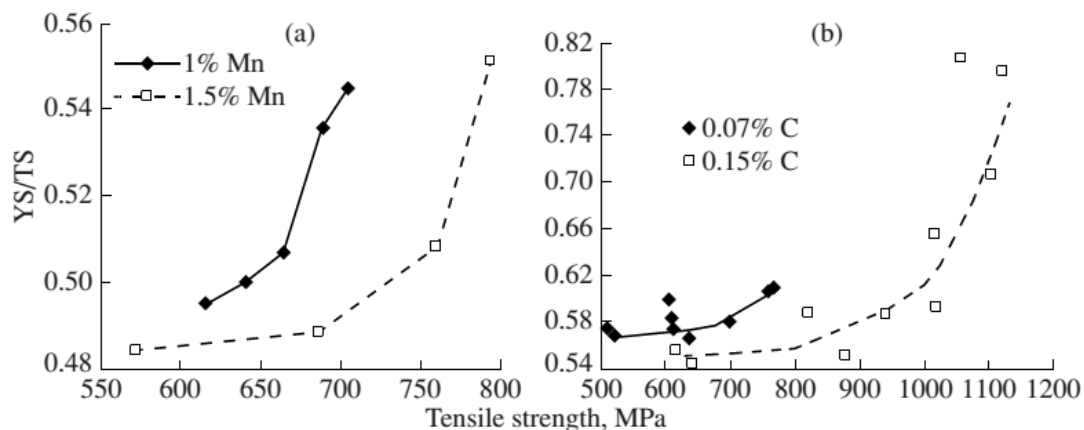


Figure 2-12 Effect of Mn and C concentration in steels on the YS/UTS ratio depending on the ultimate tensile strength of steel (after water quenching from different temperatures): (a) the effect of Mn in steel with $\sim 0.08\%$ C; (b) the effect of C in steel with $\sim 1.5\%$ Mn [30]

The Effect of Martensite on Tensile Strength of DP Steels

A α/α' DP steel can be regarded as a composite material composed of soft ferrite and hard martensite. According to the rules of mixture, the strength of DP steels can be described as

$$TS_{DP} = TS_F V_F + TS_M V_M \quad (2.1.2)$$

where TS_{DP} , TS_F , and TS_M correspond to the tensile strength of DP steels, ferrite and martensite, respectively. V_F refers to the volume fraction of ferrite.

Bortsov and Fonstein [31] performed a series of tensile tests on steels with various carbon content and martensite volume fraction. As shown in Figure 2-13, the rate of strengthening (TS_M / V_M) by martensite obtained from experiment ($11.5 \text{ MPa} / \%M$) is three times higher than the value calculated from the rule of mixture, but the absolute experimental values of TS_{DP} were lower than calculated. The tensile strength

of DP steels is irrelevant with the intrinsic strength of martensite and is dependent on V_M .

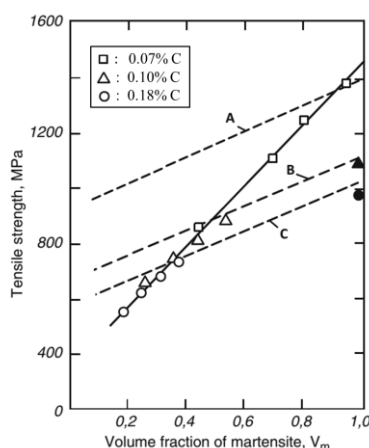


Figure 2-13 Effects of the volume fraction of martensite on the ultimate tensile strength of DP CrMnSiB steels with different carbon content: dashed lines correspond to calculations using rules of mixtures. (A-0.18% C; B-0.10% C; C: 0.07% C) [31]

According to Davis, the possible reasons for the higher carbon containing DP steels and low carbon DP steels having similar strength is that α' formed in DP steels enjoys lower strength in comparison with the strength of α' formed in fully quenched steels with the same carbon content. There are weaker strain constraints and stress relaxation in ferrite matrix during the austenite-to-martensite transformation [32].

In addition, the carbon concentration in martensite (C_M) might be overestimated due to neglecting carbon solubility in ferrite and formation of carbides of vanadium, niobium, etc. Moreover, it should be noted that martensite continuity also exerts an influence on the strength of martensite in DP steels. The formation of a continuous martensite network (martensite skeleton) tends to retard the rate of increase of strength with V_M [24]. This essentially means that the rule of mixtures does not represent the mechanical behaviour in these cases.

The Effect of Martensite on Strain Hardening of DP steels

The strain hardening behavior of DP steels can be interpreted in terms of hardening by non-deforming particles which cannot be cut by dislocations. Ashby's theory is one of the models being employed to understand the work hardening behavior of DP steels [33].

$$\sigma - \sigma_0 = kG \sqrt{\frac{bV_M \varepsilon_{pl}}{0.4\bar{L}_M}} \quad (2.1.3)$$

where σ_0 is a constant, related to the initial flow stress, G is the shear modulus of the matrix, b is the Burgers vector of the matrix dislocations, V_M is the volume fraction of hard phase, \bar{L}_M is the average particles size, ε_{pl} is the plastic strain, and k is a constant of the order of 1.

Differentiation of equation (2.1.3) gives

$$\frac{d\sigma}{d\varepsilon} = kG \sqrt{\frac{0.625bV_M}{\varepsilon_{pl}\bar{L}_M}} \quad (2.1.4)$$

According to the equation (2.1.4), for given plastic strain ε_{pl} , the strain hardening rate of DP steels increases with higher V_M and lower \bar{L}_M . The Ashby theory suggests that the high strain hardening of DP steels at the initial deformation is attributed to the significant difference in hardness of microstructure constituents [33].

According to Speich and Miller [34], there are three reasons for the accelerated work hardening of DP steels at the initial deformation. Firstly, during austenite-to-martensite deformation, residual stresses are generated. Secondly, both GNDs and SSDs are formed, and the dislocation density in ferrite is increased. Thirdly, the plastic incompatibility of the two phases is too large to be balanced by plastic deformation, so stresses are created within the martensite phase which is compensate for by back

stresses in the ferrite. The back stresses retard dislocation movement in the ferrite. Lanzillotto and Pickering [35] put up with the following analytical expression by neglecting the contributions to the work hardening and strength from statistically stored dislocations (SSD) for strain ε_{pl} less than 0.2.

$$\sigma - \sigma_0 = A\sqrt{\frac{\varepsilon_{pl}V_M}{\bar{L}_M}} + BV_M\sqrt{\frac{\varepsilon_{pl}}{\bar{L}_M}} \quad (2.1.5)$$

where A and B are constants.

Differentiation of equation derives the work hardening rate

$$\frac{d\sigma}{d\varepsilon} = \frac{1}{2\sqrt{\varepsilon_{pl}\bar{L}_M}} (A\sqrt{V_M} + BV_M) \quad (2.1.6)$$

Equation (2.1.6) also suggests that for a given plastic strain ε_{pl} , the strain hardening rate of DP steels increases with higher V_M and lower \bar{L}_M .

The relationship between the work-hardening rate and the size of the martensite particles obtained from the equation (2.1.6) are compared with experimental data in Figure 2-14. As shown below, the experimental data are in agreement with the theoretical calculations. Therefore, Lanzillotto and Pickering concluded that the work-hardening rate increases with the decrease of martensite particle size and an increase of martensite volume fraction. However, discrepancies occurred between the experimental data and predicted values of the work hardening rate when the true strain reaches 0.5, when the martensite starts to deform and the decohesion of the α/α' interface occurs [35].

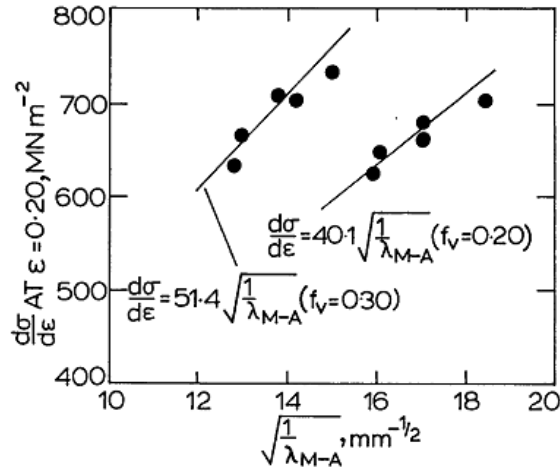


Figure 2-14 Relationship between work hardening rate at strain $\varepsilon_{pl} = 0.20$, and the size of martensite particles. f_v and λ_{M-A} refer to the volume fraction and average particle diameter of the martensite-austenite (M-A) constituent, respectively [35]

Ramos et al. [36] found that with an increase in the strength of martensite (C_M), the work hardening at initial strain increases as a result of larger plastic incompatibility between the two phases, which is in accordance with Ashby theory.

The Effect of Martensite on Ductility of DP Steels

As it mentioned previously, uniform elongation (UE), total elongation (TE), and reduction of area (RA) are important parameters of ductile properties. A high work hardening rate (n value) stabilizes tensile deformation against local plastic instabilities and results in a greater UE.

Speich and Miller [34] derived an empirical equation by correlating the true uniform strain of DP steel, ε_u^{DP} , and true uniform strain of ferrite, ε_u^F with C_M and V_M :

$$\frac{\varepsilon_u^{DP}}{\varepsilon_u^F} = 1 - 2.2C_M \sqrt{V_M} \quad (2.1.7)$$

The equation (2.1.7) suggests that uniform elongation is increased with a decrease of

C_M and V_M . Speich and Miller concluded that raising ε_u^F is the most efficient way to achieve high UE.

Movahed et al. [37] investigated the influence of martensite volume fraction on UE and TE. As shown in Figure 2-15, both UE and TE increases with increasing V_M until around $50\%V_M$, and then decreases with further increase in V_M . This can be explained by the martensite carbon content variation. Increasing V_M leads to a decrease in martensite carbon concentration, which results in higher ductility of martensite phase, which is in accordance with the empirical equation (2.1.7).

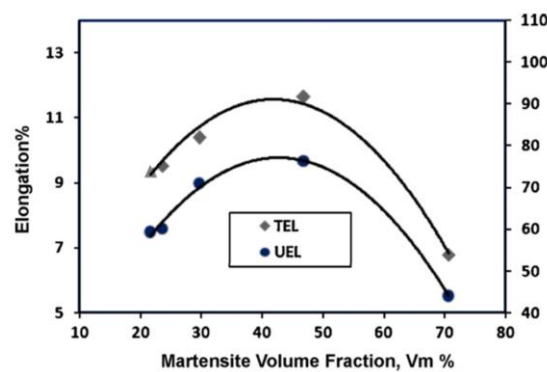


Figure 2-15 Effect of martensite volume fraction on the uniform elongation and total elongation of DP steels [37]

Total elongation (TE) incorporates uniform elongation (UE) and post-necking strain (TE - UE). The post-necking process for flat samples includes diffuse necking and localize necking. Speich and Miller [34] found that TE decreases with increasing V_M of DP steels. This can be interpreted with both smaller UE and smaller TE - UE.

The duration of the necking process (TE-UE) depends on the rate of nucleation and amount of microvoids, but the moment of their coalescence to form a main crack is defined by the distance between martensite islands and properties of ductile ferrite

matrix. In addition, decohesion along grain boundaries or fracture of martensite can also influence the span of necking process. Therefore, an increase in V_M decreases the void spacing and thus the plastic strain necessary for their coalescence. It was shown that the post-necking process duration decreases with increasing C_M due to easier decohesion or martensite fracture [38].

Matsumura and Tokizane found that the specimens with fine DP structure show higher ductility compared with specimens with coarse DP structure having the same V_M . DP steels with finer structure enjoy higher uniform elongation and smaller voids and hence their delayed coalescence [20].

2.1.4.5 The Role of Ferrite in DP steels

Introduction of Ferrite in DP Steels

The properties of the ferrite are significantly influenced by heating and holding in ($\alpha + \gamma$) region. Those properties include ferrite grain size, the extent of its recovery and recrystallization, the concentration of dissolved interstitials, partitioning of alloying elements, and precipitation hardening. During cooling from the ($\alpha + \gamma$) regime so-called new ferrite (NF) is formed due to insufficient austenite stability. Therefore, there exists both “old ferrite” and new ferrite (NF) after intercritical annealing. NF tends to contain lower concentrations of ferrite-forming elements in comparison with the initial ferrite. In the presence of carbonitrides-forming elements, such as V, Nb, Ti, NF can be strengthened by interphase precipitates. In addition, because NF is closer to martensite generated from austenite, it usually exhibits a high dislocation density. Due to the high cooling rate, there is not sufficient time for diffusion of interstitial atoms from NF to austenite, which results in higher concentration of interstitial atoms in NF compared to “old ferrite” [20].

The Effect of Ferrite on Strength of DP Steels

The effects of ferrite grain size on the flow stress of DP steels can be described by Hall-Petch equation:

$$\sigma_y = \sigma_0 + K_y d^{-1/2} \quad (2.1.8)$$

where σ_y refers to the yield stress, σ_0 is a frictional stress, K_y is a constant and refers to the intensity of stress necessary to generate new dislocations in the surrounding ferrite grains, and d is the grain diameter.

Calcagnotto et al. [39] summarized previous work on the influence of grain size on yield strength and tensile strength of DP steels, as shown in Figure 2-16. All of the data showed that the Hall-Petch relation is obeyed.

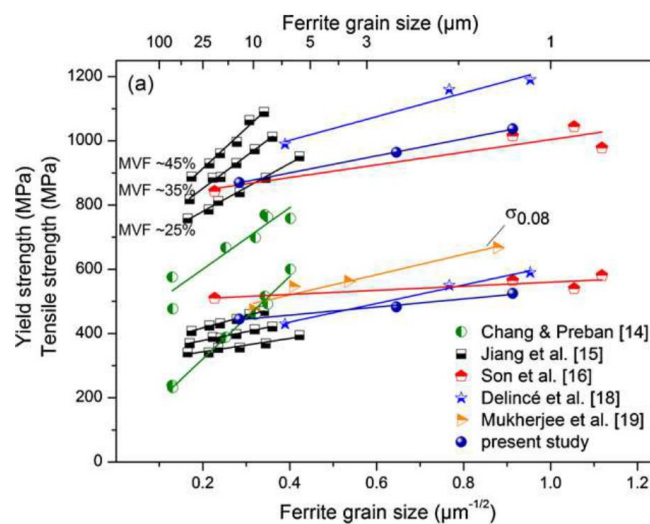


Figure 2-16 Grain size dependence of yield and tensile strength. (MVF represents volume fraction of martensite) [39]

The Effect of Ferrite on Strain Hardening of DP Steels

According to Davies' [40] research, strengthening ferrite by substitutional elements such as Si and P can increase the strain hardening rate and thus the uniform elongation of DP steels, which can be interpreted by localization of the initial deformation in ferrite and the contribution of intrinsic properties of ferrite by those elements

Calcagnotto et al. [39] found that ferrite grain refinement which is always accompanied by refinement of martensite particles helps increase initial strain hardening rate. They attributed the influence of ferrite grain refinement to early dislocation interactions, a higher number of dislocation sources and the back stresses from martensite islands.

The Effect of Ferrite on Ductility of DP Steels

When the volume fraction of martensite is constant, the ductility of a DP steel is governed by the properties of ferrite matrix. Figure 2-17 illustrates the influence of grain size on uniform elongation and total elongation of DP steels. A higher strain hardening rate delays the onset of necking and thus increases UE [39].

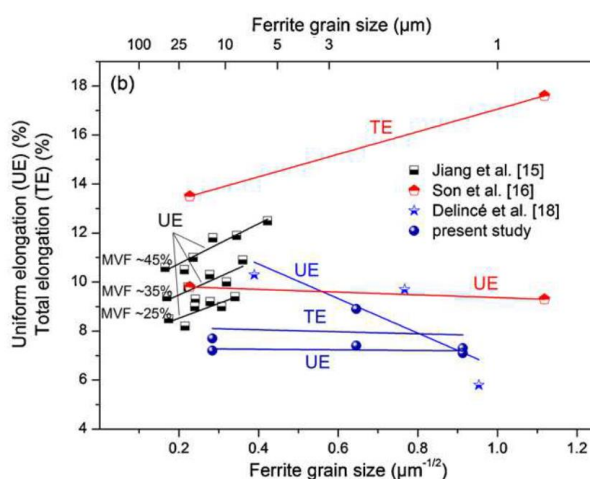


Figure 2-17 Grain size dependence of uniform and total elongation. (MVF represents volume fraction of martensite) [39]

Sugimoto et. al [20] found that ferrite grain refinement can lead to favorable higher RA values due to relative suppression of size-related critical stresses and hence delayed void formation around martensite islands.

2.1.4.6 Fracture Behaviour of DP steels

The applications of high strength materials are usually limited by their fracture

behavior. [20] α/α' DP steels can be regarded as a composite microstructure composed of soft ferrite matrix and hard martensite islands, and thus the fracture characteristics of DP steels are attributed to those two individual phases. In order to investigate how ferrite and martensite microstructure influence fracture behavior of nonhomogeneous DP steels, four possible questions can be considered [41]:

- 1) How does the second phase influence the homogeneity of deformation?
- 2) How does the second phase including pre-existing micro-cracks and non-metallic inclusions influence the driving forces for crack propagation and on the crack paths?
- 3) How do the individual phases describe the fracture characteristics?
- 4) What is the relationships between those fracture parameters, for example, the size of the plastic zone, r_y , or the critical crack opening displacement, and microstructural dimensions (grain size or particle spacing)?

Fracture Mechanisms of Metals

The most common fracture modes of metals are a brittle fracture and ductile fracture. Brittle fracture encompasses both cleavage and intergranular fracture. Ductile fracture includes failure by plastic instability and micro-void coalescence [42].

1) Brittle Fracture

During the fracture process, steps or ridges appear on the fracture surface to balance the local misorientations. For BCC metals, these steps present indentation marks and they are named “tongues”. To maintain the equilibrium of the crack front, the nearest steps merge together and form a single step of higher height resulting in the formation of “rivers”. These rivers tend to be parallel to the same direction of the local propagation of the cleavage cracks. The surfaces of cleavage facets tend to be normal to the maximum principal stress on a macroscopic scale. Figure 2-18 is a typical brittle fracture surface observed on steels and illustrates of the formation of an intergranular triangle along the grain boundary crossed by a cleavage plane. Both

cleavage facets and some intergranular facets are present on the surface when a cleavage micro-crack located in a given grain crosses a grain boundary with a tremendous twist misorientation component [42].

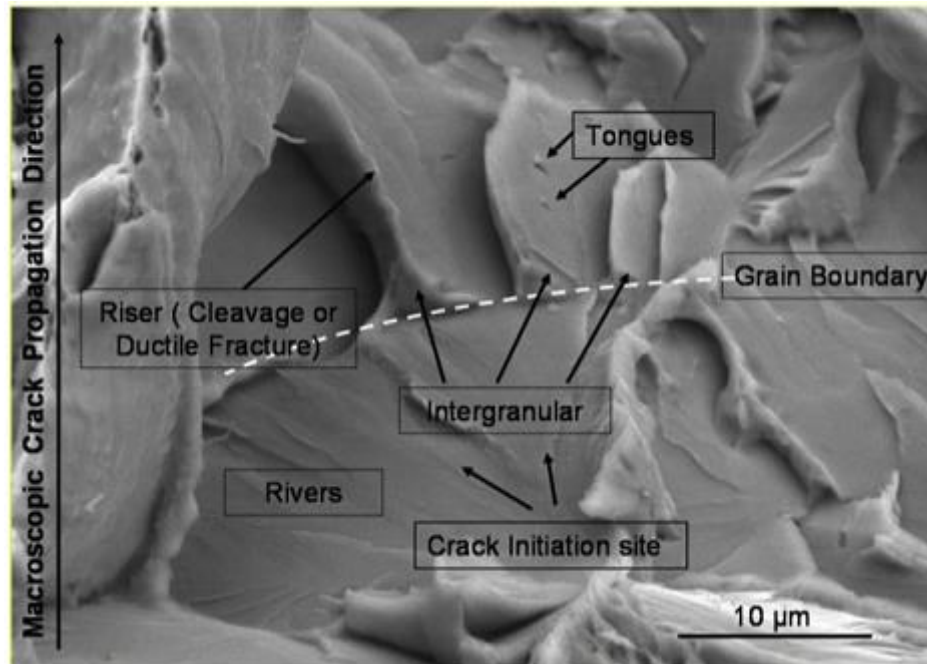


Figure 2-18 Cleavage fracture surface showing the segmentation of the cleavage crack front into four facets separated by risers in the grain [42]

2) Ductile fracture

A typical ductile fracture surface observed on UFG IF steel is shown in Figure 2-19 [42]. The main dimples can be used to trace void formation at second-phase particles or inclusions.

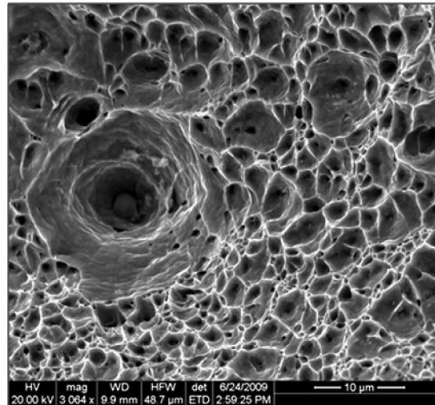


Figure 2-19 Dimpled fracture surface of ultra-fine grained IF steel [42]

Ductile failure by micro-void coalescence or by plastic instability is illustrated schematically in Figure 2-20. In the first case, voids nucleate and then grow with the assistance of plasticity. When they coalesce, a crack forms and the material fails by ductile tearing. However, voids are not necessary even though they might facilitate failure by instability. Failure by plastic instability is usually involved with shear banding. Material separation occurs through the shear band and induces void nucleation, growth and coalescence [42].

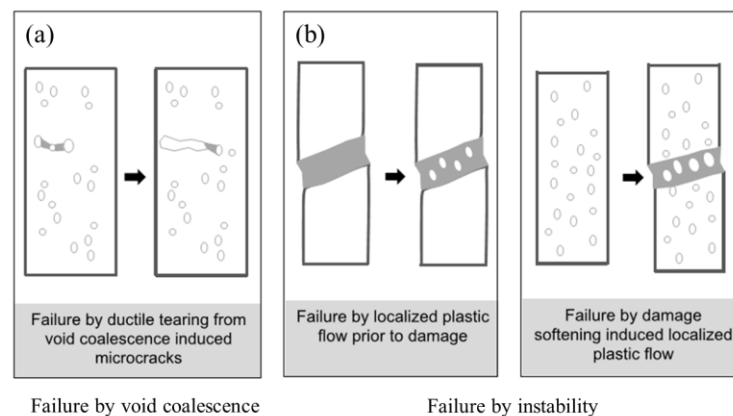


Figure 2-20 Schematic representation of two types modes if ductile failure (a) by micro-voids coalescence; (b) by plastic instability [42]

Figure 2-21 schematically depicts a typical process of void nucleation, growth and

coalescence nucleated on second-phase particles when the specimen is subjected to uniaxial loading. When the specimen reaches the maximum strength, where strain hardening cannot compensate the loss in the cross-sectional area (plastic instability), damage gradually builds up in the materials and the engineering stress drops. The knee in the curve corresponds to the onset of a macroscopic crack through the coalescence of the primary voids. The decreasing of the curve is related to the crack propagation process [43].

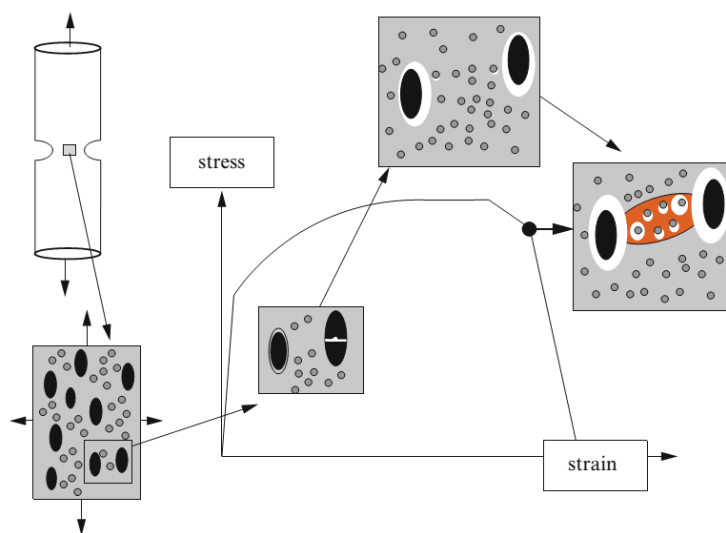


Figure 2-21 Process of micro-void coalescence failure corresponding to the macroscopic mechanical response [43]

Fracture Mechanisms of DP steels

Due to unequal phase strains, fracture of hard particles, or decohesion of phase interfaces, the harder phase primarily influences crack initiation. The amount of strain that results in nucleation of microvoids in α/α' DP steels depends on the strength of α/α' interfaces, by the strength and shape of the martensite particles, and by the properties of ferrite that dominate the unequal distribution of plastic strains between phases during deformation process. The extent of interfacial void nucleation can also

be effectively affected by solutes which generate interface segregations [20]. Due to the complexity of microstructural parameters and microstructure heterogeneity, void nucleation in DP steel varies among materials. Figure 2-22 offers a schematic presentation to show how V_M and ferrite grain size affect the void nucleation mechanisms of DP steels. When martensite fraction is high enough to form a skeleton structure, martensite undergoes plasticity earlier and hence martensite cracking is promoted. In contrast, for DP steels with smaller amounts of martensite and larger ferrite grain sizes, interface damage mechanisms are dominant. When ferrite grain size is decreased for low martensite content, both mechanisms are present [4].

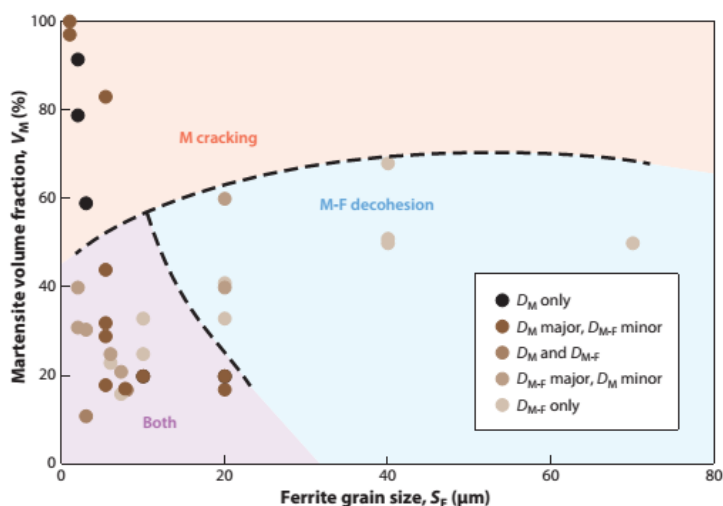


Figure 2-22 A summary of void nucleation mechanism for DP steel [4]

Generally, the toughness of DP steels is determined by the properties of martensite and ferrite. The parameters used to characterize martensite include the volume fraction, morphology (shape, size, and distribution), and toughness, which are controlled by carbon content in martensite. The parameters that characterize martensite exhibit a complex interrelationship with each other.

For instance, when the steel composition remains the same, an increase in V_M leads to

its higher intrinsic toughness of martensite because of its lower C_M . A decrease in V_M also can introduce an additional favorable effect of reduced martensite continuity. This should prevent crack propagation due to the necessity for a crack to bypass or cleave the dispersed martensite particles that elevates toughness [20].

2.2 Grain Refinement of BCC Steels

There are several mechanisms to enhance the strength of materials. Grain refinement is the only method to elevate both strength and toughness at the same time.

Grain refinement provides many advantages in terms of strengthening steels: for example, lowering cost by avoiding additional alloying elements and heat treatment, and facilitating weldability due to lower required carbon contents and other alloying elements in comparison with other high strength steels [44].

2.2.1 Methods of Producing Ultrafine-grained (UFG) Steels

There are mainly two kinds of methods to produce ultrafine-grained (UFG) bcc steels: severe plastic deformation (SPD) techniques and advanced thermomechanical processing.

2.2.1.1 Severe Plastic Deformation (SPD) Techniques

Severe plastic deformation (SPD) techniques impose large plastic strains in materials under high applied pressure and at relatively low temperatures. They have been applied to produce UFG metals. [45] Typical SPD techniques include equal-channel angular pressing (ECAP), accumulative roll bonding (ARB), bidirectional compression, and high-pressure torsion (HPT). SPD techniques require a well-designed strain path and are usually applied on a small scale due to the complexity and the discontinuous nature of these processes [44].

2.2.1.2 Advanced Thermomechanical Process

Rather than applying large strain, advanced thermomechanical methods use the

following ways to produce UFG steels. For advanced thermomechanical methods, the high temperature phase can be pretreated to obtain larger grain boundary area and to introduce more dislocation substructure by large strains at the lowest possible temperature to prevent static primary recrystallization. Finally, warm or cold deformation can be applied to the transformed product, and sometimes carbide precipitation is involved. Advanced thermomechanical methods include recrystallization of austenite during hot deformation, strain-induced ferrite transformation, intercritical hot rolling, dynamic recrystallization of ferrite during warm deformation, pronounced recovery of ferrite during warm deformation and annealing, and cold rolling and annealing of martensitic steel [44].

Advanced thermomechanical methods are large-scale industrial processes in comparison with SPD. Advanced thermomechanical methods are continuous processes, require less total strain, and can be more easily optimized to operate at a desired temperature where they beneficially utilize phase transformation and controlled cooling. However, the advanced thermomechanical routines are less effective with respect to grain refinement compared to SPD methods [44].

2.2.2 Microstructure Characterization of Ultrafine-grained (UFG) Steels

To quantitatively characterize the microstructure of UFG steels, it is necessary to report the average grain size, the corresponding grain size distribution, and the fraction of high-angle grain boundaries produced from the various processing methods. Because of intense deformation, the UFG steels produced by SPD are usually more elongated. About 40% of the grain boundaries are subgrain boundaries, which are less beneficial for the overall mechanical properties. Hot deformation produces larger more polygonised subgrains during dynamic recovery in comparison with the submicron structure obtained from SPD. Compared to hot deformation, warm and cold deformation speed up grain subdivision owing to a relatively higher

dislocation density accumulated. Subsequent annealing facilitates the formation of high-angle grain boundaries through severe recovery /recrystallization processes [44]. The effects of alloying are similar during the various types of processing. Solid solution additions enhance the degree of strain hardening in both cold and hot working and may retard dynamic recovery in BCC steels [44]. Large amount of second phase constituents, for instance, fine cementite particles, are beneficial for the formation of a fine ferritic grain structure. They prevent grain boundary migration because of Zener pinning. This effect stabilizes the ultrafine grains against grain coarsening and may also retard primary recrystallization. The presence of such fine particles results in an increase of the effective recrystallization temperature, widening the temperature range for corresponding warm rolling and annealing treatments [46].

2.2.3 Mechanical Properties of Ultrafine-grained (UFG) Steels

Compared with those coarse-grained steels, UFG steels enjoy an improved combination of strength and toughness.

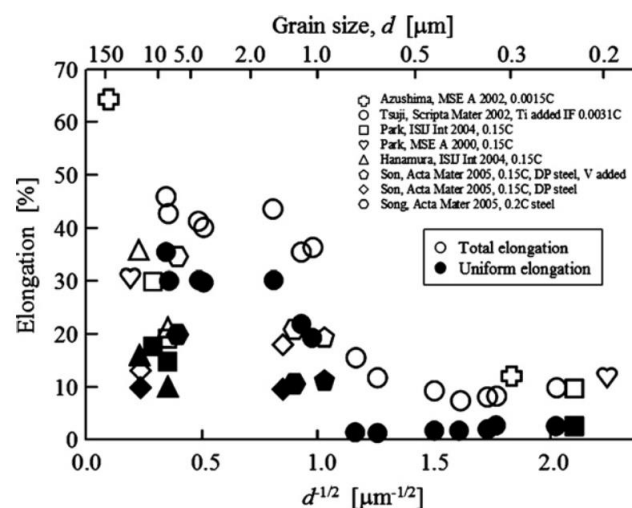


Figure 2-23 Grain size dependence of ductility for bcc steels [44]

As mentioned earlier, grain refinement helps increase the yield stress of the steels

according to Hall-Petch relation. For ductility, Figure 2-23 illustrates tensile ductility with the inverse square root of grain size of BCC steels with grain size of 150-0.2 μm . The figure suggests that for UFG steels, the tensile ductility tends to decrease with the decrease of grain size. This phenomenon can be explained as follows. Firstly, dislocations that carry the intragranular strain are trapped at grain boundaries during deformation. The trapped lattice dislocations spread into the grain boundaries and changes the dislocation density during dynamic recovery. It is suggested that there are two kinds of recovery mechanisms, including slow recovery in the grain interiors and much faster recovery near grain boundaries. In UFG steels, the latter plays an important role during deformation. Secondly, plasticity instability contributes to a decrease in tensile ductility. In UFG steel plastic instability occurs at an early stage during tensile testing, which leads to limited UE in UFG steels [44]. However, high ductility can be obtained due to the presence of finely dispersed cementite particles. Those particles can facilitate the work hardening rate due to the accumulation of GNDs surrounding the particles [47].

2.3 Two Dimensional (2D) Digital Image Correlation (DIC)

Understanding the relationship between material microstructure and deformation is of great importance from a materials engineering perspective. In particular, measurements of the localized heterogeneous deformation and strain distribution are crucial in understanding the role of different microstructure in the deformation behavior of multiphase materials and composite [48].

2.3.1 Brief Introduction of Full-field Optical Methods

The development of full-field optical measurement techniques successfully provides abundant information for material characterization. Because of the contactless nature of full-field optical methods, the abundant information they provide, their speed and

resolution, these methods have tremendous potential both for the research lab and for real application in industry. Table 2-1 provides a summary of several types full-field optical measurement techniques [49]. These measurement techniques can be classified based on the nature of the physical phenomenon involved, for instance, white light (non-interferometric methods) and interferometric methods. Non-interferometric techniques determine the surface deformation by comparing the gray intensity evolution of the object surface before and after deformation and usually have less strict requirements under experimental conditions. Interferometry requires a coherent light source, and the measurements are usually performed in a vibration-isolated optical platform in the laboratory. Interferometric techniques realize the deformation measurement by recording the phase difference of the scattered light from the test object surface before and after deformation. The measurement results are related to interferometric fringes, and hence further fringe processing and phase analysis techniques are needed [50]. A more detailed introduction of full-field optical measurement methods is provided in reference [49].

Table 2-1 Summary of various full-field optical measurement techniques [49]

Classification		White light (Non-interferometric methods)				Interferometry			
Measured Encoding / Interaction mode		Random encoding		Phase modulation (Periodic signal)		Reflected light	Diffuse light		Diffracted light
Measurand		In-plane dis.	Shape	In-plane dis.	Shape	Out-of-plane dis.	In-plane dis.	Out-of-plane dis.	In-plane dis.
Examples		Digital image correlation (DIC) Deflectometry	Stereo-correlation	Grid method (with or without moiré)	Fringe projection (structured light)	Michelson Interferometry	In-plane speckle	Out-of-plane speckle	Moiré interferometry
Differential Setup (slopes, strain)		Not used		Deflectometry		Nomarski microscopy	Shearography		Grating differential interferometry
Performances	Simplicity	+ +		+		-			
	Cost	-		-		+			
	Performances	-		- +		+ +			

Digital image correlation (DIC) is a representative non-interferometric full-field optical technique. Compared with other optical techniques, DIC is generally more

cost-effective, simpler and still offers an accurate solution [51]. The following section will elaborate the implementation procedures, basic principles and concepts, and microscopic measurements of DIC method.

2.3.2 Digital Image Correlation Method

2.3.2.1 Definition and Background

Digital image correlation (DIC) is an innovative computer-vision-based, non-contact, full-field technique which is used for deformation measurement [52].

DIC provides full-field displacement and strains by comparing the digital images of the specimen surface in the reference and deformed states respectively. In principle, DIC is an optical metrology method relying on digital image processing and numerical computing [50]. This technique was developed in the early 1980s, and it had exerted a profound impact in the field of mechanics of solids and structure [52-53]. Nowadays, this technique is still undergoing prominent developments.

DIC method has been extensively investigated and improved for reducing computation complexity, achieving high accuracy deformation measurement and expanding the application range over the past few years [50]. Software techniques have been applied to efficiently perform the complicated algorithms and obtain sub-pixel resolutions. These make it feasible for high-resolution measurements with commercially available digital photography, such that surface deformation can be measured down to one part per million of the field of view [51].

Nowadays, it is possible to use images shot by fast and ultra-fast cameras at time scales down to the microsecond or less, as well as those acquired by a scanning electron microscope (SEM) or an atomic force microscope (AFM) at micrometric or nanometric scales. Multi-camera system makes it possible to obtain three dimensional (3D) shapes and displacement fields of the surfaces of an observed object. 3D images acquired by computed (micro) tomography or magnetic resonance imaging can also be

utilized to measure 3D displacement fields in the bulk of various (optically opaque) materials [49]. Recently the DIC technique has been applied to study the local and global deformation and fracture behavior for in/ex-situ local strain analysis [48]. One of the major advantages of DIC method is the full-field nature of the measurement data, which allows quantitative analysis. DIC techniques can be applied to 2D or volumetric images. 2D deformation and motion measurements were the basis of the early applications in DIC. In this thesis, the emphasis is placed on the introduction of 2D DIC method.

2.3.2.2 Technical Procedures of 2D DIC

Generally, the implementation of the 2D DIC method includes the following three steps:

- (1) Specimen and experimental preparations;
- (2) Recording images of the planar specimen surface before and after loading;
- (3) Processing the acquired images through a computer program to obtaining the desired displacement and strain information. This section will provide the specimen preparation and image capture first and then present the basic principles of 2D DIC in Aramis software [50].

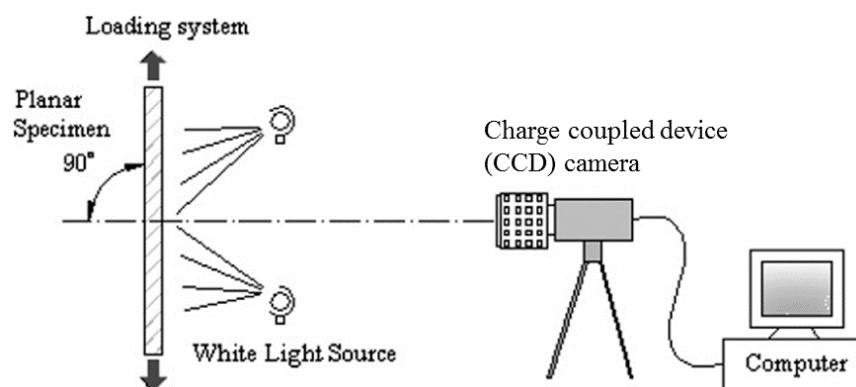


Figure 2-24 Typical optical image acquisition system for the 2D DIC method [50]

The schematic illustration of a typical optical image acquisition system for 2D DIC method is presented in Figure 2-24. A nominally flat sample is subjected to loading. The camera is placed with its optical axis perpendicular to the specimen surface, imaging the planar specimen surface in different loading states onto its sensor plane [55]. The CCD camera is usually used for conventional macroscopic 2D DIC tensile test as an imaging system. When SEM is coupled, microscopic 2D DIC tensile test is applicable. Commercial software can be applied to data processing. Aramis software [50] has been utilized in this project.

The specimen surface is of crucial importance for performing a DIC test. The specimen surface must have a randomly distributed greyscale speckle pattern with good contrast and brightness which is able to follow the deformation of the specimen and must not break or flake off the surface. The speckle pattern can be the natural texture of the specimen surface or artificially made by spraying black and/or white paints, or other techniques [55]. Figure 2-25 (c) presents a good example for high contrast stochastic pattern on specimen surface. Usually patterns are suited particularly well for the process of matching if the ratio between light and dark are around 50:50 and the transitions between them are not too sharp. [50], [55]

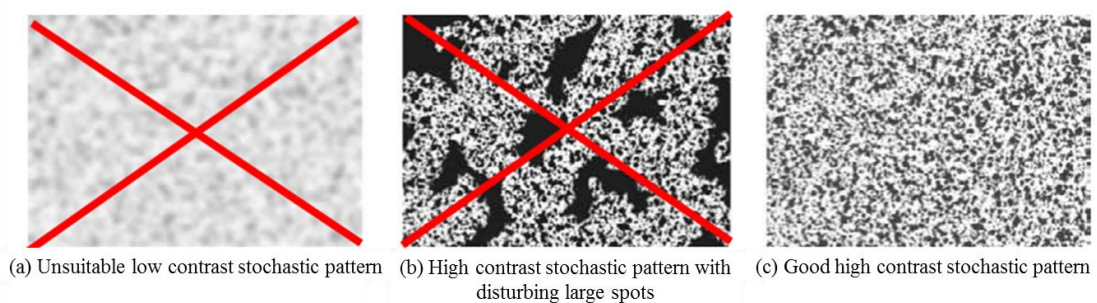


Figure 2-25 Comparison between specimens with different stochastic pattern [55]

In order to alleviate the systematic error introduced during measurement, the following requirements must be satisfied [55]:

(1) The specimen must be nominally planar and remain in the same plane parallel to the CCD sensor target throughout the deformation process. The CCD sensor and the object surface should be parallel and out-of-plane motion of the specimen during deformation should be small enough to be neglected.

(2) The influence of geometric distortion of the imaging system should be small enough to be neglected. In practice, geometric distortion is unavoidable in either optical imaging system or other high-resolution imaging system (e.g. SEM or AFM), which tends to impair the ideal linear correspondence between the physical point and imaged point and generates additional displacements. If geometric distortion is too pronounced, additional corresponding techniques should be applied to remove the influence of distortion to provide accurate measurements.

2.3.2.3 Fundamental Principles of 2D Aramis software

Aramis software is one of the commercially available software packages used for DIC data analysis. The application of Aramis software is used for analyzing, calculating and documenting deformations. Aramis software can recognize the surface structure in digital images and assign coordinates to every pixel in the image. The first image gathered in the measuring project represents the undeformed state of the object. After or during the deformation of the measuring object, further images are recorded. Then, Aramis software compares the images in different states and computes the motion of each image point and then deriving the displacement and deformation of the object characteristics. [53-54]

A facet is a unit domain of the pattern used to calculate the strain [48]. The distance between the center of the consecutive facets is called facet step. Both facet size and step size are given with dimensions in pixels. During computation, the Aramis software computes the deformation of the specimen through the images in different stages by means of square or rectangular image details, so-called facets. Figure 2-26

shows an example of 15x15 facets with 2 pixels overlapping area [55].

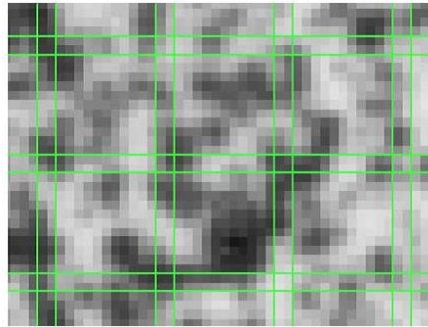


Figure 2-26 The default facet (15x15 pixels) with a facet step of 13 pixels corresponding to 2 pixels overlapping area [55]

The reasons why a facet instead of an individual pixel, is selected for matching is that the facet containing a wider variation in grey scales will distinguish itself from other facet, and can be more uniquely located in the deformed image [55].

The facet size and step size influence the quality of the DIC results. When the facet size and step size setting deviates from the default value in Aramis software system, the following factual relations in Table 2-2 apply [55]:

Table 2-2 Influence of facet size and facet step on calculation in Aramis software [55]

facet size		facet step	
Facet size < Default value	Facet size > Default value	Facet step < Default value	Facet step > Default value
<ul style="list-style-type: none"> - The accuracy of the resulting measuring point decreases. - The computation requires less time. - Local effects can be captured better. 	<ul style="list-style-type: none"> - The accuracy of the resulting measuring point improves. - The computation requires more time. - Local effects within the facet size cannot be captured 	<ul style="list-style-type: none"> - The measuring point density increases. - The computation requires more time. - Overlapping areas up to 50% are still suitable for representing the measuring results. 	<ul style="list-style-type: none"> - The measuring point density decreases. - The computation requires less time.

Mapping Function

The fundamental principle of Aramis software is based upon the fact that those facets in the undeformed state correspond to those same facets in the deformed state [50].

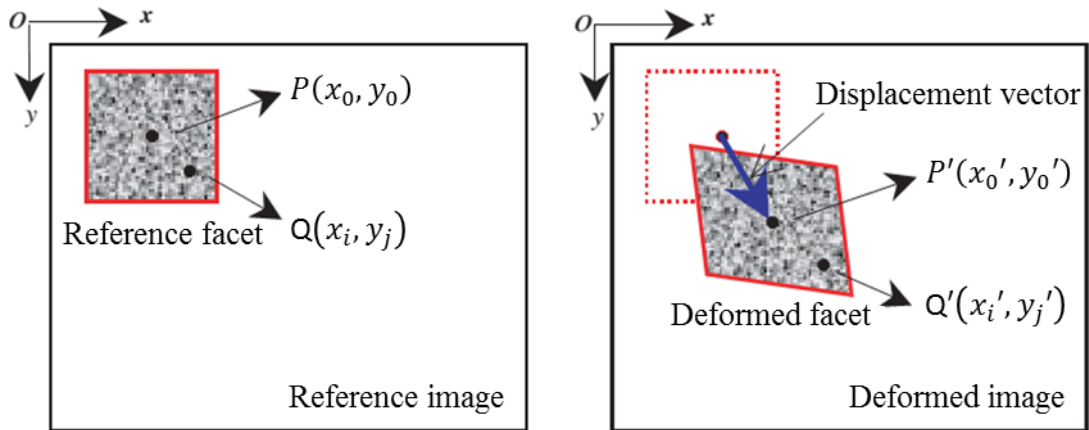


Figure 2-27 Facets in the undeformed and the deformed state [50]

As schematically shown in Figure 2-27, a reference square facet is present in the left image (undeformed state/reference image), and the corresponding deformed facet is shown in the right image. A reference point P is defined in the left image (undeformed state/reference image), which must also be defined as starting point in the second image (deformed state/destination image). The coordinates of point $P(x_0, y_0)$ in the reference facet can be mapped to point $P'(x'_0, y'_0)$ in the deformed facet by the grey values according to the shape function or displacement mapping function [53-54]:

$$P(x_0, y_0) = P'(x'_0, y'_0) \quad (2.1.9)$$

where $P(x_0, y_0)$ and $P'(x'_0, y'_0)$ corresponds to the grey values of initial and destination images respectively. The pixels of the facet in the reference image are then transformed into the deformed image as follows [56]:

$$x'_0 = a_1 + a_2x_0 + a_3y_0 + a_4x_0y_0 \quad (2.1.10)$$

$$y'_0 = a_5 + a_6x_0 + a_7y_0 + a_8x_0y_0 \quad (2.1.11)$$

The values a_1 and a_5 describe the translation of the facet's center and the others describe the rotation and deformation of the facet.

In order to compensate possible differences of illumination in the images, a linear

radiometric transformation is adopted while the images are matched [56]:

$$P(x_i, y_j) = b_1 + b_2 \cdot P'(x'_0, y'_0) \quad (2.1.12)$$

The above parameters (a_1 - a_8 and b_1, b_2) of the geometric and radiometric transformation are calculated in such a way that the sum of the quadratic deviation of the matched grey values is minimized [56].

Correlation Criterion

To evaluate the similarity degree between the undeformed and deformed facets, a cross-correlation (CC) criterion or sum-squared difference (SSD) correlation criterion should be defined before correlation analysis [57]. Those criteria are based on the analysis of the grey scale around the target point and on searching for the most similar pattern in the successive image. The fundamental implicit assumptions are that the grey level approximately remains the same between successive frames and that local texture is able to provide sufficient unambiguous information [50].

The matching procedure is accomplished by searching the peak position of the distribution of correlation coefficient. Once the correlation coefficient extremum is detected, the position of the deformed facet is determined. The differences in the positions of the reference facet center and the deformed facet center generate the in-plane displacement vector at point P, as shown in Figure 2-27. The definitions of correlation criteria can be classified into two groups, including CC criteria and SSD correlation criteria, as shown in Table 2-3 [50].

Table 2-3 Commonly used correlation criterion [50]

Criterion		Definition
CC correlation criterion	Cross-correlation (CC)	$C_{CC} = \sum_{i=-M}^M \sum_{j=-M}^M [f(x_i, y_j) g(x'_i, y'_j)]$
	Normalized cross-correlation (NCC)	$C_{NCC} = \sum_{i=-M}^M \sum_{j=-M}^M \left[\frac{f(x_i, y_j) g(x'_i, y'_j)}{\bar{f} \bar{g}} \right]$
	Zero-normalized cross-correlation (ZNCC)	$C_{ZNCC} = \sum_{i=-M}^M \sum_{j=-M}^M \left[\frac{[f(x_i, y_j) - f_m] \times [g(x'_i, y'_j) - g_m]}{\Delta f \Delta g} \right]$
SSD correlation criterion	Sum of squared difference (SSD)	$C_{SSD} = \sum_{i=-M}^M \sum_{j=-M}^M [f(x_i, y_j) - g(x'_i, y'_j)]^2$
	Normalized sum of squared difference (NSSD)	$C_{NSSD} = \sum_{i=-M}^M \sum_{j=-M}^M \left[\frac{f(x_i, y_j)}{\bar{f}} - \frac{g(x'_i, y'_j)}{\bar{g}} \right]^2$
	Zero-normalized sum of squared difference (ZNSSD)	$C_{ZNSSD} = \sum_{i=-M}^M \sum_{j=-M}^M \left[\frac{f(x_i, y_j) - f_m}{\Delta f} - \frac{g(x'_i, y'_j) - g_m}{\Delta g} \right]^2$

In Table 2-3,

$$f_m = \frac{1}{(2M+1)^2} \sum_{i=-M}^M \sum_{j=-M}^M f(x_i, y_j) \quad (2.1.13)$$

$$g_m = \frac{1}{(2M+1)^2} \sum_{i=-M}^M \sum_{j=-M}^M g(x'_i, y'_j) \quad (2.1.14)$$

$$\bar{f} = \sqrt{\sum_{i=-M}^M \sum_{j=-M}^M [f(x_i, y_j)]^2} \quad (2.1.15)$$

$$\bar{g} = \sqrt{\sum_{i=-M}^M \sum_{j=-M}^M [g(x'_i, y'_j)]^2} \quad (2.1.16)$$

$$\Delta f = \sqrt{\sum_{i=-M}^M \sum_{j=-M}^M [f(x_i, y_j) - f_m]^2} \quad (2.1.17)$$

$$\Delta g = \sqrt{\sum_{i=-M}^M \sum_{j=-M}^M [g(x'_i, y'_j) - g_m]^2} \quad (2.1.18)$$

It should be noted that the CC criteria are related to the SSD correlation criteria. For instance, the ZNCC and the NCC criterion can be deduced from ZNSSD and NSSD correlation criterion, respectively. Besides, for the correlation values obtained from ZNCC or ZNSSD correlation criterion, even a linear transformation of the deformed facet grey intensity is made according to the function $g'(x', y') = a \times g(x', y') + b$, the correlation values remain unchanged. Therefore, it is concluded that the ZNCC or ZNSSD correlation criterion provides the most robust noise-proof performance and is insensitive to the offset and linear scale in illumination lighting. The NCC or NSSD correlation criterion is insensitive to the linear scale in illumination lighting, but it is sensitive to lighting offset. The CC or SSD correlation criterion is sensitive to all lighting fluctuations [50], [58].

Displacement Field Measurement

Since digital images are composed of discrete pixels, the integer displacements with 1-pixel accuracy can be easily obtained. However, the integer pixel resolution is far from that required in many real applications. To further improve displacement measurement accuracy, different sub-pixel registration algorithms can therefore be applied [50].

The 2D DIC method usually requires an accurate initial guess of the deformation before achieving sub-pixel accuracy. For instance, the most commonly used iterative spatial cross-correlation algorithm (the Newton-Raphson method) only converges when an accurate initial guess is provided. Besides initial guess of the deformation vector, sub-pixel displacement registration algorithms, for example, a coarse-fine

search algorithm and peak-finding algorithm, are also required to further improve the accuracy of DIC. There are various algorithms can be used to achieve sub-pixel displacement. However, the most widely used two algorithms are the iterative spatial domain cross-correlation algorithm and the peak-finding algorithms, owing to their simplicity [59].

The Aramis software automatically determines the set of grey values that can minimize the correlation coefficient C value. When a facet is nearly white or black, the correlation coefficient is close to zero. In this case, the correlation criteria cannot match between two successive images and the displacement and corresponding strain data will not be reported. This is regarded as a weak correlation and a 'hole' will be present in the corresponding location in the strain map [50].

Continuity through multi-face matching

When quadratic arrangements of facets are matched simultaneously (multi-facet matching), a higher accuracy for matching can be obtained. As shown in Figure 2-28, the middle one of the nine facets is matched with a higher accuracy than the others, which themselves enjoy a higher accuracy than facets which are matched individually (single facet matching). Multi-face matching guarantees the continuity of the assembly of facets, namely the limiting lines between two facets are equally long. Furthermore, it can be arranged that the individual facets overlap, leading to a greater stability of the group of facets. However, the computation time for a multi-facet matching naturally is longer than for individually matched facets [56].

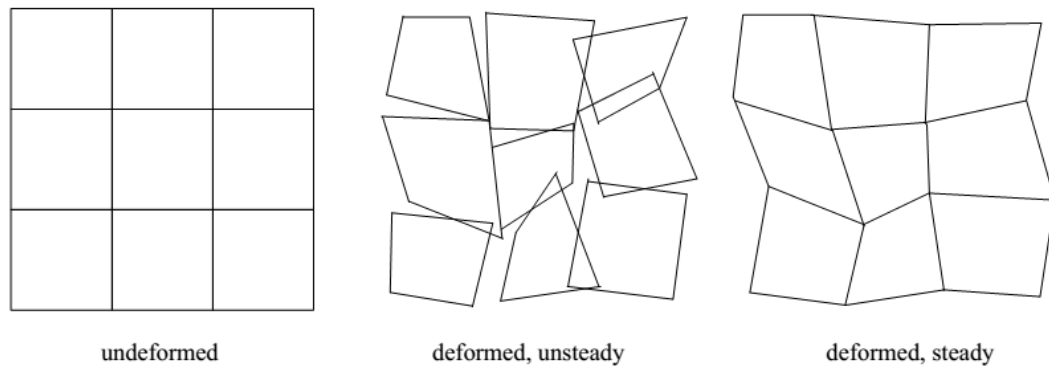


Figure 2-28 Matching of 3x3 facets [56]

The Basics of 2D Strain Computation

For 2D strain computation, displacement and strains will be determined only on the surface of objects. The calculation of the thickness change assumes volume constancy of the materials during loading. Usually the calculated thickness change belongs to a thin area of the materials close to the surface only [55].

Strain is the measure for the deformation of a line element. The stretch ratio λ refers to the relative elongation of an infinitesimal line segment and can be defined as follows [55]:

$$\lambda = \lim_{l \rightarrow 0} \left(\frac{l + \Delta l}{l} \right) \quad (2.1.19)$$

Commonly used strain measures can be defined as the function of stretch ratio λ [55]:

1) Technical or engineering strain

$$\varepsilon_e = f(\lambda) = \lambda - 1 \quad (2.1.20)$$

2) Logarithmic or true strain

$$\varepsilon_T = g(\lambda) = \ln(\lambda) \quad (2.1.21)$$

In order to quantitatively display the deformation of a surface element, the deformation gradient tensor \mathbf{F} is introduced. The deformation tensor transforms a line

element $d\mathbf{X}$ into a line element $d\mathbf{x}$. In both scenarios, the line element connects the same material coordinates. Theoretically, it must be an infinitesimal line element (Figure 2-29). The deformation tensor is defined as follow [55]:

$$d\mathbf{x} = \mathbf{F} \cdot d\mathbf{X} \quad (2.1.22)$$

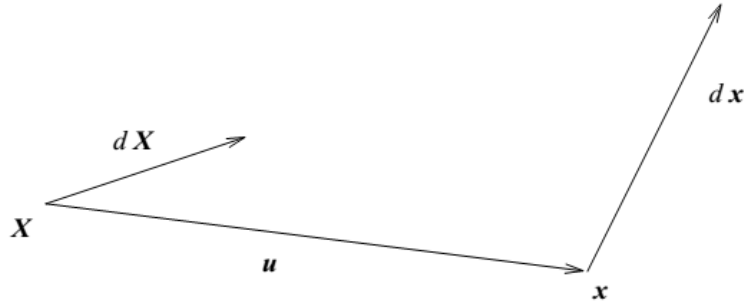


Figure 2-29 Translation (\mathbf{u}) and strain of a line element [55]

One of the disadvantages of the deformation gradient is that rotation and stretch are modeled using one matrix only. This can be overcome by splitting the deformation gradient into two tensors: purely rotation matrix and purely stretch tensor. The matrix can be decomposed into two different ways [55]:

1) Decomposition into rotation \mathbf{R} and right stretch tensor \mathbf{U} :

$$\mathbf{F} = \mathbf{R} \cdot \mathbf{U} \quad (2.1.23)$$

2) Decomposition into left stretch tensor \mathbf{V} and rotation \mathbf{R} :

$$\mathbf{F} = \mathbf{V} \cdot \mathbf{R} \quad (2.1.24)$$

The values ε_x , ε_y and ε_{xy} can be found in the stretch tensor \mathbf{U} :

$$\mathbf{U} = \begin{pmatrix} U_{11} & U_{12} \\ U_{21} & U_{22} \end{pmatrix} = \begin{pmatrix} 1 + \varepsilon_x & \varepsilon_{xy} \\ \varepsilon_{xy} & 1 + \varepsilon_y \end{pmatrix} \quad (2.1.25)$$

For the interpretation of the values ε_{xy} , the shear angle γ_{xy} is used. The shear angle describes the change of an angle of 90° in the undeformed state to a new angle in the deformed state. It should be noted that the equation $\varepsilon_{xy} = \frac{1}{2}\gamma_{xy}$ is not valid for large

strain values since the assumption is only valid for the small strain from the elastic strain theories.

The strain measurements ε_x and ε_y are dependent on the coordinate system. To eliminate this disadvantage, major and minor strain values can be computed. The symmetrical matrix \mathbf{U} can be transformed to the main diagonal form. The two eigenvalues λ_1 and λ_2 can be calculated below [55]:

$$\lambda_{1,2} = 1 + \frac{\varepsilon_x + \varepsilon_y}{2} \pm \sqrt{\left(\frac{\varepsilon_x + \varepsilon_y}{2}\right)^2 - (\varepsilon_x \cdot \varepsilon_y - \varepsilon_{xy}^2)} \quad (2.1.26)$$

Based on the values from the calculation, the larger eigenvalue corresponds to the major strain and the smaller eigenvalue corresponds to the minor strain. In this way, the strain values are independent of the coordinate system.

If the material thickness is small compared to the entire surface, it is necessary to deduce the remaining material thickness from the deformation of the surface. In other words, the third principle strain can be calculated from the major and minor strain, given the assumption of a constant volume. The volume constancy being expressed by the relationship between the stretch ratios is as follows [60]:

$$\lambda_1 \cdot \lambda_2 \cdot \lambda_3 = 1 \quad (2.1.27)$$

The effective strain is frequently needed. The effective strain can result from the formula below according to von Mises:

$$\varepsilon_E = \sqrt{\frac{2}{3}(\varepsilon_{xx}^2 + \varepsilon_{yy}^2 + \varepsilon_{zz}^2) + \frac{1}{3}(\gamma_{xy}^2 + \gamma_{yz}^2 + \gamma_{zx}^2)} \quad (2.1.28)$$

where ε_{xx} is the normal strain component along the x-axis, ε_{yy} is the normal strain component along the y-axis, ε_{zz} is the normal strain component along the z-axis, and γ_{xy} , γ_{yz} and γ_{zx} represent the shear strain components on the x-y, y-z and x-z planes,

respectively. In the 2D Aramis system, only ε_{xx} , ε_{yy} and γ_{xy} can be determined.

Assume the constant volume conditions is valid, i.e. $\varepsilon_{xx} + \varepsilon_{yy} + \varepsilon_{zz} = 0$, and that γ_{yz} and γ_{zx} are zero. Therefore, the equivalent strain can be obtained below:

$$\varepsilon_E = \sqrt{\frac{4}{3}(\varepsilon_{xx}^2 + \varepsilon_{xx}\varepsilon_{yy} + \varepsilon_{zz}^2) + \frac{1}{3}\gamma_{xy}^2} \quad (2.1.29)$$

The computation size includes the adjacent points around a point in the strain calculation. The default parameter of computation size in linear strain is 3. This means that a 3x3 field of 3D points is used to calculate the strain value of the center point. This setting is particularly appropriate for the assessment of local strain. When the computation size is increased, the noise decreases but there will be less strain being calculated in the marginal area. If all adjacent points do not exist for a calculation, the strain for the center point can still be calculated. The validity quote determines how many points must exist for calculation. For instance, a quote of 100% means that all 9 points (for a field of 3x3) must exist [55].

2.3.2.4 2D Microscopic DIC (μ -DIC) Uniaxial Tensile Test Coupled with SEM

Understanding the influence of microstructure on the macroscopic behavior of materials required new experimental techniques to track full-field deformations on small length scales with high spatial resolution (mico/nano-scale) [59, 61]. To fulfill this requirement, the application of DIC method has been combined with high-magnification imaging systems, including an atomic force microscope (AFM), SEM, or an optical microscope. While AFM can provide images with very high spatial resolution, it is very difficult to set up a loading stage underneath the AFM scanning probe due to space limitations. The spatial resolution of an optical imaging device is determined by its diffraction limit. SEM can provide a wide range of magnifications from x10 to x500000 according to working distance with relatively larger space inside

the chamber to work with [59-60].

Microscopic DIC (μ -DIC) technique coupled with SEM is very powerful and versatile, and it enables the acquisition of an abundant information in nano/micro-scale level. For instance, it can link in-situ deformation behavior directly to the underlying crystallography of the material when coupled with electron backscattered diffraction (EBSD) microstructure mapping, and characterize of the microstructural strain distribution between phases [60], [64].

Although μ -DIC SEM methodology enjoys many advantages, it also introduces challenges which are far more complex than those encountered in macro-scale DIC techniques. The first challenge is to create a suitable tracking pattern for micro-scale specimens. Besides, μ -DIC SEM also requires careful correction of distortions that are inherent to SEM imaging [64]. Additional challenges include a limitation on the size of the specimen, the size of straining stage which can fit inside of the SEM chamber, and sample charging for non-conducting samples. The SEM introduces more image noise compared to optical imaging. Finally, SEM usage and patterning methods can be expensive [60].

Those two main challenging problems μ -DIC SEM of will be discussed in detail below.

Small-scale Patterning Methods

Anisotropic, high contrast and the random surface pattern are required for DIC measurements. The pattern can be natural surface features, such as the surface polished steels after etching, or artificially applied patterns. Kammers et al. compared some common patterning techniques for μ -DIC SEM in Table 2-4 below [60].

Table 2-4 Summary of patterning techniques for μ -DIC SEM [60]

Technique	Advantages	Disadvantages
Focused ion beam patterning (FIB)	<ul style="list-style-type: none"> - Accurate control of pattern location - Repeatable - Substrate-independent 	<ul style="list-style-type: none"> - Expensive - Time consuming - Ion beam surface damage
Template patterning	<ul style="list-style-type: none"> - Fast and efficient - Inexpensive - Repeatable - Accurate control of pattern location - Substrate-independent 	<ul style="list-style-type: none"> - Filter must be held perfectly flat to the surface of the sample - Stock filter pore aspect ratio limits the minimum feature size to 400 nm - Low pore density in stock filters requires numerous applications
Nanoparticle patterning	<ul style="list-style-type: none"> - Fast - Inexpensive - Can be stock purchased with diameters ranging from 2 to 250 nm - Easily synthesized - Broad distribution of speckle sizes 	<ul style="list-style-type: none"> - Difficult to control pattern location - Difficult to achieve repeatable results - Substrate-dependent
E-beam lithography	<ul style="list-style-type: none"> - Accurate control of pattern location - Repeatable - Easily scaled for different magnifications - Suitable for high temperature - Substrate-independent 	<ul style="list-style-type: none"> - Expensive - Time consuming - Multi-step process

All of the patterning techniques which can provide good quality pattern must satisfy the requirements below [48]:

- 1) They should be clearly discernible;
- 2) The pattern should be dense and precise and smaller than the facet size;
- 3) There should be little damage to the specimen surface.
- 4) Adhesion between pattern and surface and should be maintained during deformation;

Error Introduced by SEM Imaging

SEM systems record images by raster-scanning an electron beam across a specimen

surface. Figure 2-30 shows a schematic of a typical SEM system. After electron beam (e-beam) generation in a thermal emission gun or field emission gun (FEG), the e-beam passes through a series of electromagnets and is focused onto the specimen surface [63].

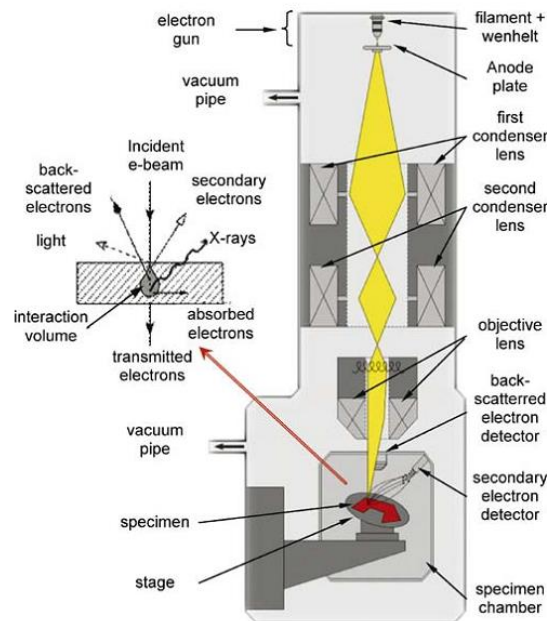


Figure 2-30 Schematic of a typical SEM and imaging process [63]

The e-beam rastering process and conversion to a digitized image in SEM is shown in Figure 2-31. The e-beam rastering proceeds by scanning horizontally on specimen surface with a dwell time. Beam dwell time at each pixel position along row is preset. A delay time between scanning rows is required to reset the e-beam. Either secondary electron detector or back-scattered electron detector can be used to record the SEM image [65].

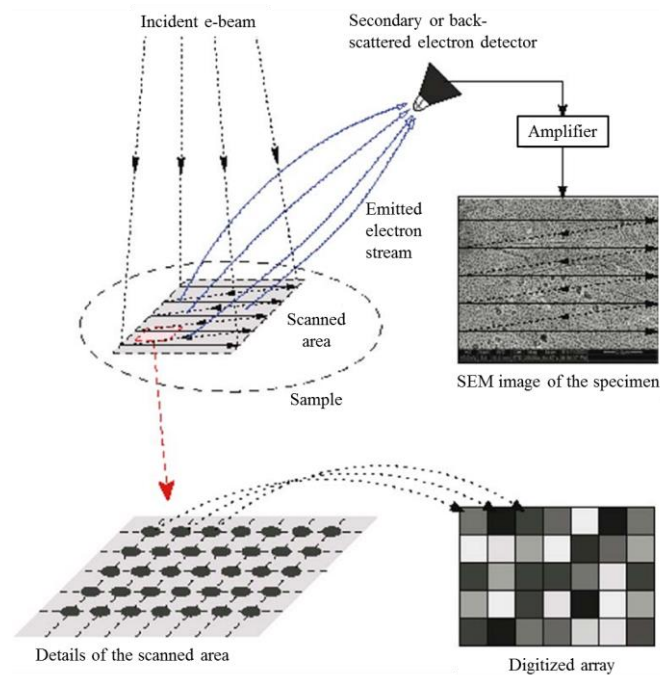


Figure 2-31 Schematic of typical image formation process in a SEM [65]

In an SEM system, e-beam steering during the scanning process is realized through electromagnetic lenses. A typical modern SEM system is open loop on e-beam position. In other words, the e-beam position is not a control parameter. Therefore, positional errors will be generated during the scanning process due to environmental and system variables. Variables may include combinations of the following factors: electromagnetic field variable fluctuations, time shifts between scan lines, beam positioning variations, scan distortions, and environmental factors (e.g., thermal fluctuations, mechanical vibrations, air currents) [63].

The time-varying drift and spatial distortions can introduce inaccurate strain and displacement data, and it is critical that they are correctly accounted for when performing μ -DIC SEM experiments. In addition to distortions, SEM images can suffer from more noise than optical images, which limits the minimum discernible displacement measurements.

3 Materials Processing

The steels investigated in this project are provided by CanmetMATERIALS. The processing and baseline properties of this material are described by Scott et al. [66]. In order to compare the effects of vanadium, two compositions were designed. The measured compositions and their designations are shown in Table 3-1. C is an austenite stabilizer and it can strengthen the martensite. Si can facilitate ferritic transformation. Mn also can stabilize the austenite and it can strengthen the ferrite by solid solution. It also retards ferrite formation. V is added to refine the microstructure. A relatively higher N addition (0.008 wt%) is used to promote V(C, N) precipitation. Mo and Cr can inhibit pearlite and bainite formation. The Al content was kept as low as possible to reduce AlN precipitation [19], [66].

Table 3-1 Chemical compositions of studied DP steels (in wt%)

Steel	C	Si	Mn	V	N	Mo	Cr	Al
DP: Ref	0.23	0.19	1.59	0.003	0.008	0.009	0.027	0.011
DPV: Ref + V	0.21	0.19	1.65	0.14	0.008	0.01	0.032	0.019

The thermomechanical processing routes to produce the studied DP steels are plotted in Figure 3-1. Ingots with 130 mm thick were hot rolled in the CanmetMATERIALS pilot mill. To guarantee a high finishing rolling temperature (900°C), nine passes were applied to roll the ingot from 130 mm to 15 mm thick. The material was reheated to 1240°C and plates with 15 mm thickness was rolled to 3 mm in 5 passes, followed by forced air cooling rate at 13°C/s to a coiling temperature 450°C and then slow cooling at 60°C/h to room temperature. The hot bands were then cold-rolled 67% from 3 mm to 1 mm under tension in 7 passes using the CanmetMATERIALS pilot rolling mill. The plates supplied to McMaster were then annealed at different temperature and time (750°C/120s for DP and 760°C/90s for DPV) using an annealing simulator and cooled

by fast die quenching.

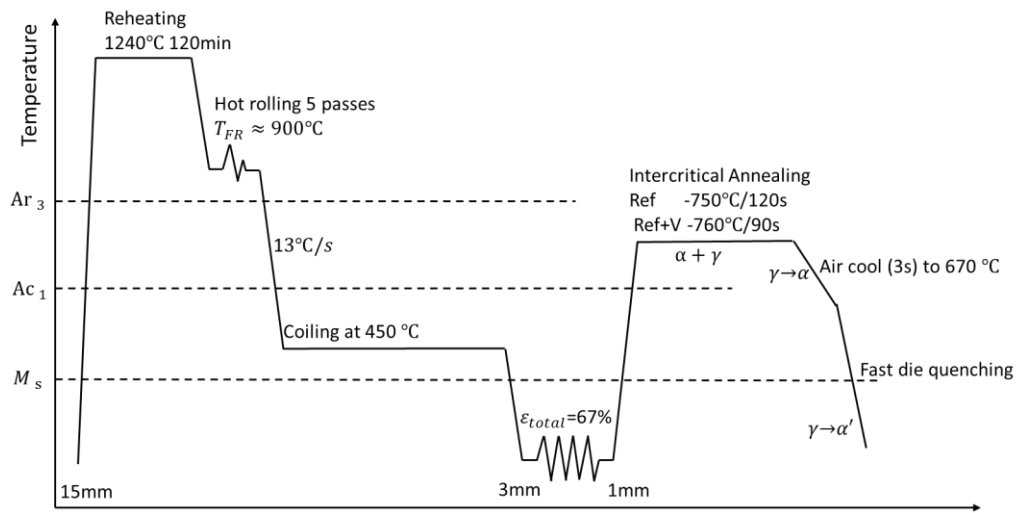


Figure 3-1 Schematic diagram of processing routes to produce DP steels in CANMET

4 Experimental Procedure

Two high-strength sheets of DP1300 steel, named DP and DPV, were studied in this research. The sheet thickness was 1 mm. The experimental procedures for sample preparation, sample characterization, digital image correlation (DIC) tensile test, and fractography are presented in this chapter.

4.1 Metallography

Samples were cut using a Struers Precision Saw for microstructural analysis. They were cold-mounted in epoxy and prepared using a Struers Automatic Polisher. Firstly, samples were grounded with 400, 600, 800, and 1200 grit silicon carbide abrasive. Next, samples were polished with 3 μm and 1 μm diamond abrasive and 0.04 μm colloidal silica suspension (OPS). Finally, samples were etched with 2% nital for 10 s at room temperature. Scanning electron microscopy (SEM) was performed using a JEOL JSM-7000F.

4.2 Transmission Electron Microscopy (TEM)¹

Nano-scaled observations were realized by using transmission electron microscopy (TEM) in this research. TEM analysis was carried out at CanmetMATERIALS using a Tecnai Osiris 200 keV FEG-STEM equipped with a Gatan Enfina electron energy loss spectroscopy (EELS) system and four windowless Super-X SDD EDX detectors for chemical mapping. Samples were prepared from thin foils using electro-polishing with A8 solution and from both direct and indirect extraction replicas.

¹ The TEM experiments were performed by Dr. Babak Shalchi-Amirkjiz at CanmetMATERIALS

4.3 DIC Tensile Test

In order to avoid deteriorating the properties of the investigated materials, micro-tensile samples were machined through milling rather than electro-discharge machining (EDM).

4.3.1 Macroscopic uniaxial DIC Tensile Tests

Macroscopic uniaxial DIC tensile tests were performed on DP and DPV steels along both the rolling and transverse directions (RD and TD) using an MTS Landmark Servo-hydraulic test system with a 5 kN load cell at CanmetMATERIALS. Due to limited amount of materials available, micro-tensile specimens with a straight gauge length were used in this study (Figure 4-1). The specimens were sectioned from the sheets subjected to milling.

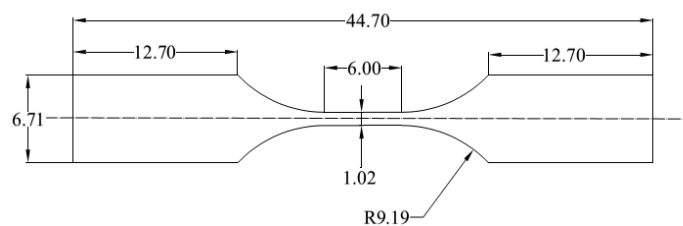


Figure 4-1 Dimensions of micro-tensile specimen

Specimens were ground with 600 grit silicon carbide abrasive papers to remove oxide layers on the surface. A stochastic ink-pattern was sprayed on the gauge length of each specimen (Figure 4-2). Uniaxial DIC tensile tests were run at a displacement rate of 0.216 mm/min which gave a strain rate 6×10^{-4} /s. The data acquisition rate of the tensile machine is one frame per second, which is the same as the frame rate of the camera. During the experiments, the tensile machine recorded the loading force and the camera recorded the images, respectively.

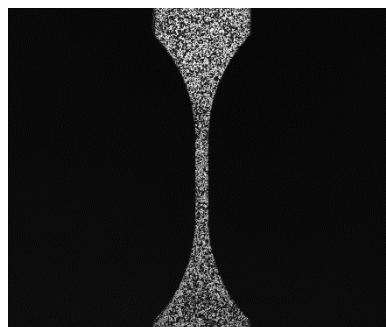


Figure 4-2 Photos of micro-tensile specimen with stochastic pattern

4.3.2 Microscopic In-situ Tensile Tests through Scanning Electron

Microscope (SEM)

Microscopic in-situ tensile tests were performed using the SEM JEOL JSM-7000F. An hourglass-shaped specimen was designed to guarantee that fracture occurs within a small window inside the imaging region. The geometry of the tensile specimens for in-situ tensile tests is illustrated in Figure 4-3.

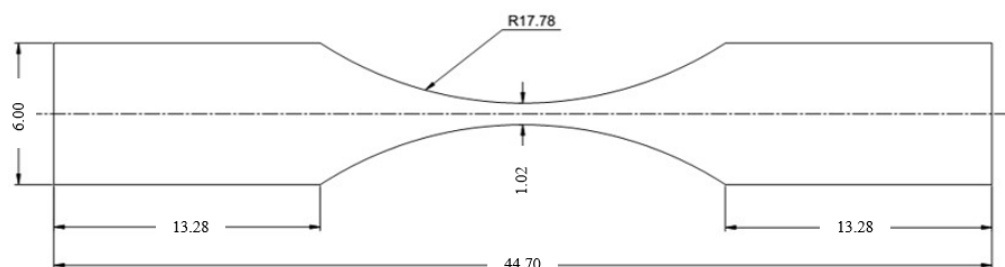


Figure 4-3. Dimension of micro-tensile hourglass-shape test specimen

4.3.2.1 Specimens Geometry Design

The geometry of the micro-tensile hourglass-shape test specimen was developed by using finite element simulations through ABAQUS. Four-point plane stress shell elements and the von Mises yield criterion were applied for the analysis. True stress and plastic strain from experimental data were used as input and true strain

distribution along the surface was exported. For the designed geometry, the finite element analysis shows that up to the necking strain, the strain distribution is uniform in a region around 2 mm long in the middle of the specimen (Figure 4-4). No strain concentration occurred.

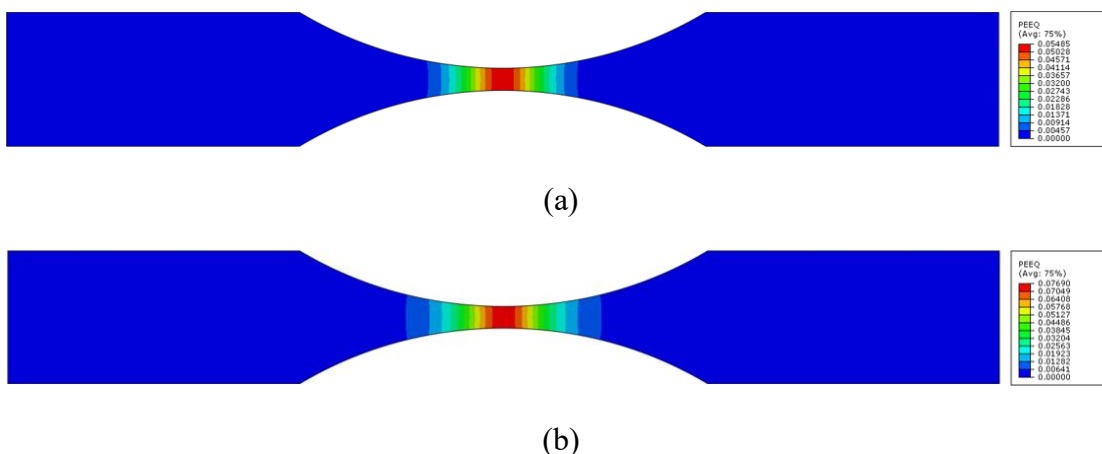


Figure 4-4 Strain distribution along the proposed specimen geometry through finite element analysis. The strain presented here is the von Mises effective strain (a) Reference steel, (b) Vanadium added steel

4.3.2.2 Tensile Specimens Preparation

The micro-tensile specimens were sectioned from the sheets subjected to milling. Micro-tensile specimens were glued on the jigs and then ground and polished through the auto-polishing machine. Figure 4-5 shows the automatic polishing jigs for preparing specimens.



Figure 4-5 Micro-tensile specimens on automatic polishing jigs

The metallographic procedures are shown below:

Grinding:

The side of the specimens was also ground to remove the oxide layer. Both surfaces of the tensile specimens were ground with 400, 600, 800, 1200 grit silicon carbide abrasive papers lubricated with flowing water. The tensile specimens were then cleaned with anhydrous ethanol in the ultrasonic bath followed by blow drying in hot air.

Polishing:

1. Specimens were polished on MD-Dur cloth with 3 μ m diamond abrasive for 8 minutes using a water-free lubricant followed by flowing water cleaning, anhydrous ethanol cleaning and blow drying in hot air;
2. Specimens were polished on MD-Nap cloth with 1 μ m diamond abrasive for 8 minutes using water-free lubricant followed by flowing water cleaning, anhydrous ethanol cleaning and blow drying in hot air;
3. Specimens were polished on MD-Chem cloth with a solution made with 50% 0.04 μ m colloidal silica suspension (OPS) and 50% ethylene glycol for 1.5 minutes lubricated by water followed by flowing water cleaning, ethylene

glycol cleaning, anhydrous ethanol cleaning and blow drying in hot air.

Etching:

In order to reveal the microstructures, the specimens were then immersed in freshly made 4% nital for 12 s with agitation. The tensile specimens were then cleaned with methanol in the ultrasonic bath followed by blow drying in hot air to remove any chemical residue on the surface.

The middle section of the tensile specimen was then indented using a CLEMEX Vickers's micro-hardness indenter. 13 diamond-shaped indentations were made in the middle of the tensile specimens parallel to the loading direction over a total length of 1000 μm (Figure 4-6). The indents were used as a reference to track the selected locations.

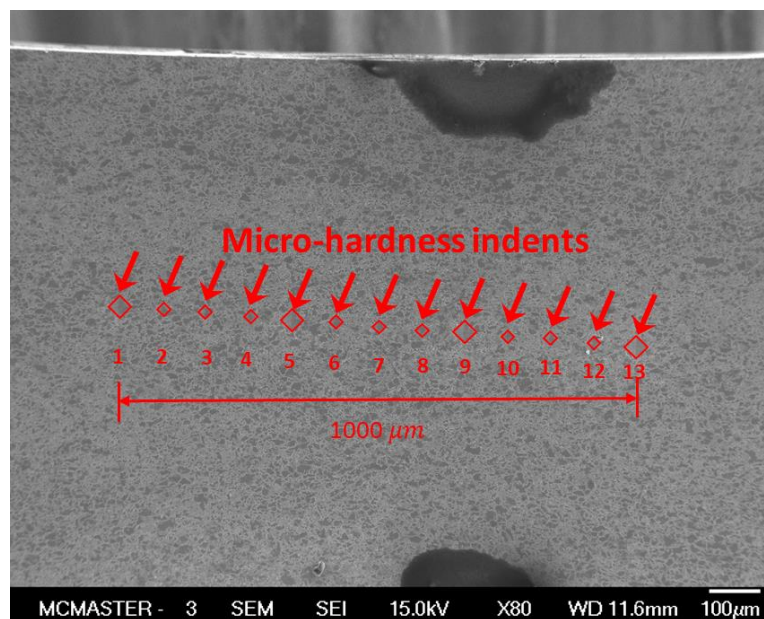


Figure 4-6 SEM images showing micro-hardness indents on specimen surface

4.3.2.3 In-situ SEM Tensile Testing

All SEM imaging in this project was performed in the Canadian Center Electron Microscopy at McMaster University. A simple manual tensile jig (Figure 4-7) was

made to perform the in-situ uniaxial tensile tests within a SEM JEOL JSM-7000F chamber on four micro-tensile specimens (DP RD, DP TD, DPV RD, and DPV TD), respectively. High vacuum mode with secondary electron detector was used.

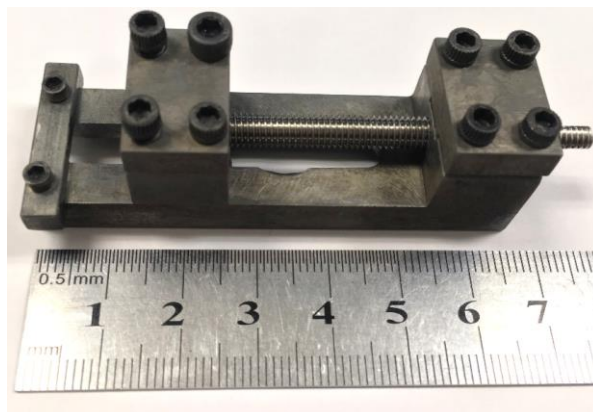


Figure 4-7 Manual tensile jig for in-situ tensile test coupled with SEM

Figure 4-8 shows a side view of the tensile jig used in this project. The tensile specimen was put on the tensile jig and then the assembly was installed on the SEM stage. It then was inserted into field emission SEM (FE-SEM) chamber.

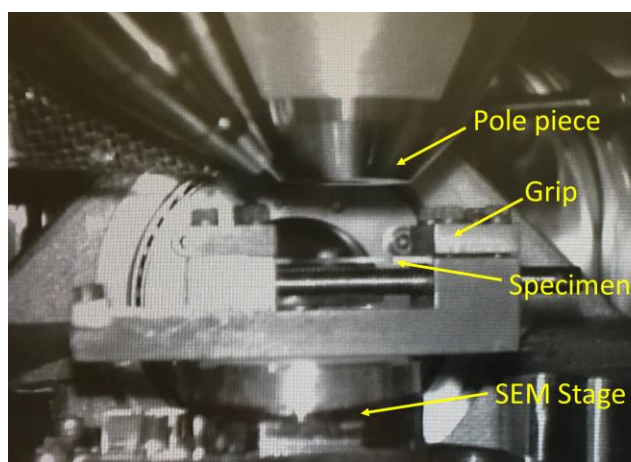


Figure 4-8 Manual tensile jig in FE-SEM chamber

The parameters of the e-beam for taking micrographs within FE-SEM are as follows: 15 kV accelerating voltage, medium probe current 6, and SEM mode 3. The working

distance (WD) and magnifications differed from sample to sample because of the variation of each sample. All those parameters were maintained throughout each in-situ tensile test. Several images were taken at different locations on each sample. All the image array shared an image size of 2560 x 2048 pixels, this data corresponds to an image acquisition time 80s. The first SEM images were taken when the tensile specimen was undeformed. Next, the assembly was taken out of the FE-SEM chamber and the tensile specimen was pulled a small strain amount. And then the assembly was inserted into FE-SEM chamber again to take the second image at the same locations. The procedure was repeated until the tensile specimen was fractured.

4.3.2.4 Strain Calculation

The series of SEM micrographs were input into Aramis software for strain analysis.

4.4 Fractography

Fractured samples of DP RD and DPV RD were observed in the SEM JEOL 6610LV using secondary electron beam imaging at an accelerating voltage 5 kV.

4.5 Quantitative Methods

4.5.1 Microstructural Analysis

The grain size of ferrite (S_F) and volume fraction of martensite (V_M) were quantitatively analyzed in this study. A series of SEM images were taken through the thickness of samples and then Image J software was used for calculation.

4.5.1.1 Mean Grain Size of Ferrite

The mean grain size of ferrite was determined according to the ASTM E1382-97 [67]. The 95% confidence interval (95% *CI*) of each grain size measurement is determined by:

$$95\% CI = \pm \frac{t \cdot s}{\sqrt{N}} \quad (4.5.1)$$

where t is an 95% CI interval multiplier as a function of the number of fields n , s is the standard deviation, and N is the number of grain intercept lengths.

The percent relative accuracy, % RA , of each grain size measurement is calculated by:

$$\% RA = \pm \frac{95\% CI}{\overline{S_F}} \cdot 100 \quad (4.5.2)$$

where $\overline{S_F}$ is the mean value of measured grain size?

The mean grain size of ferrite estimate is presented as:

$$S_F = \overline{S_F} \pm 95\% CI \quad (4.5.3)$$

According to the standard, when % $RA \leq 10\%$, the measuring precision is acceptable.

To obtain reasonable precision, there are the following rules:

- At least five fields are needed ($n \geq 5$)
- There should be more than 50 grains within one field
- At least 500-grain intercept lengths are measured ($N \geq 500$)

In this study, both the grain size of ferrite along rolling direction (RD) and normal direction (ND) were measured. Seven fields were measured for DP and five fields were measured for DPV.

4.5.1.2 Volume Fraction of Martensite

The volume fraction of martensite was determined according to the ASTM E562-11 [68].

The 95% confidence interval (95% CI) of each volume fraction measurement is determined by:

$$95\% CI = t \times \frac{s}{\sqrt{n_{field}}} \quad (4.5.4)$$

where n_{field} refers to the number of fields, t is an 95% *CI* interval multiplier as a function of n_{field} , and s is the standard deviation.

The percent relative accuracy, % *RA*, of each grain size measurement can be obtained as:

$$\% RA = \frac{95\% CI}{\overline{P_p}} \cdot 100 \quad (4.5.5)$$

where $\overline{P_p}$ is the mean value of measured volume fraction of each field?

The volume percentage of martensite estimate is presented as:

$$V_M = \overline{P_p} \pm 95\% CI \quad (4.5.6)$$

4.5.2 Nano-hardness Measurements²

Nano-indentation studies were conducted through an Anton Paar Nano-indentation Tester (UNHT) at an indentation load of 5000 μ N. Square arrays, 8×8 and 4×4 , of indents were carried out with a 8 μ m indent separation and the indented phase was revealed using optical imaging after a light Nital etching (Figure 4-9). The measurements were performed at room temperature with a diamond Berkovich indenter by applying increasing indentation force at a constant rate (30000 μ N/min) and simultaneously recording the indentation depth. It should be noted that only indents which were located completely within phase boundaries were used for data quantification. Based on this around 83% of the measurements were considered.

² The nano-hardness tests were performed by Dr. Javad Samei at the University of Toronto

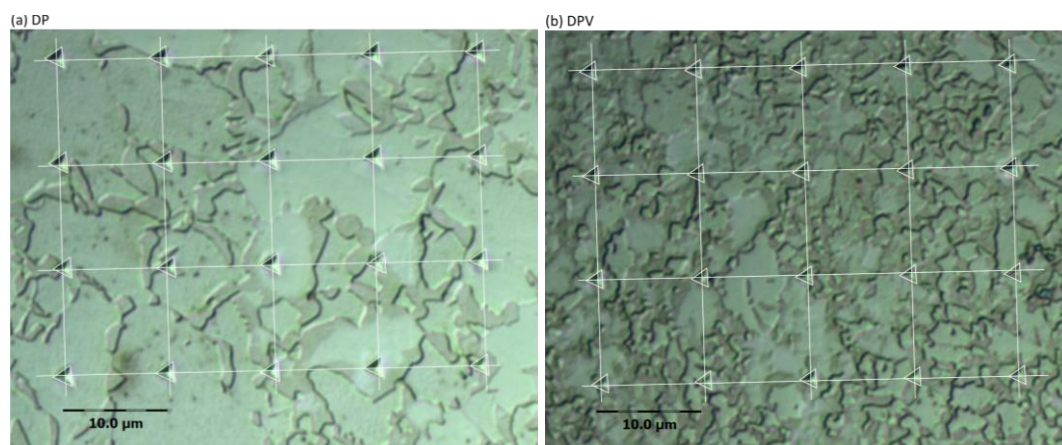


Figure 4-9 Optical image of the nano-indentated region in both steels: (a) DP steels; (b) DPV steels.

4.5.3 Strain Analysis of In-situ Tensile Test Coupled with SEM

Micrographs obtained from in-situ uniaxial SEM tensile tests were analyzed using the Aramis software. Those images were converted to grey scale and then input into the system to perform local strain calculations. The step size for four sets of specimens was adjusted to similar values to allow data to be comparable with each other under different magnification.

4.5.4 X-ray Computed Tomography (X-ray CT) Scans³

The fracture tensile samples were scanned on a Bruker Skyscan1172 X-ray computed tomography (XCT) scanner for quantitative analysis of microstructural damage. The system was equipped with a 100 kV X-ray source with an Al/Cu filter. The scans were performed at the high-resolution mode with a resolution of 0.7 μm/pixel. The sample was rotated over 360° and 720 images were taken for image analysis. By taking account the resolution of the images and to those artifacts during the post-processing of images, only those objects with a minimum volume of 13.8 μm³ were used for

³ The X-ray CT tests were performed by Dr. Javad Samei in McMaster Automotive Research Center

analysis. 3D reconstruction of the fractured specimens were built through tomographic images and the location of voids and dimples were presented in the models. The commercial Skyscan1172 software package was used for post-processing of images, quantitative analysis and 3D reconstruction.

5 Results and Discussion

This chapter will discuss all the experimental findings in this project, including microstructural characterization, macroscopic and microscopic mechanical behaviour analysis, nano-hardness measurements, and fracture surface analysis.

5.1 Microstructures

Figure 5-1 shows SEM images of DP-ref steels and DP-V steels at different magnifications. Those islands which are protruding correspond to martensite. The ferrite and martensite phases are relatively uniformly distributed for both variants. The martensite phase in both steels is continuous and forms a skeleton structure. There are more ferrite/martensite (α/α') interfaces than ferrite grain boundaries for both materials. Because of cold rolling, the microstructures are elongated along the rolling direction. Despite the different chemical composition and varied intercritical annealing parameters, the martensite content in both steels is similar (around 50% α'). This makes it possible to analyze the influence of V addition on ductility through microstructural modification. The volume fraction of martensite (V_M) and grain size of ferrite (S_F) are listed in Table 5-1. Scott [69] measured the martensite of both of the DP-ref and DP-V steels produced under the same conditions from optical images. He found the martensite volume fraction of DP-ref steel to be 30-31%, which is lower than the value measured here ($49.0\pm 2.6\%$). The differences between these two groups of data might be explained from the heterogeneity of the DP-ref steel. The martensite volume fraction of the DP-V steel measured by Scott [69] is 50-65%, which overlaps the value measured here ($50.3\pm 1.7\%$).

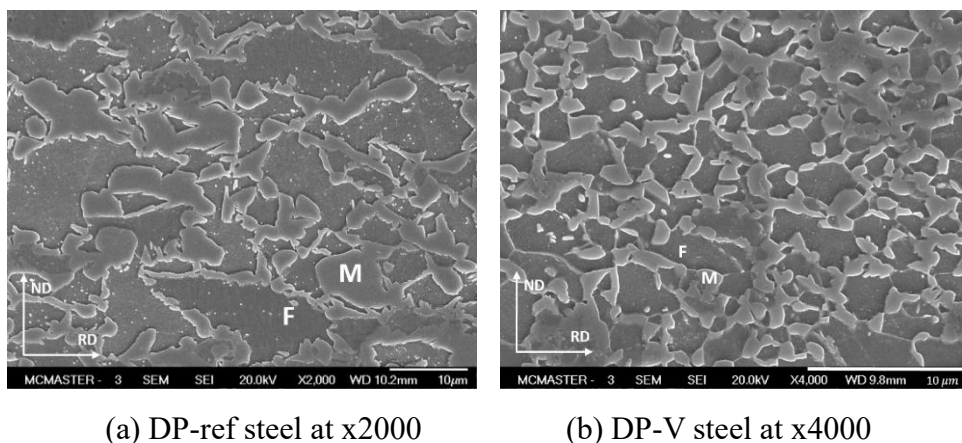


Figure 5-1 SEM micrographs of ferrite-martensite DP steels. (F: ferrite; M: martensite; ND: normal direction; RD: rolling direction)

Vanadium additions introduce profound grain refinement for α/α' DP steels. Scott [66] proposed that this is caused by Zener pinning of newly recrystallized ferrite by V(C, N) precipitates nucleated on dislocations during the heating stage before intercritical annealing. Both ferrite size and martensite size are significantly reduced. The ferrite grain size is reduced in both the rolling direction and the normal direction by about a factor of three. It is difficult to quantitatively analyze the reduction of martensite size when martensite forms a skeleton structure and there is no distinct interface between martensite islands. However, according to the microstructural images, it can be concluded that the refinement of the martensite is of the same order as the ferrite grain refinement.

Table 5-1 Microstructure parameters obtained from SEM micrographs

Steel	Martensite Volume Fraction V_M (%)	Ferrite Grain Size S_F (μm)	Aspect ratio
DP-ref	49.0 \pm 2.6	//RD: 4.8 \pm 0.4 //ND: 2.9 \pm 0.2	1.66
DP-V	50.3 \pm 1.7	//RD: 1.6 \pm 0.1 //ND: 0.8 \pm 0.1	1.90

Introducing vanadium into DP steels generates a more homogenous microstructure.

This was studied by measuring V_M inside different statistical volume elements (SVEs).

SVEs were randomly selected in both steels in the area where the local martensite volume fraction was around 50%. Figure 5-2 illustrates how SVEs overlapped on the microstructures and the corresponding calculation results are listed in Table 5-2. Point counting method was employed. As shown in Table 5-2, when excluding SVE1, the V_M in the smaller SVEs of DP-V steel converges to the average value, but V_M in the DP-ref steel does not. The size of SVE1 is close to the grain size, and hence cannot be used for comparison with other SVEs here. This examination of the microstructures suggests that DP-V steel with a finer scale has a more homogeneous microstructure, so that even a small SVE window can represent reasonable characteristics of the whole microstructure.

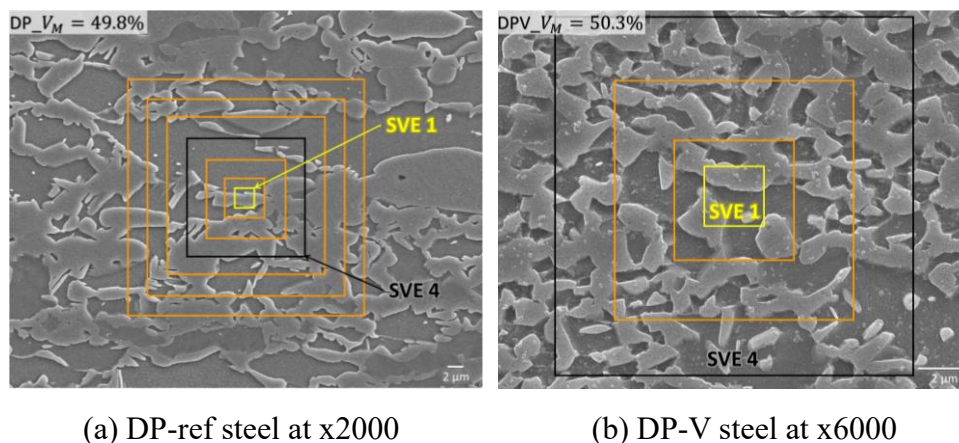


Figure 5-2 SVEs in SEM micrographs

Table 5-2 V_M inside each SVE of DP-ref and DP-V steels

	SVE1	SVE2	SVE3	SVE4	SVE5	SVE6	SVE7
SVE size (μm)	2.5x2.5	5x5	10x10	15x15	20x20	25x25	30x30
DP-ref steel (%)	50.0	40.0	43.4	42.9	42.3	46.1	47.6
DP-V steel (%)	57.1	46.9	52.8	48.3	-	-	-

The SEM micrographs used for measuring martensite volume fraction was taken through the sample thickness (1 mm). To identify each phase clearly, a magnification of x2000 was used for the DP-ref sample, and a magnification of x4000 was used for the DP-V sample. The individual results for each location are shown in Figure 5-3. It should be noted that the martensite volume fraction near the sample surface is much lower than elsewhere. The distribution of martensite through the thickness is quite uniform except near the surface. Therefore, the data which is near the sample surface (within 100 μm) was discarded. Lower martensite content near the sample surface is caused by decarburization during high-temperature heat treatment and thus carbon near the steel surface was removed due to the reaction with CO gas. There are 20 images used for this calculation in DP-ref steels and 29 images used for the calculation in DP-V steels.

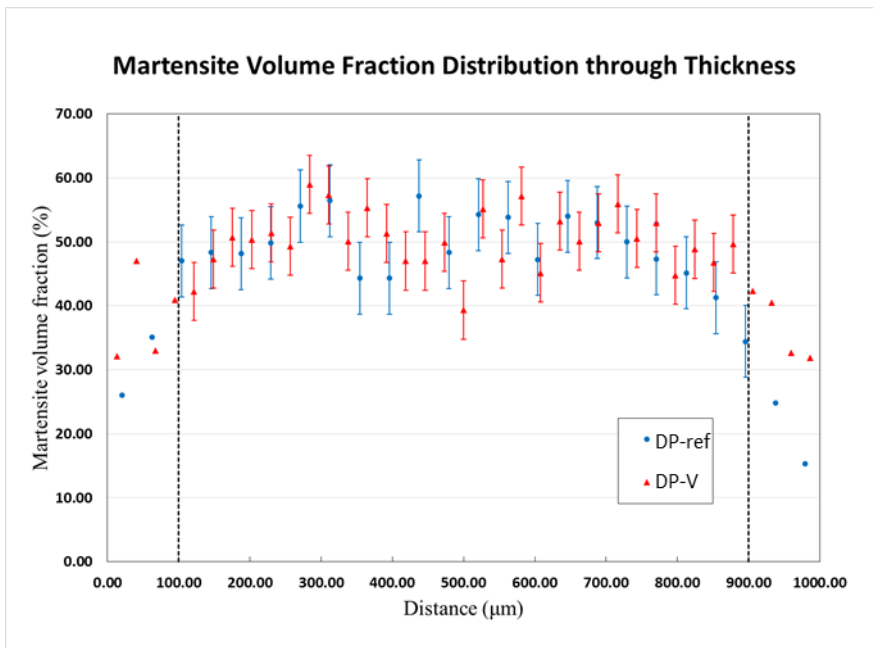
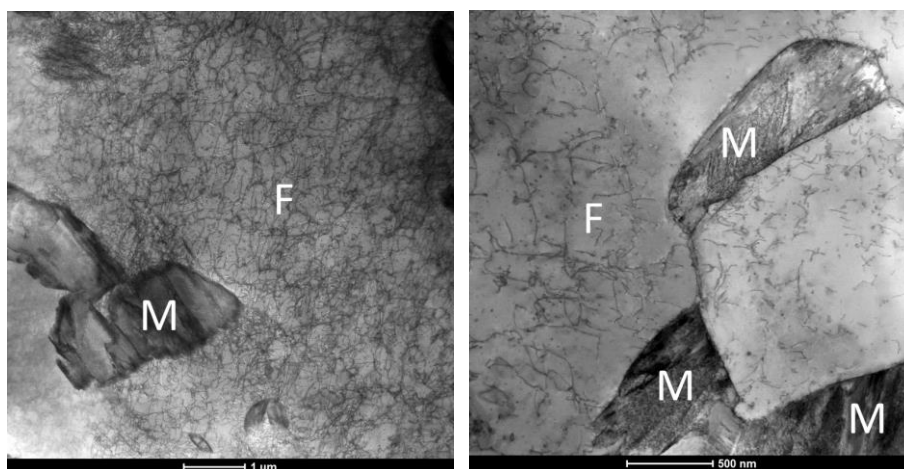


Figure 5-3 Martensite volume fraction distribution through sample thickness

The bright field (BF) scanning transmission electron microscopy (STEM) images are shown in Figure 5-4. Regions of the specimen which enjoy higher density can scatter more strongly, and will appear darker in the BF image [70]. There are more carbon atoms in the martensite phase compared to ferrite phase and martensite should present a lath structure when the carbon content in the steel is around 0.2 wt%. We can identify martensite islands from the BF images by their darker color. There are abundant dislocations present in ferrite phase because of internal stresses generated during the austenite-to-martensite transformation.

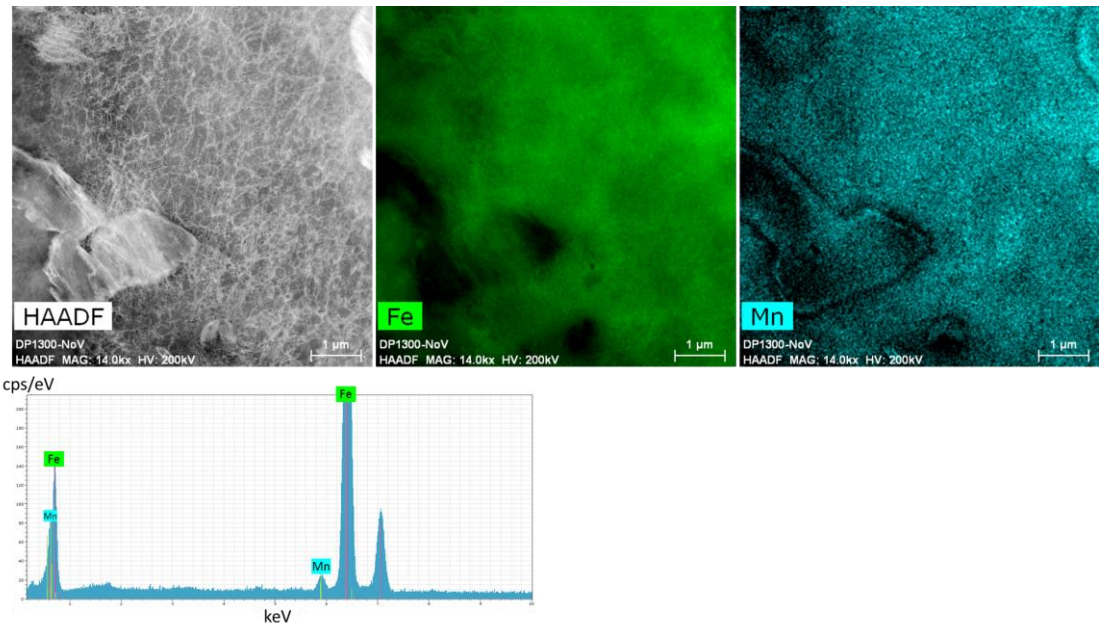


(a) DP-ref DP steel

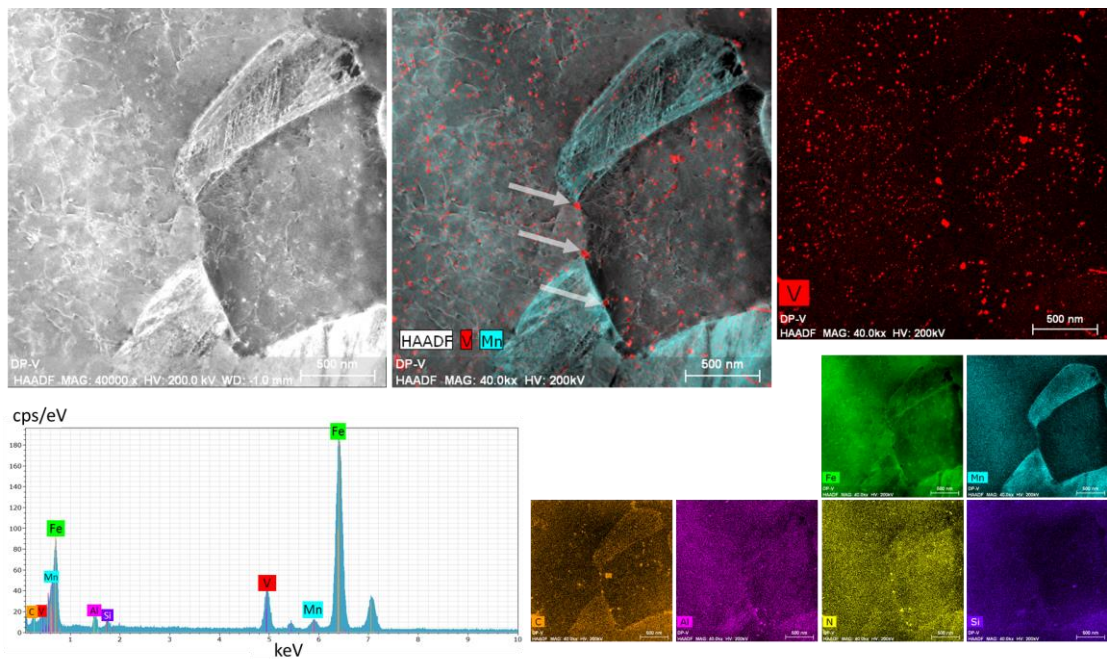
(b) DP-V DP steel

Figure 5-4 TEM Bright field (BF) images

Figure 5-5 provides a HAADF-STEM image, electron energy loss spectroscopy (EELS) map of elements and the EDS spectrum for both steels. In BF imaging, the objective aperture only allows undeflected electrons to contribute to the image, while for DF TEM images, those regions which can scatter more strongly will appear brighter [70]. As shown in Figure 5-5 (a), there are no precipitates or Mn segregation in DP-ref steels. Figure 5-5 (b) shows clear evidence of Mn segregation in DP-V steel, and there is more Mn in the DP-V steel. Many nano-scale V (C, N) particles (in red) precipitate both in ferrite and martensite phases. There are more V (C, N) particles inside the ferrite phase compared to martensite and the particles size in the ferrite phase is also bigger. Those relatively large particles can interact with dislocations and hinder dislocation movements during deformation. The white arrows in Figure 5-5 (b) indicates some larger V (C, N) particles at the α/α' interfaces.



(a) DP-ref steel



(b) DP-V steel

Figure 5-5 TEM observations, including HAADF images, EELS map of elements, and EDS spectrum

5.2 Macroscopic Stress-strain Behaviour

The macroscopic mechanical properties of DP-ref (V-free) and DP-V (V-added) steels along the RD and TD directions are analyzed based on macroscopic uniaxial DIC tensile tests.

The engineering stress is calculated based on the formula below:

$$\sigma_e = \frac{F}{A_0} \quad (5.1.1)$$

where F is the loading force exported from the tensile machine, and A_0 refers to the initial cross-section area of the tensile specimens.

The true strain is calculated from ARAMIS software by exporting ε_y (true strain along tensile direction) from the virtual gauge applied over the center of the specimens.

Figure 5-6 presents images exported from ARAMIS software. Figure 5-6(a) shows the micro-tensile specimen with mapping in project mode, and the red box refers to one square facet with the length of 13 pixels. Figure 5-6 (b) presents an example of strain mapping with a virtual gauge.

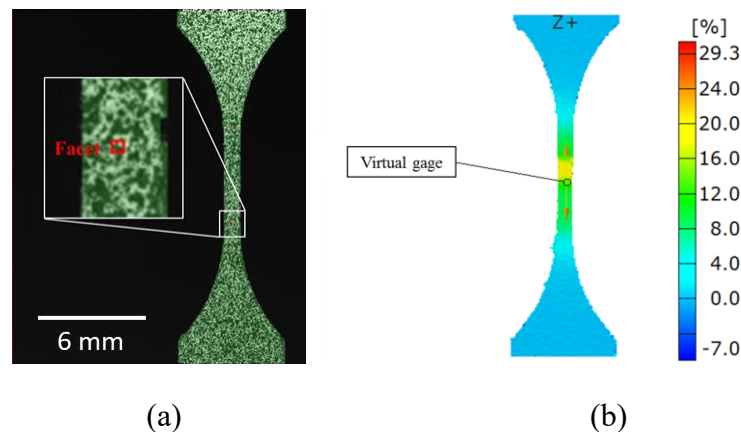


Figure 5-6 Images exported from ARAMIS software: (a) Specimen surface with mapping in project mode; (b) True strain map of DP-ref-RD-1

For all the data analysis in ARAMIS software, the facet size (square shape) is set to be 13 pixels and the step size is set to be 9 pixels. The detailed parameters setting in shown in Table 5-3. The initial virtual gauge length is selected to be around 4 mm in each case. The resolution is obtained by a manual calibration process in ARAMIS. The average resolution is about 106 pixels/ mm. Since the specimen width is 1mm, there are at least 9 facets over the width of the specimen when the surface pattern is good. In other words, there are enough facets to perform the calculation and the data is valid.

Table 5-3 Parameters setting in ARAMIS software for macroscopic tensile tests

Specimens	Initial virtual gauge length (mm)	Virtual gauge length before fracture (mm)	Resolution (pixel/mm)
DP-ref-RD-1	4.05	4.53	105
DP-ref-RD-2	4.03	4.35	112
DP-ref-TD-1	4.03	4.52	105
DP-ref-TD-2	3.96	4.40	102
DP-V-RD-1	3.97	4.38	109
DP-V-RD-2	4.01	4.64	103
DP-V-TD-1	4.04	4.61	110
DP-V-TD-2	3.97	4.45	104

The engineering strain during uniform deformation process can be calculated from the formula below: [71]

$$\varepsilon_e = e^{\varepsilon_T} - 1 \quad (5.1.2)$$

where ε_e and ε_T represent engineering strain and true strain along a tensile direction, respectively. Since the conversion is only valid when the gauge section is uniform, the calculation cannot be performed once necking occurs.

The true stress can be obtained through the formula: [71]

$$\sigma_T = \sigma_e (1 + \varepsilon_e) \quad (5.1.3)$$

where σ_e and σ_T represent engineering stress and true stress, respectively. Since the conversion is only valid when strain is uniform along the gauge length, the calculation cannot be performed after necking.

The initial cross-section area A_0 and the area after fracture A_F were measured.

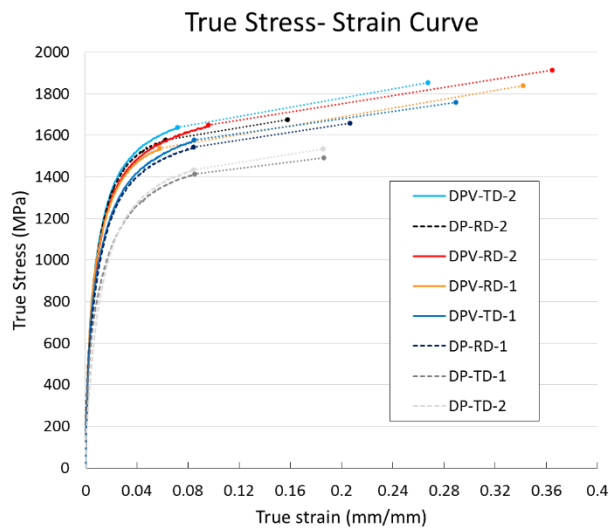
The area reduction RA can be obtained the formula:

$$RA = \frac{A_0 - A_F}{A_0} \times 100\% \quad (5.1.4)$$

The true strain when the specimen fractured in terms of reduction in area can be calculated from:

$$\varepsilon_F = \ln(A_0 / A_F) \quad (5.1.5)$$

For each material, two uniaxial tensile tests were performed. The true stress-strain curves of the DP-ref and DP-V steels along RD and TD directions are illustrated in Figure 5-7. The tensile curves are extrapolated by connecting the necking point to the final point (true stress and strain at fracture), assuming the post-uniform stress-strain relationship is linear.



(a)

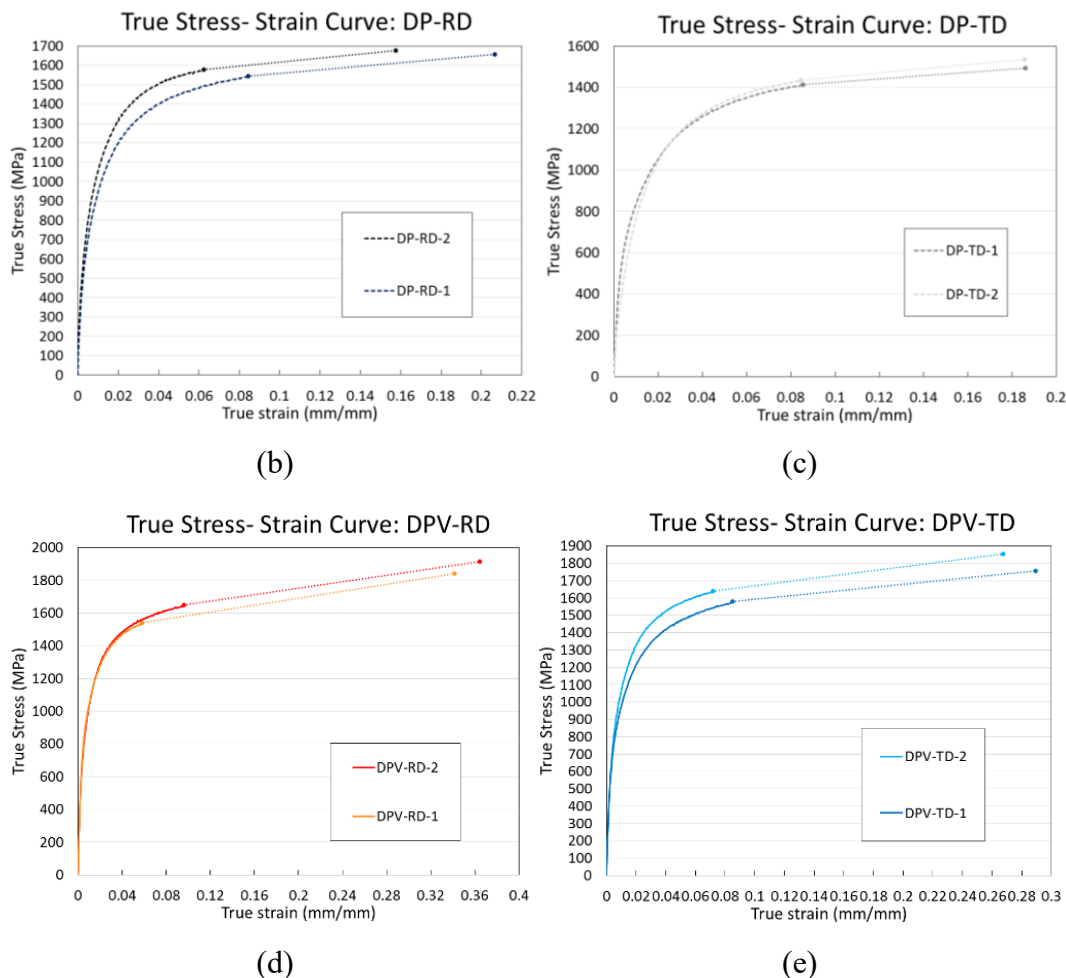


Figure 5-7 True stress v.s. strain curves of DP-ref and DP-V steels: (a) All of the materials; (b) DP-ref-RD; (c) DP-ref-TD; (d) DP-V-RD; (e) DP-V-TD

Both steels show the typical characteristics of α/α' DP steels: low yield strength, lack of distinct yield point, continuous yielding, high initial strain-hardening rate and low YS/UTS ratio. There exist some differences between the two directions and two groups of data except for DP-ref steels along TD direction. It suggests that there exists a certain level of anisotropy and slight heterogeneity of the steel sheets in the material. This correlates well to the observation that the two phases are elongated along RD direction, as can be seen in Figure 5-1.

Figure 5-8 plots the evolution of the work hardening response of DP-ref and DP-V

steels along RD and TD directions. All the curves are almost overlapped with each other. It is not possible to distinguish any significant difference between those groups.

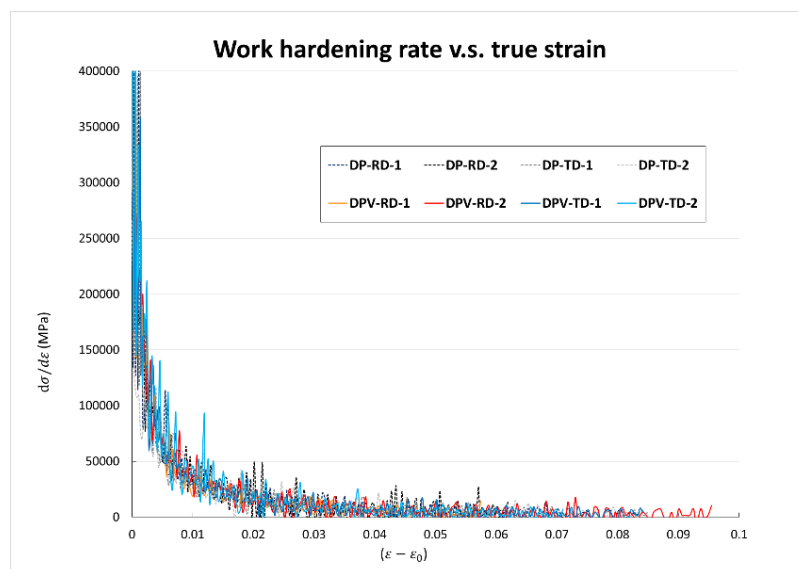


Figure 5-8 Plotting of the evolution of the work hardening against the true strain

Table 5-4 summarizes the tensile tests data, including 0.2% offset yield strength ($\sigma_{0.2}$), engineering ultimate tensile stress (σ_u), engineering uniform elongation (ϵ_u), reduction in area (RA%), and the true strain to fracture (ϵ_F).

Table 5-4 Mechanical properties of the steels

Specimens	Eng. $\sigma_{0.2}$ (MPa)	Eng. σ_u (MPa)	$\sigma_{0.2}/\sigma_u$	Eng. ϵ_u (%)	RA% (%)	True strain ϵ_F
DP-ref-RD	755±86	1451±45	0.57	7.6±1.7	16.6±2.9	0.182±0.035
DP-ref-TD	518±145	1309±15	0.48	8.9±0.1	16.9±0.04	0.186±0.0005
DP-V-RD	839±27	1475±33	0.57	8.0±2.8	29.8±1.2	0.353±0.016
DP-V-TD	813±52	1488±53	0.55	8.2±1.1	24.3±1.2	0.278±0.015

Both DP steels have a high ultimate tensile strength (over 1400 MPa) except for DP-ref-TD steels, which shows relatively lower strength close to 1300 MPa. The overall yield strength of DP-V steels is higher than for the DP-ref steels. According to the work done by Scott [66], when using the same thermomechanical process for both grades, the DP steel with vanadium addition shows both higher UTS and better ductility in comparison with the vanadium free steels. In this project, with a slight modification of the thermomechanical process, both DP-V and of DP-ref steels have similar martensite content and similar UTS. This makes it possible to explore the effect of vanadium addition on ductility through microstructural refinement. Despite the similar uniform elongation is for both steels, the total strain at fracture for DP-V steels along both RD and TD directions are much higher than for the DP-ref steels; this represents an improvement in post-uniform ductility due to the vanadium addition. The large reduction in cross-section area of DP-V steels caused by significantly localized necking also reflects the profound effect of vanadium addition on post-uniform elongation. In summary, the addition of vanadium refines the microstructure of α/α' DP steel and improves the true ductility at similar strength levels.

The tensile strength combined with the estimated elongation of both steels are plotted over the global formability diagram in Figure 5-9. DP1300 is located in the right upper corner of the diagram, which corresponds to the third generation AHSS. We can conclude that DP-V steel presents high strength and ductility, which is very promising for the enhancement of crashworthiness for the application in automotive industry.

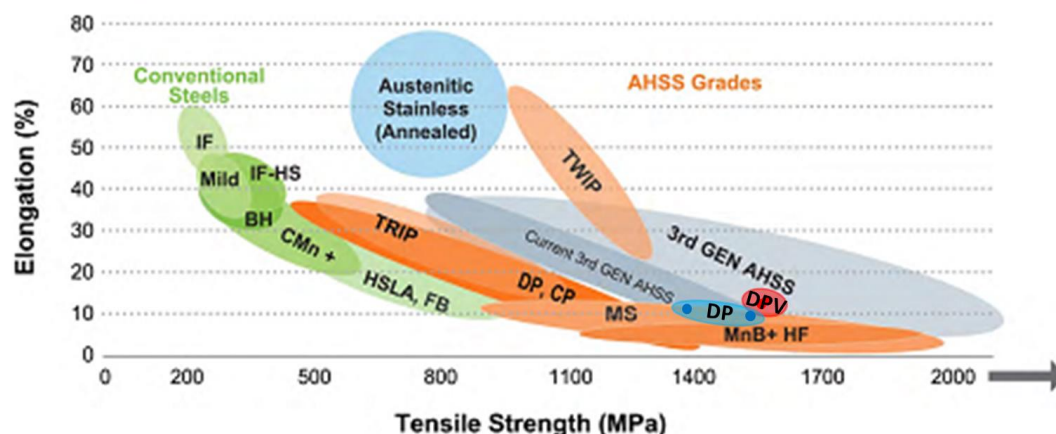


Figure 5-9 Investigated DP steels mechanical properties overlapping with global formability diagram [3] (DP: V-free steel; DPV: V-added steel)

5.3 Nano-indentation Study

Nano-indentation tests were conducted to investigate the influence of vanadium addition on the strength of ferrite and martensite grains. The nano-indentation data of both steels are provided in Figure 5-10. As expected, the hardness of ferrite is clearly separated from martensite in both steels. However, the separation between the hardness of two phases is lower in the DP-V steel than that in the DP-ref steel. These results are in a good agreement with the hypothesis stated by Scott et al. in [66], who proposed that for steels with similar martensite content, the ferrite of the DP-V steel must always be stronger than that of the DP-ref steel, and thus the martensite must be softer. This is valid if the carbon precipitated in the form of VC and V(C, N) was considered to be “lost” for martensite strengthening purposes (it should be noted that it was verified that the cementite dissolution behavior was similar for both alloys) [66]. Since the hardness of martensite is mainly controlled by the carbon content, and when a large amount of carbon is consumed by vanadium all over the microstructure, the carbon content of martensite and therefore its hardness is decreased.

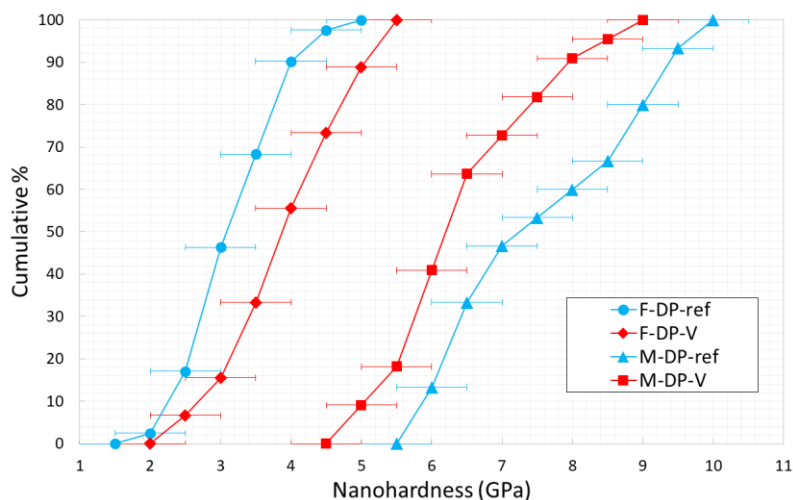


Figure 5-10 Cumulative distribution of ferrite and martensite island hardness of both steels from nano-indentation measurements.

The detailed analysis of nano-hardness data is discussed in the following section using the approach already developed by Scott et al [72].

5.3.1 Nano-hardness of Ferrite

The average ferrite nano-hardness was 3.8 GPa for DP-ref steel, which is in accordance with published nano-hardness data for similar steels when using the similar experiment conditions [73]. The DP-V steel has an average nano-hardness of 4.1 GPa. The increase of strength in ferrite can be explained by grain refinement and precipitation strengthening from V(C, N) precipitation.

The difference in the average yield stress of the ferrite grains (ΔYS_f) between the two steels can be estimated. Zhang et al [74] compared the nano-hardness (H_n) and Vickers hardness values (H_v) for a series of Fe-C martensitic steels. When ignoring grain size effects and extrapolating their data to zero carbon content (for ferrite), it can be found that the ratio $(H_n / H_v)_\alpha$ should be ~ 1.33 when both of the hardness values

are expressed with the unit GPa. Suppose this ratio is the same in both steels, and thus the difference in the average Vickers hardness ΔH_v is $(4.1-3.8)/1.33 \sim 0.23$ GPa (~ 23 kgf / mm^2). From the empirical correlation between ΔH_v and YS provided by Pavlina and Van Tyne in [75], we can obtain the following equation:

$$\Delta YS = 2.876 \Delta H_v \quad (5.1.6)$$

where ΔYS has units of MPa and ΔH_v has units of kgf / mm^2 . Therefore, the average yield stress of ferrite in the DP-V steel is ~ 66 MPa higher than that of the DP-ref steel. The increment in the ferrite can be ascribed to the reduction of grain size and vanadium precipitation.

The contribution of grain refinement in strengthening can be calculated from the Hall-Petch relationship:

$$\sigma_y = \sigma_0 + k_y / \sqrt{d} \quad (5.1.7)$$

where σ_y is the yield stress, σ_0 is the friction stress against the movement of dislocations in the grains and k_y is a constant. Therefore, the relationship between $\Delta \sigma_y$ and Δd is:

$$\Delta \sigma_y = k_y / \sqrt{\Delta d} \quad (5.1.8)$$

Calcagnotto et al. [76] investigated a range of DP steels with 0.17 wt.%C. with varied grain size. They found that the yield strength obeyed the Hall-Petch relation and k_y is $4.0 MPa / mm^{-1/2}$ [76]. The calculated increment of ferrite yield stress is 71-87 MPa (Table 5-5). Therefore, the Hall-Petch strength fully accounts for the experimental value for $\Delta \sigma_y$ of 66 MPa. It should be realized that precipitation strengthening is also involved here. However, it is hard to estimate the strength

increase due to the precipitation strengthening because the volume fraction and the mean particle diameter of V(C, N) are unknown.

Table 5-5 Yield stress increment derived from Hall-Petch relationship

	// RD	// ND
S_F in DP-ref	4.8 μm	2.9 μm
S_F in DP-V	1.6 μm	0.8 μm
ΔS_F	3.2 μm	2.1 μm
$\Delta\sigma_y$	71 MPa	87 MPa

5.3.2 Nano-hardness of Martensite

The ratio $(H_n / H_v)_{\alpha'}$ is ~ 1.2 for martensite [74]. The average martensite nano-hardness was 7.7 GPa in the DP-ref steel, and 6.6 GPa in the DP-V steel, respectively. Similar to the analysis just used for ferrite, the difference in the average Vickers hardness ΔH_v is $(7.7-6.6)/1.2 \sim 0.92$ GPa ($\sim 93.5 \text{ kgf} / \text{mm}^2$) which corresponds to a difference in the martensite YS of ~ 349 MPa.

Pavlina and Van Tyne also proposed an empirical correlation between ΔH_v and UTS in [75]:

$$\Delta UTS = 3.734 \Delta H_v \quad (5.1.9)$$

where ΔUTS has units of MPa and ΔH_v has units of kgf / mm^2 . Therefore, ~ 349 MPa difference is expected for the UTS between the two alloys.

Suppose the C wt.% of ferrite in both steels is 0.02 wt.%, so the corresponding C wt.% of martensite of DP-ref and DP-V steel is 0.44 wt.% and 0.40 wt.%, respectively. Buessler et al. [77] proposed an analytical expression which can calculate the Vickers hardness of individual martensite island from the carbon content in martensite:

$$HV = \alpha - 1 / (\beta + \gamma[\%C])^\delta \quad (5.1.10)$$

where $\alpha = 950.44$, $\beta = 0.9688$, $\gamma = 0.1274$, $\delta = 208.676$, the carbon content is expressed in wt.% and the Vickers hardness HV is expressed in kgf / mm^2 . After converting the unit from kgf / mm^2 to GPa and converting the Vickers hardness to nano-hardness, H_n is derived. The calculated martensite strength of DP-ref and DP-V steels are 8.5 GPa and 8.2 GPa, respectively (Table 5-6). The influence of VC formation on the reduction of martensite hardness is analyzed below. Now assume that all the vanadium exists in the form of VC, and the precipitated VC makes no contribution to the martensite strength. The extreme case is considered here, where vanadium absorbs the maximum carbon content and that part of carbon caused by 0.14 wt.% V addition should be deducted from the wt.% C in martensite. Therefore, the calculated martensite hardness is reduced by 0.58 GPa to 7.7 GPa. The corresponding difference of martensite nano-hardness between the two materials is increased from 0.29 GPa to 0.87 GPa when considering the carbon composition reduction in martensite. The calculated data (0.87 GPa) explains the reduction of martensite strength in DP-V steels indicated by nano-indentation study (1.1 GPa). We can propose here that carbon content in martensite plays a very important role on martensite strength, and the vanadium addition reduces the carbon content in martensite and leads to the softening of martensite in DP-V steel.

Table 5-6 Ferrite (α) and martensite (α') strengths obtained from nano-indentation measurements compared with the calculated hardness

Alloy	C (wt.%)	V_M	Phase	Number of retained Indents	Average Nano Hardness (GPa)	Assumed average carbon (wt.%)	Calculated Hardness (GPa)
DP-ref	0.21	0.49	α	41	3.8 ± 0.5	0.02	-
			α'	15	7.7 ± 0.5	0.44	8.5
DP-V	0.23	0.5	α	45	4.1 ± 0.5	0.02	-
			α' -(a)	22	6.6 ± 0.5	0.40	8.2
			α' -(b)	-	-	0.334	7.7

5.4 Microstructure Evolution during In-situ Tensile Test

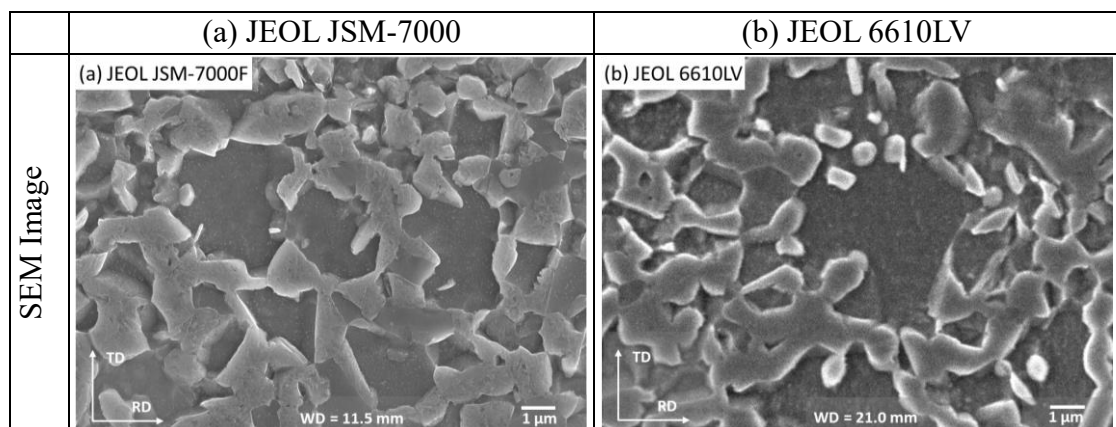
The previous section illustrated that the addition of Vanadium is an effective strategy to improve the post-uniform ductility while maintaining strength. In this section, the local deformation behavior between ferrite and martensite will be quantitatively investigated using the μ DIC technique. The full history of the strain field from the undeformed state until fracture can be obtained through μ DIC analysis based on SEM images taken after each successive loading step. The macroscopic stress-strain relationship can then be correlated with the local deformation behavior of the two phases.

5.4.1 SEM Selection

The image quality is of crucial importance for DIC analysis. To determine the appropriate SEM for the μ DIC experiment, both JEOL JSM-7000F and JEOL 6610LV were used for image recording. The JEOL JSM-7000F equipped with a Schottky field emission gun offers high resolution but is limited because of the small specimen chamber. The JEOL 6610LV equipped with a thermionic tungsten filament has a larger chamber, but offers lower resolution compared to the JEOL JSM-7000F. The large chamber in the JEOL 6610LV makes it possible to employ an automated tensile

stage for the in-situ tensile tests.

The micrographs of DP-V were taken from these two SEMs with a similar resolution (6 nm/pixel). A series of micrographs with small deformations were imported into ARAMIS software and calculations were performed by setting the same parameters combined with one starting point. The facet size and step size were set to 27 pixels and 21 pixels, respectively. Due to the principle of thermionic SEM and the large working distance (21.0 mm) induced by the automatic tensile stage, the image obtained from JEOL 6610LV shows poorer quality and digital image correlation maps are worse in comparison with the image taken from JEOL JSM-7000. To obtain the strain value inside of the small ferrite grains, the desired facet size step size needs to be smaller. In addition, the deformation applied to the tensile specimens in an in-situ experiment would also be larger compared with the test case here. When performing calculations with smaller facet size and step size combined with a series of images with larger deformation, it would be more difficult to obtain good results for ARAMIS. Therefore, the SEM JEOL JSM-7000 combined with the manual tensile stage was selected for this project.



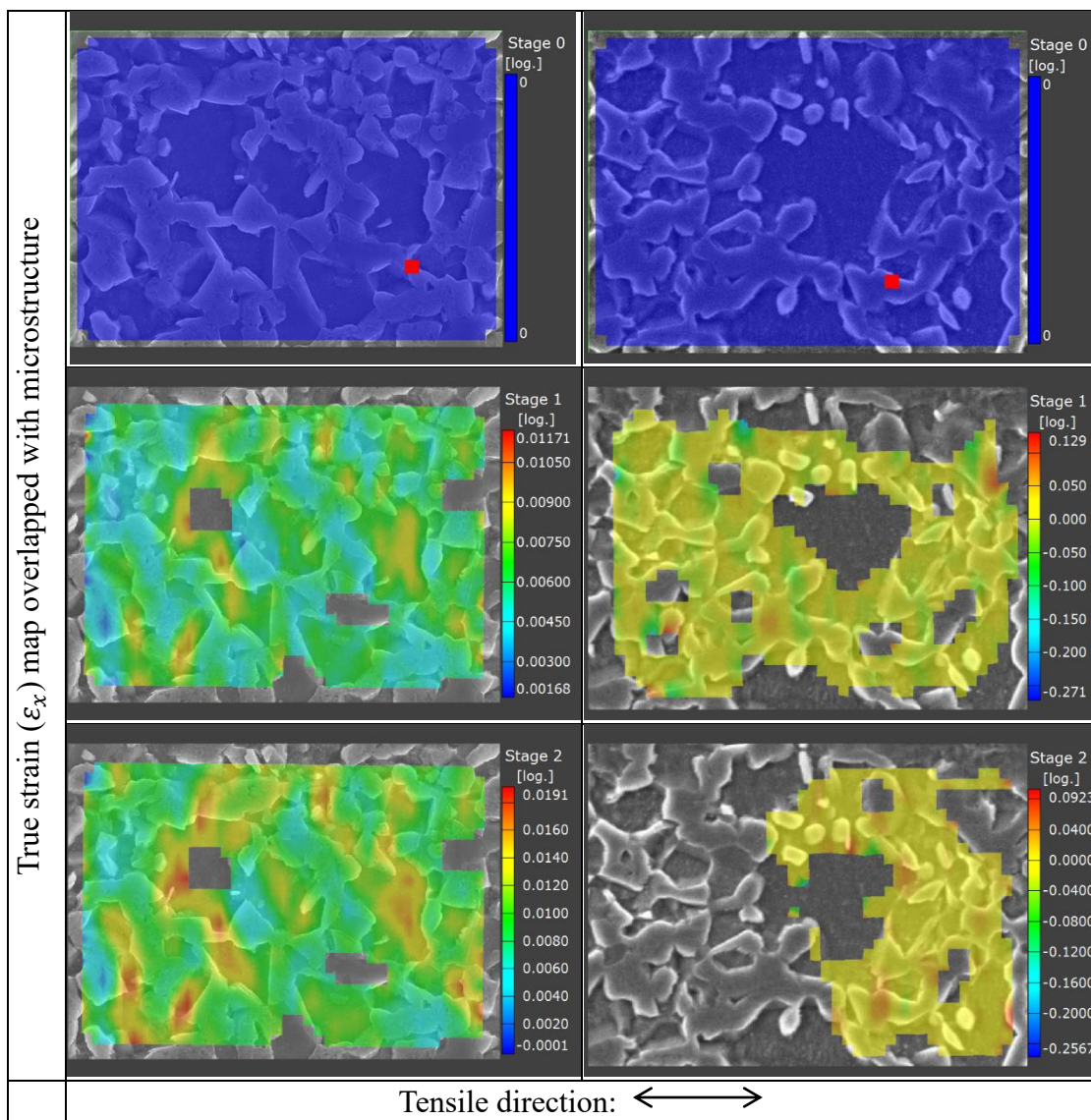


Figure 5-11 SEM images under similar resolution and strain maps of DP-V steels obtained from DIC analysis (a) Micrographs taken from JEOL JSM-7000, (b) Micrographs taken from JEOL 6610LV. (facet size x step size = 27x21 pixels)

5.4.2 Strain Analysis

As mentioned in section 4.3.2, all the in-situ tensile tests were performed within a JEOL JSM-7000F SEM combined with micro-tensile hourglass-shaped test specimens. There was no extensometer applied and the distance change between indents was utilized as a reference to calculate the macroscopic strain. The relative

locations of micro-hardness indents (1-13) and selected locations (A-H) for taking images are shown in Figure 5-12. Those micro-indents were originally 83 μm apart.

The red dash line in Figure 5-12(b) and (d) represents the main crack leading to fracture of micro-tensile specimens. There were eight locations selected for each in-situ tensile test. In other words, eight groups of SEM images were taken for each case. Those locations which are the closest to the main crack and enjoy good image quality are input into ARAMIS to perform strain calculation.

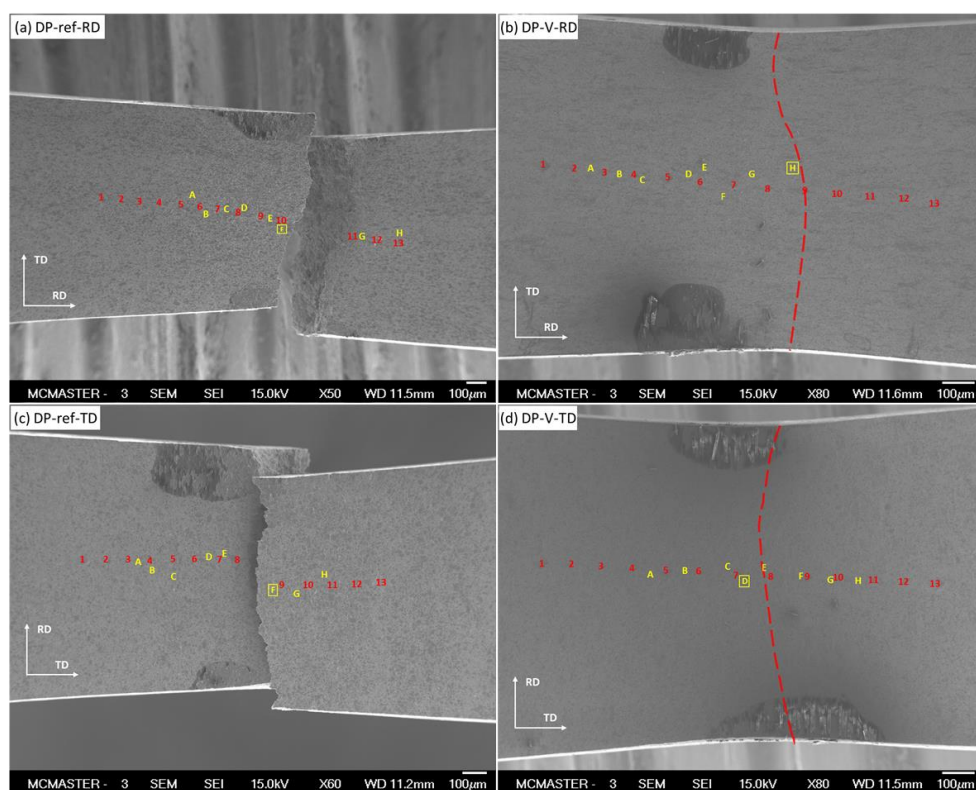


Figure 5-12 SEM images of heavily deformed or fractured micro-tensile specimens at low magnifications showing relative locations of micro-indents and image locations.

(a) DP-ref along RD; (b) DP-V along RD; (c) DP-ref along TD; (d) DP-V along TD.

Capital letters A-B represents locations where images were taken; Arabic numbers 1-

13 represents locations of micro-indents. The selected regions to perform DIC are

highlighted by boxes with a yellow outline

In this section, the local deformation behavior between the two phases is quantitatively analyzed. Strain obtained from micro-indent distance and strain calculated from DIC method will be discussed.

5.4.2.1 Micro-indent Strain Measurements

The local strain compared with total strain calculated from the micro-indent displacements are plotted in Figure 5-13. For all the cases, the local strains varied along the gauge length.

The strain is enhanced in those regions closed to the fracture surface (red dash line). For those regions located outside of the necking region, the strain is much smaller (blue dash line). The total strain between indents No. 1- No. 13 is higher in DP-V steels in comparison with DP-ref steels which is consistent with the macroscopic strain behavior.

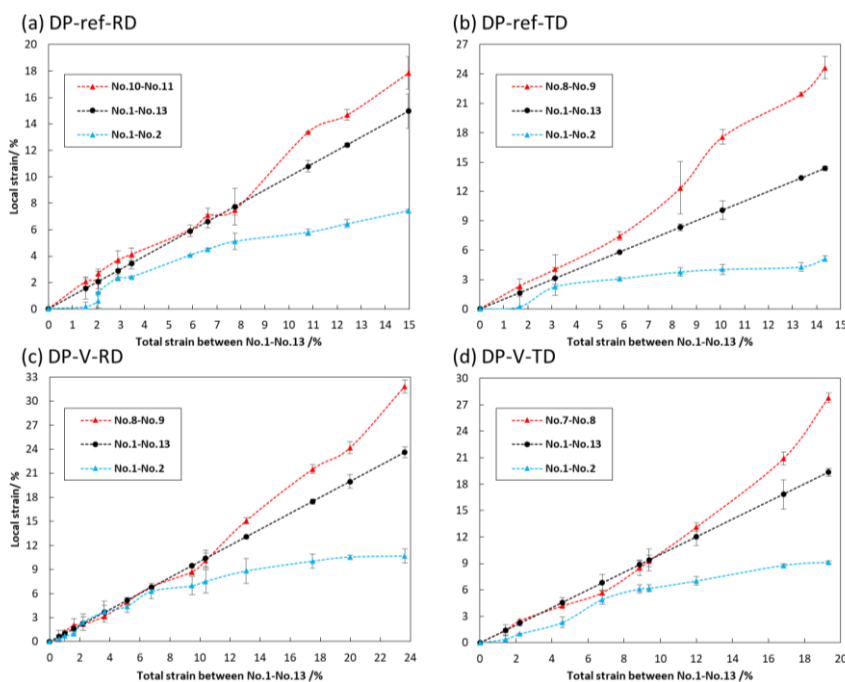


Figure 5-13 Engineering strain measurements of indents. Red dash line: strain measurements of two indents where the main crack went through; Blue dash line: strain measurements of two indents which are away from the fractured part.

5.4.2.2 Microscopic Strain Measurements

In order to track the strain distribution under microscopic level quantitatively, DIC analysis is applied. A series of images for all the cases were imported into the ARAMIS software to perform strain calculations. All the parameters used in DIC along with the SEM images features are listed in Table 5-7.

The selection of SEM images and data processing in ARAMIS is of crucial importance in this project. Different magnifications were selected for each case to guarantee there are enough characteristic features and an appropriate number of grains to be analyzed in the local field. The characteristic features present on the SEM images depend on the etching conditions and SEM parameters setting of the images, including working distance, magnifications, accelerating voltage, and probe current, etc. With increasing of strain, parts of the image cannot be analyzed by ARAMIS and lead to a weak correlation of the corresponding facets due to the appearance of the new features. Therefore, the strain increment between steps needs to be relatively small to guarantee the image correlation process is successful.

The facet size exerts significant influence on data processing [74-77]. For one thing, the facet size should be large enough to reveal the characteristic feature of the local field. For another, the facet size should be small enough to guarantee the deformation of the facet is uniform. Besides, in terms of efficiency, smaller facet size leads to more facets and lowers the efficiency. Therefore, facet size selection should be optimized to achieve the best trade-off between spatial and strain resolution. Moreover, the step size can be converted into an actual size by calibration from the scale bar. When the computation size is set to be three, the gauge length is two times of the step size [56]. In order to represent the local strain at the grain level, the gauge length should be smaller than the average grain size. [61]. The step size is set to be similar in four experiments (0.22 μm and 0.23 μm) to obtain the same gauge length and then the data

set can be comparable.

The assessment of the accuracy of this measurement is also very important. The allowable accuracy was set to 0.04 pixels for all cases and valid for all the analysis. In order to ensure the accuracy, the correlation algorithm embedded in ARAMIS locates the same four corner points of a facet in two successive images and analyzes their corresponding grey-level distribution. Then the algorithm optimizes the accuracy by repositioning the corner points until no better positions can be located within the set accuracy [61]. The maximum error Δ in the strain calculation can be calculated as:

$$\Delta = \frac{0.04}{step_size} \quad (5.1.11)$$

Table 5-7 Parameters of microscopic strain calculation in ARAMIS

Specimens	DP-ref-RD	DP-ref-TD	DP-V-RD	DP-V-TD	
Magnifications	x3500	x4000	x8000	x7000	
Represented Area (μm^2)	34x27	30x24	15x12	17x14	
Facet Size x Step size (pixels)	23x17	25x19	53x39	45x33	
Facet Size x Step size ($\mu\text{m} \times \mu\text{m}$)	0.31x0.23	0.29x0.22	0.31x0.23	0.30x0.22	
Resolution (pixels/ μm)	75	85	171	149	
Maximum error	0.0024	0.0021	0.0010	0.0012	
Counted No.	F	267	478	99	156
	M	568	114	102	93

The strain measurements of ϵ_x in DIC can be obtained from virtual gauge line and average strain of the field. Figure 5-14 presents an example of virtual gauge lines.

Three lines were selected and average values are obtained.

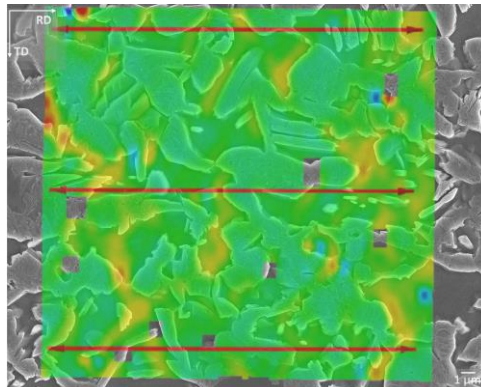


Figure 5-14 Schematic drawing showing selected lines

As mentioned earlier, when the strain increment is very big or new features develop between stages (cracks or voids), ARAMIS cannot track locations and perform the necessary calculations and thus the strain maps include blank regions. In the case of large deformation, an interpolation function can be applied to fill the blank regions in the strain maps after removing the damage accumulation regions. Figure 5-15 illustrates an example of strain maps before and after interpolation. It can be seen from the figure that the left lower corner was filled after interpolation. The interpolation function can automatically fill those blank regions by replacing blank region with the certain value obtained by averaging the surrounding region.

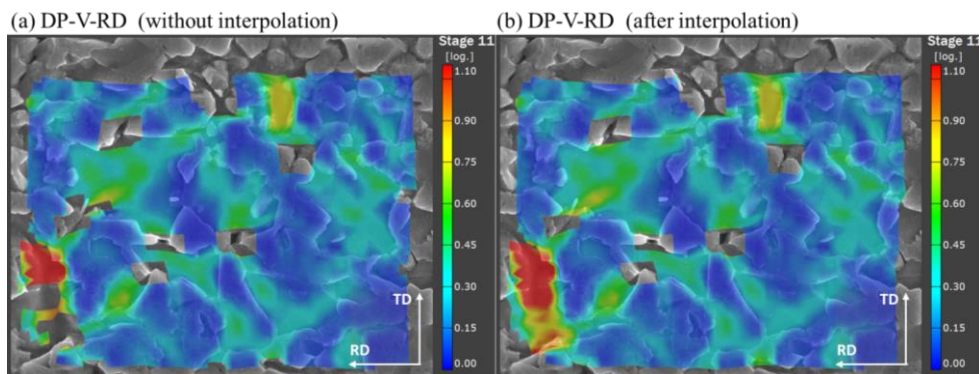


Figure 5-15 Strain maps before and after interpolation

The DIC strain measurements are compared with micro-indent strain measurements in Figure 5-16. All three measurements have varied gauge length. DIC virtual gauge line strain measurements have a gauge length that corresponds with the image width (15-34 μm). DIC area measurements have a gauge length of 0.44-0.46 μm (two times of the step size). The bars in the line of DIC- area denote the full range of experimental scatter. The micro-indent strain measurements have a gauge length of 83 μm . Despite the differences, these three measurements show a similar trend of strain evolution, suggesting a good agreement between varied strain measurement methods. Since the strain measurements over the area incorporate abundant data set, the corresponding error bars are largest. As expected, the DP-V steels along both directions enjoy a higher strain compared to DP-ref steels.

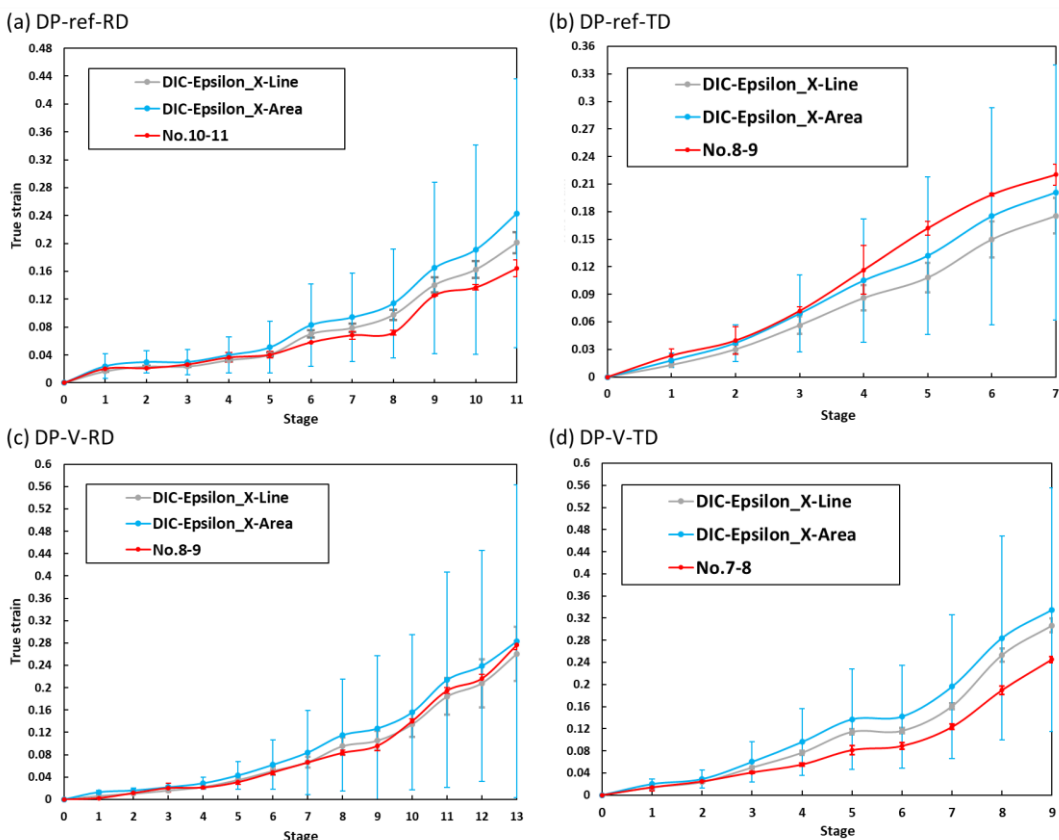


Figure 5-16 Strain measurements comparison

Figure 5-17 schematically illustrate the influence of image location selection on the measured DIC strain value. The plotted local strain between the two micro-indentations is arbitrary. The DIC strain measurements can be either higher or lower than the micro-indentations strain measurements, which shows the inhomogeneity of the strain field.

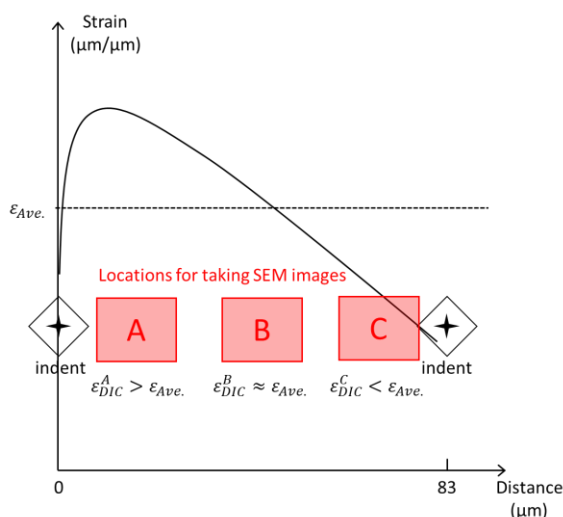
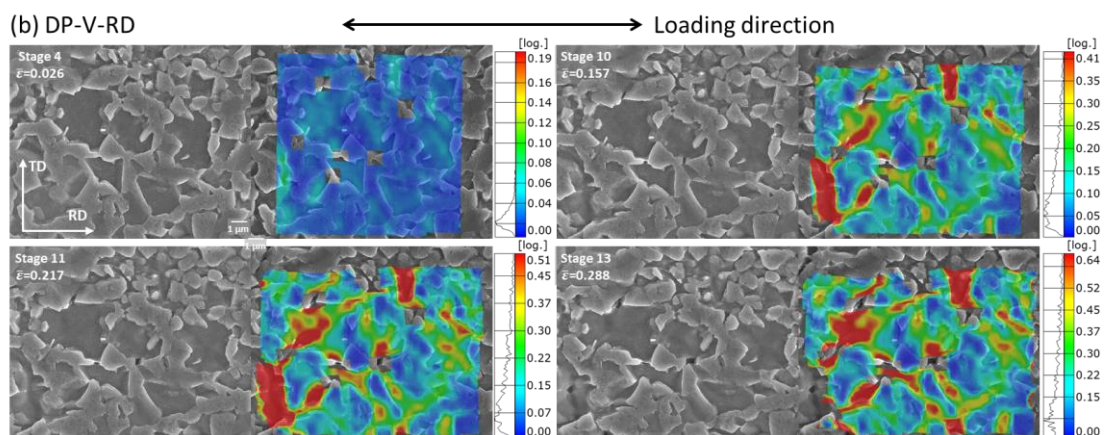
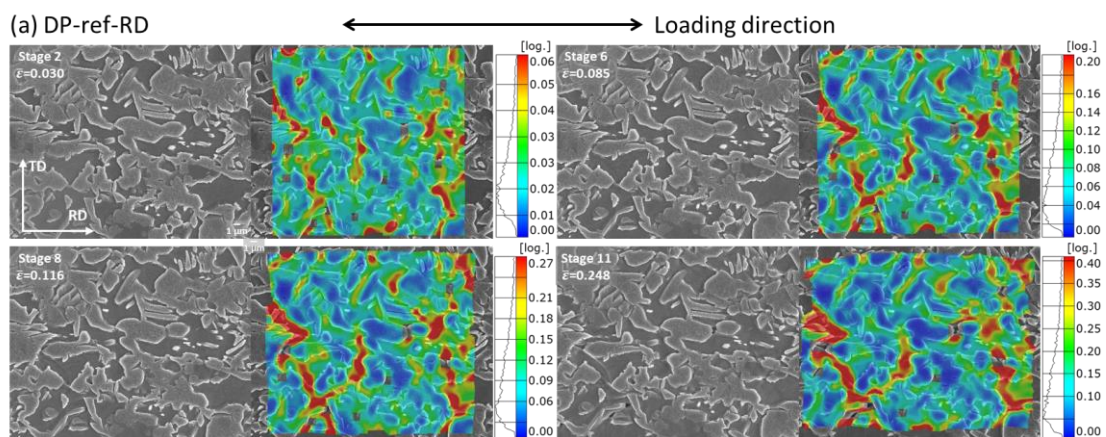


Figure 5-17 Schematic diagram showing the relationships between the micro-indentations strain measurements and DIC average strain

Figure 5-18 summarizes the development of equivalent strain distribution over the microstructure during in-situ tensile testing until the stage before fracture for all the materials. For most cases, after removing the damaged area, the interpolation function filled those blank regions. However, when the strain increment between stages is too high, even the interpolation function cannot fill the holes in the strain maps. The final stage (stage 13) of DP-V steel in Figure 5-18 (b) shows an example. The strain of the left lower corner is too big to have strain maps, which may influence the strain analysis in the following part.

It is clearly shown that in all cases, noticeable strain heterogeneity appeared in the early stages of the deformation (less than 0.03), which is far less than the uniform

elongation ($\epsilon_u = 0.08$). As the deformation proceeds, the strain distribution is more heterogeneous. The strain heterogeneity is also found within individual ferrite grains in Figure 5-18(b) (c) (d). Most of the higher strained area (hot spots) corresponds to α/α' interface and α matrix, while the major part of the less strained area is located on martensite islands. Hot spots are preferentially generated at those locations where ferrite is under high constraint by the surrounding martensite islands. The local strain in the hot spots can reach much higher values compared to the global strain in that field. It should be noted that those sites where hot spots are located can be assumed as the likely sites for damage initiation. As the deformation proceeds, microscopic damage develops and exerts a significant effect on the surrounding region, which leads to the formation of a hot spot pattern in the strain maps.



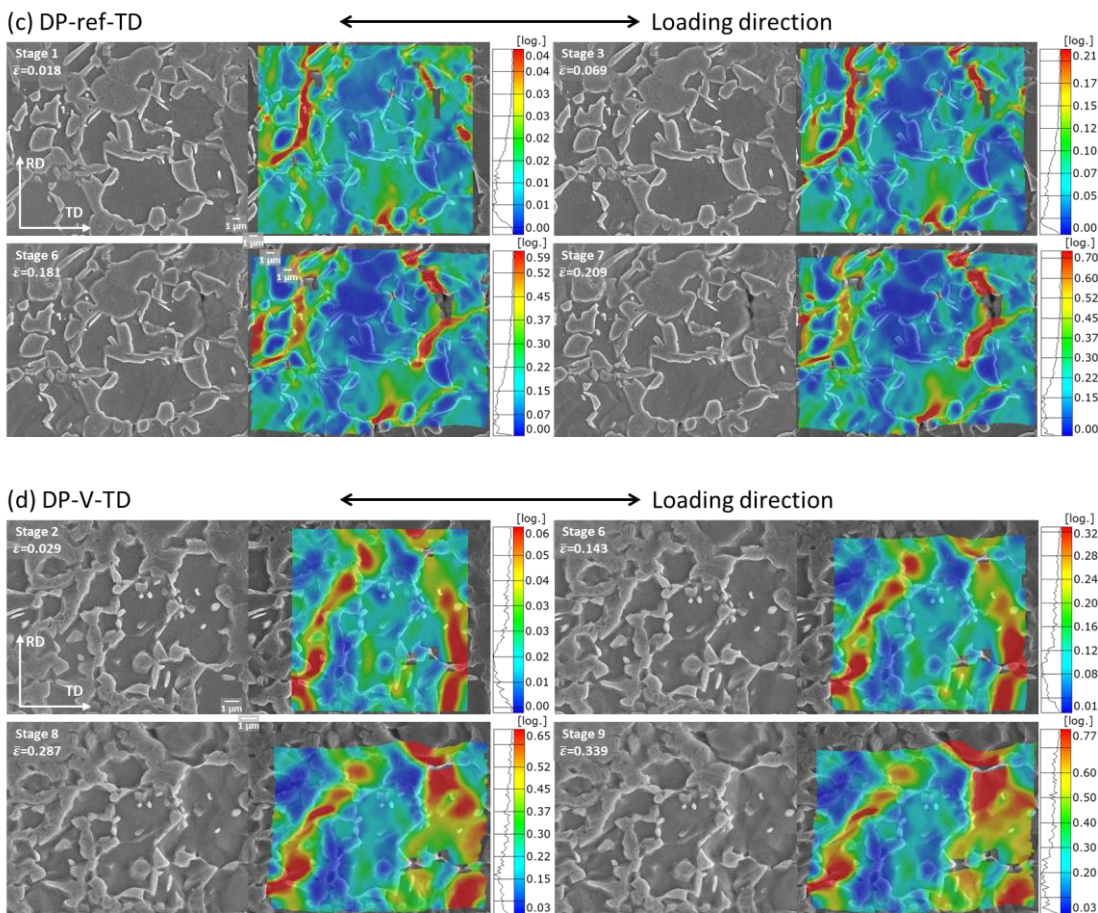


Figure 5-18 Typical examples of the deformation of the steels: SEM images (left) and equivalent strain maps overlapping with microstructures.

The development of the strain distribution in the two materials is quite different. Figure 5-19 compares the maximum equivalent strain over the minimum equivalent strain for each case. Both DP-V steel samples tested along the RD direction and the DP-V steels samples tested along TD direction present lower values, suggesting that the variations of local strain in DP-V steels are lower than those in DP-ref steels. In other words, the strain distribution is more uniform in DP-V steels.

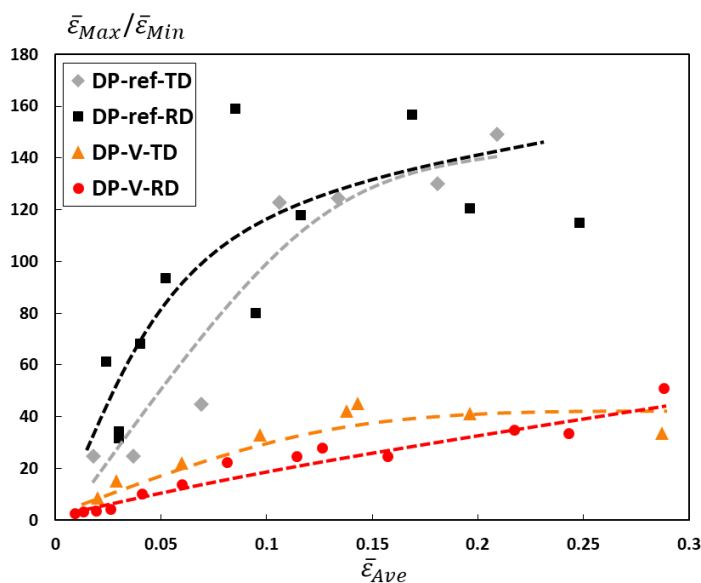


Figure 5-19 DIC Effective strain $\bar{\epsilon}$ measurements comparison

Figure 5-20 compares the equivalent strain distribution for steels along the RD direction. SEM images in the undeformed state are used as the reference state for strain analysis. Those stages with similar average global strain were selected for comparison. Despite different magnifications, the number of grains in the selected field is roughly the same. By setting the legend to show the same extreme value, it is clearly seen that the strain distribution in DP-ref steels is much more heterogeneous. There is a higher contrast between the regions of high strain (ferrite) and the regions of low strain (martensite) in DP-ref steels.

To clarify the remarkable difference in strain partitioning between DP-ref and DP-V steels, cumulative strain distribution in the ferrite phases and martensite islands are separated and then plotted in Figure 5-21. Figure 5-21 (1) set the bounds of the x-axis to be the same in order to compare the data. Figure 5-21 (2) adjusts the maximum bounds of the x-axis to an appropriate value to show the cumulative curve more clearly. As expected, the distribution of ferrite strain is clearly separated from martensite in both steels. Besides, the cumulative distribution of the strain in ferrite in

the DP-ref steel reaches a maximum value by spreading over a large strain region, while the cumulative distribution of the strain in the martensite islands only occupied a smaller region before reaching the maximum value. In other words, the DP-ref ferrite contains a number of regions with strain well in excess of the average while the ferrite strains in the DP-V steels are more tightly bounded. With the increase of applied tensile strain, this strain partitioning becomes more pronounced. In addition, the strain distribution in the ferrite phase is spread in a larger region with the increase of strain, while the distribution in the martensite islands remains in a relatively small range. Contrarily, the difference of distribution of strain between two phases in DP-V steel is smaller. Moreover, both distributions present a shift to larger strain value, suggesting that the deformation is more homogeneous in DP-V steels.

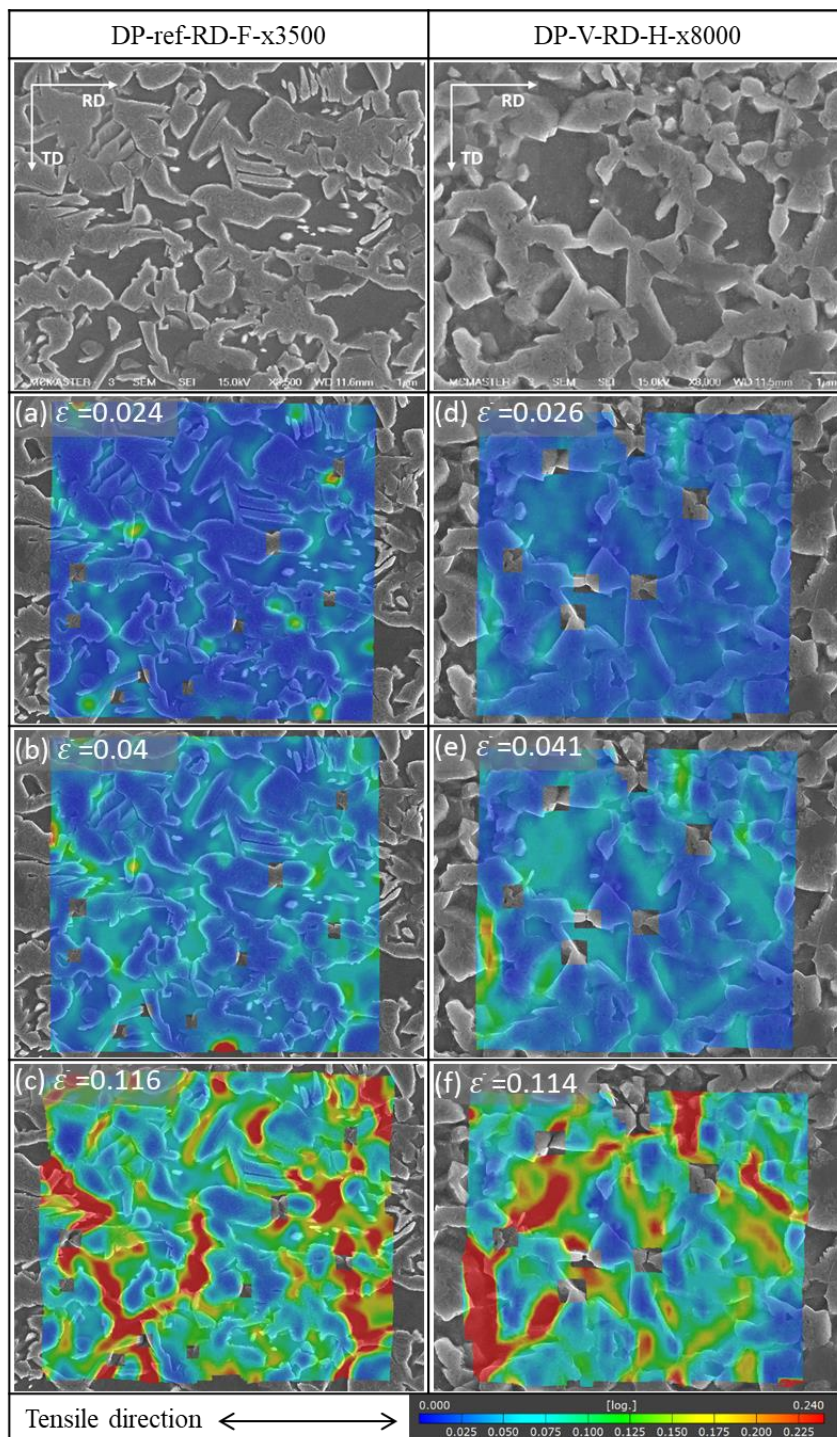
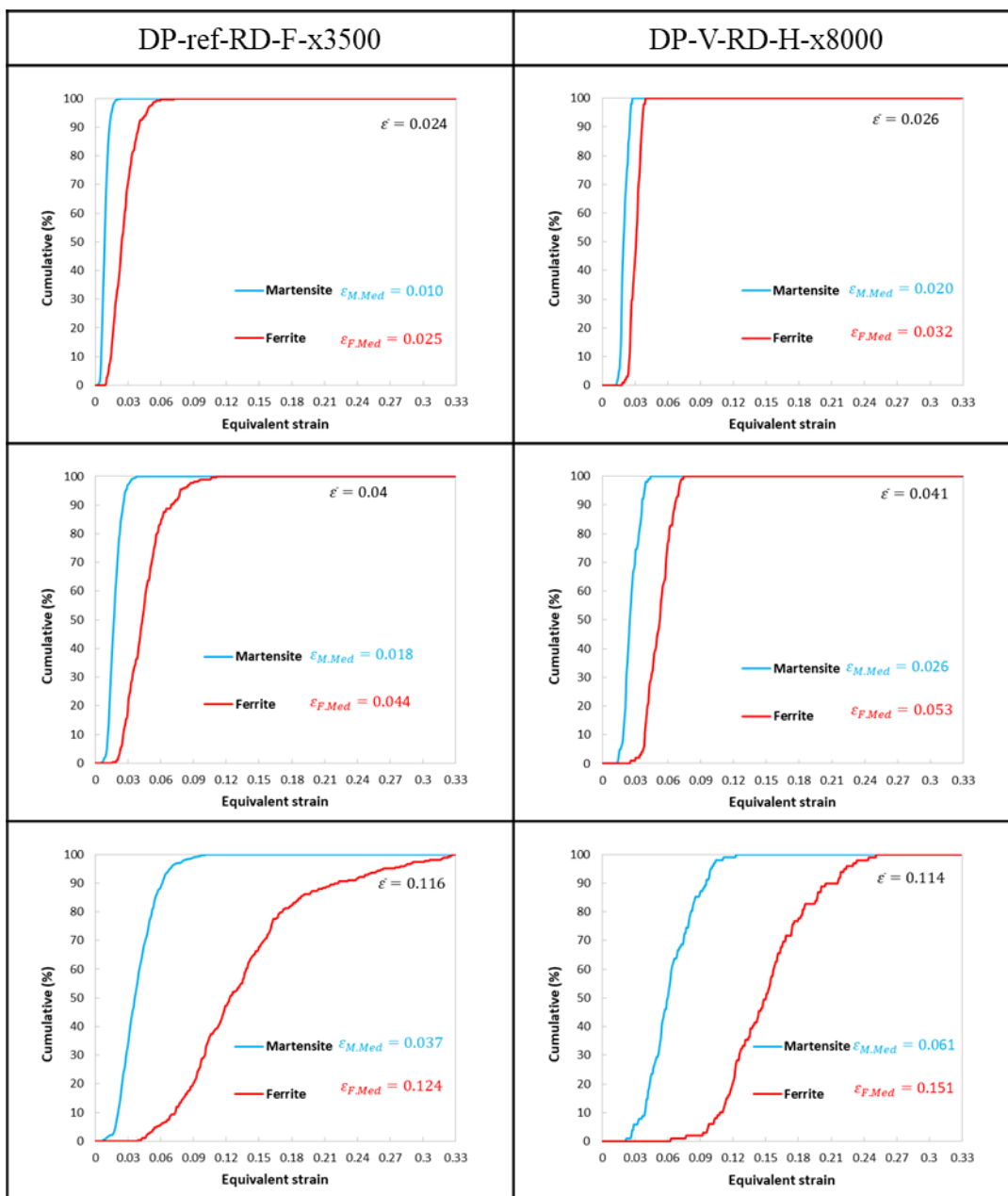


Figure 5-20 Equivalent strain maps comparison between steels along RD directions.

The legend is set to be same for all the stages.

(1)



(2)

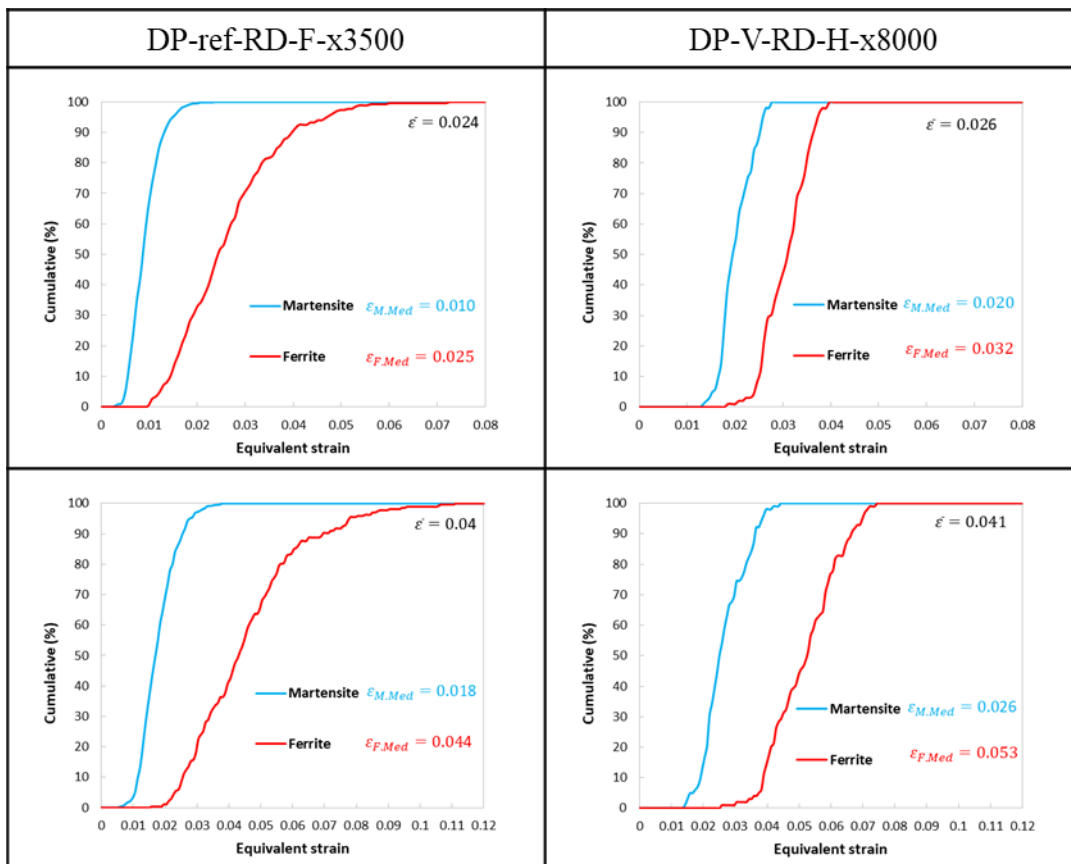


Figure 5-21 Cumulative equivalent strain distribution between ferrite and martensite for DP-ref and DP-V steels along RD directions.

Figure 5-22 present the strain distribution between ferrite and martensite in steels along TD directions. They show a similar trend of the two distributions to those along RD directions.

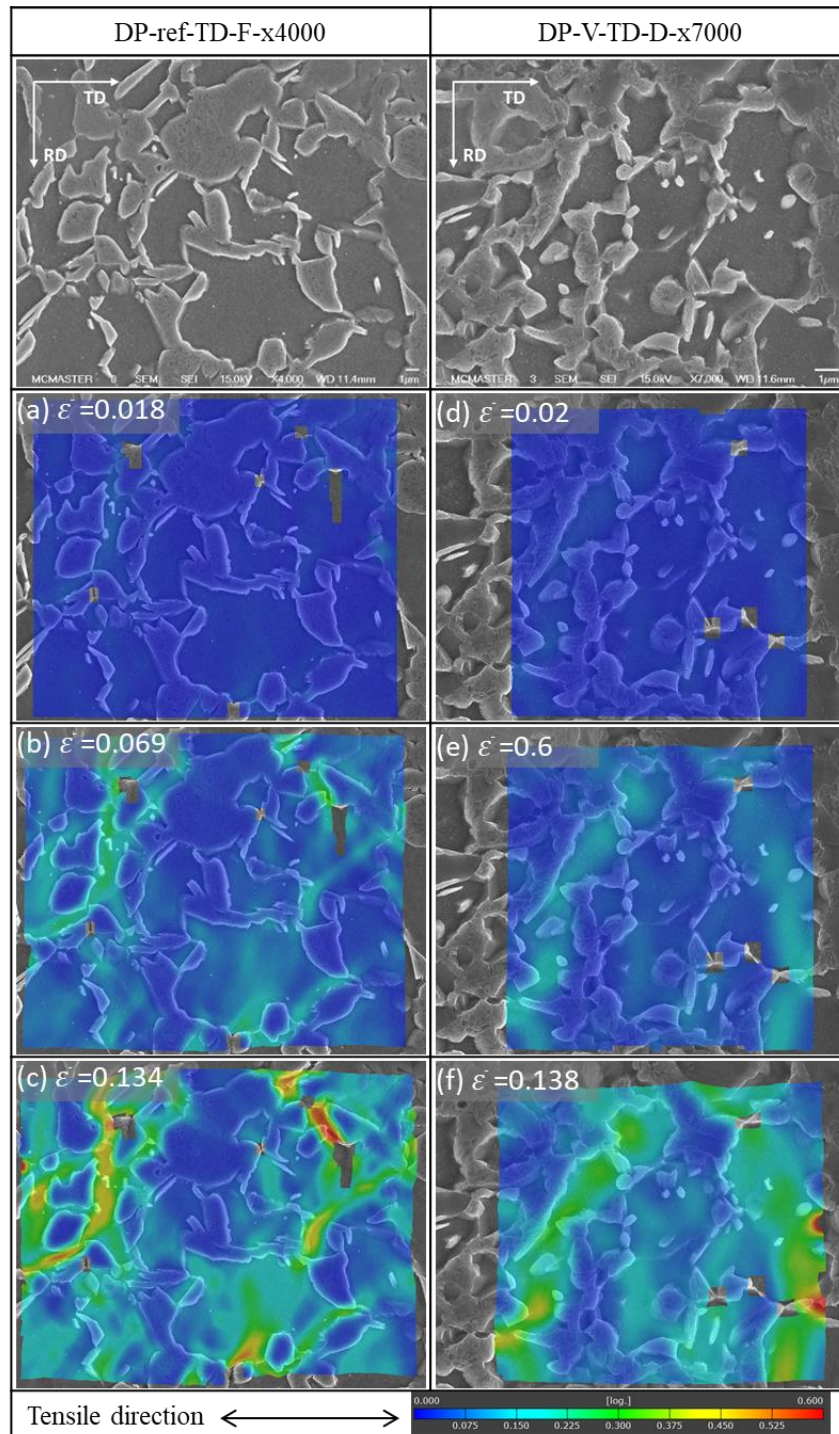
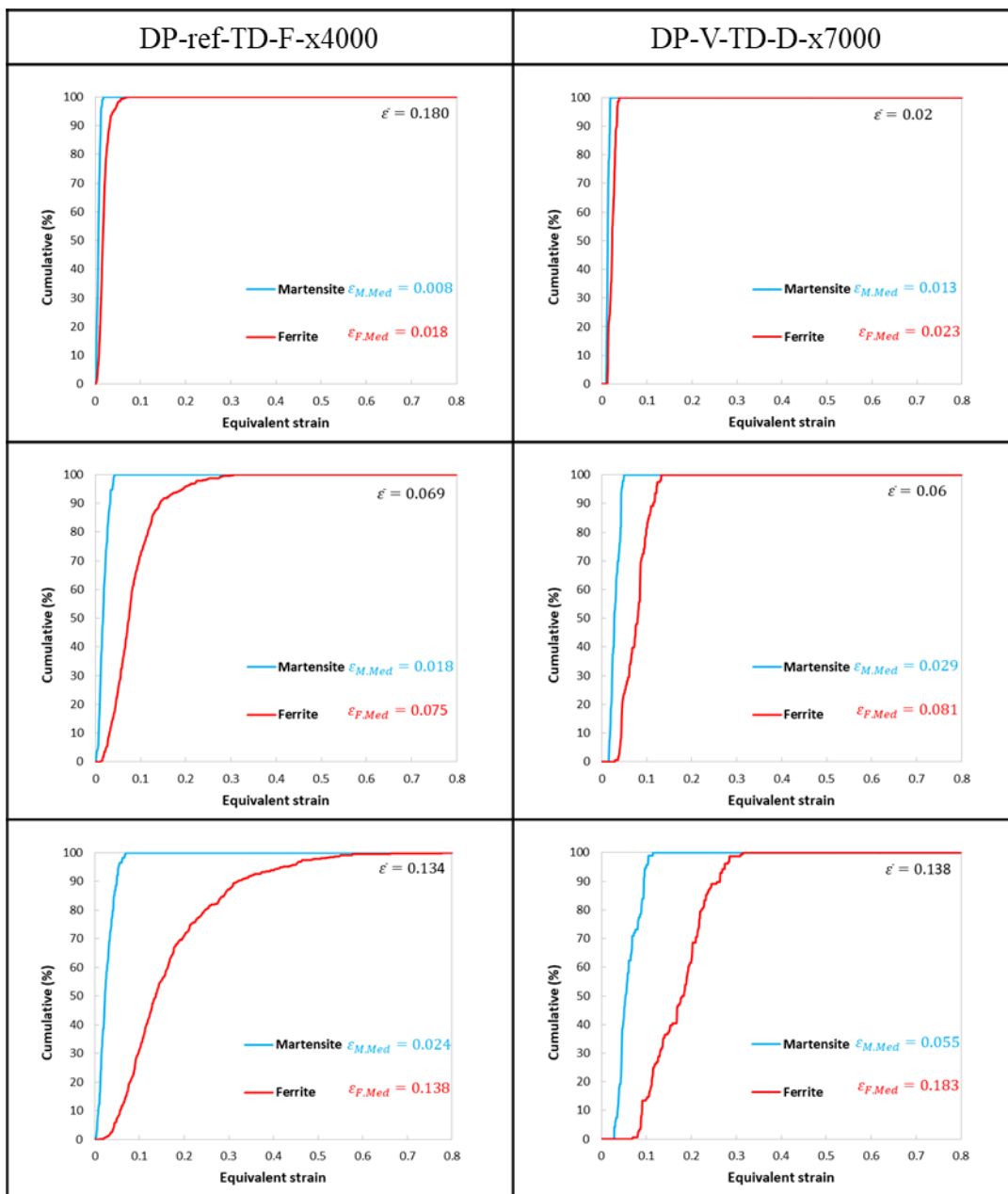


Figure 5-22 Equivalent strain maps comparison between steels along TD directions.

The legend is set to be same for all the stages

(1)



(2)

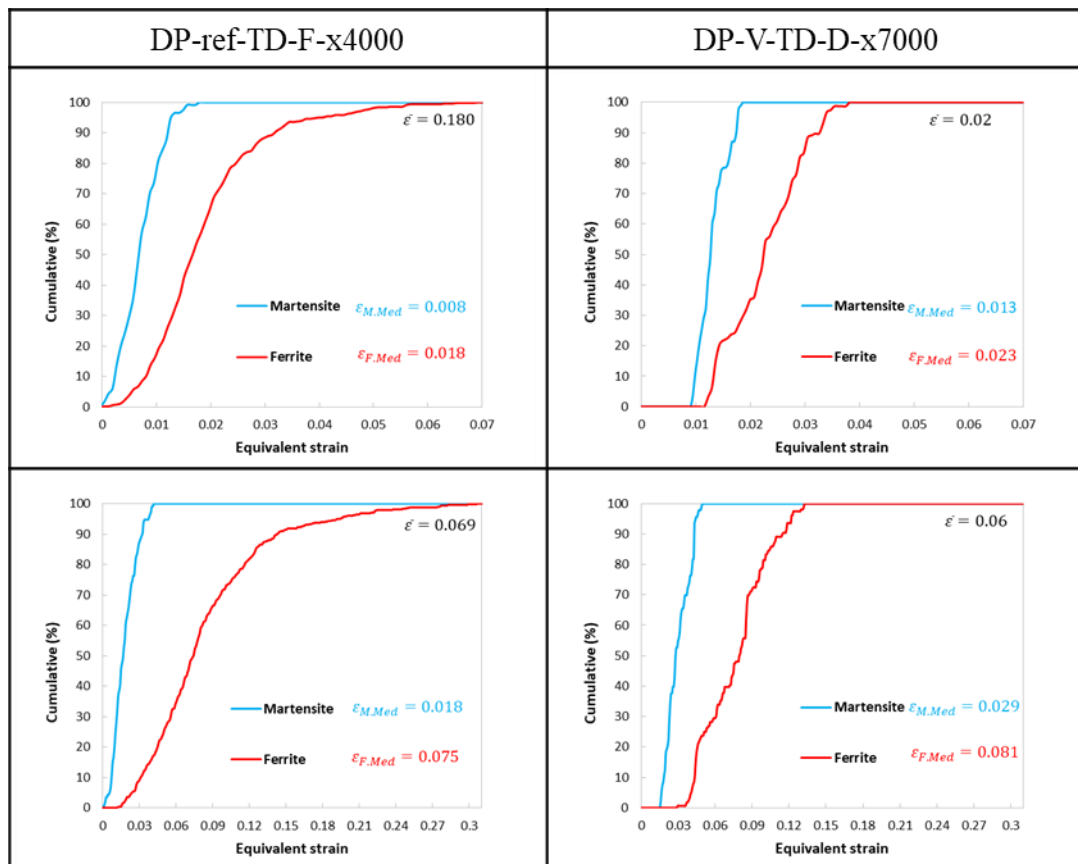


Figure 5-23 Cumulative equivalent strain distribution between ferrite and martensite for DP-ref and DP-V steels along TD directions.

Figure 5-24 presents the average partitioned strain between ferrite and martensite along the RD and TD directions, as a function of ϵ_x and $\bar{\epsilon}$, respectively. The median value instead of the average value of each phase at a certain stage is used. The upper/lower bounds for each point corresponds to the maximum/minimum value, respectively. In other words, the bars in the figure denote the full range of experimental scatter. The distribution of the data set is not Gaussian, and the median value is smaller than the average value for each stage. Moreover, all the data sets are widely scattered, especially for ferrite. Kadkhodapour et al. [80] performed several

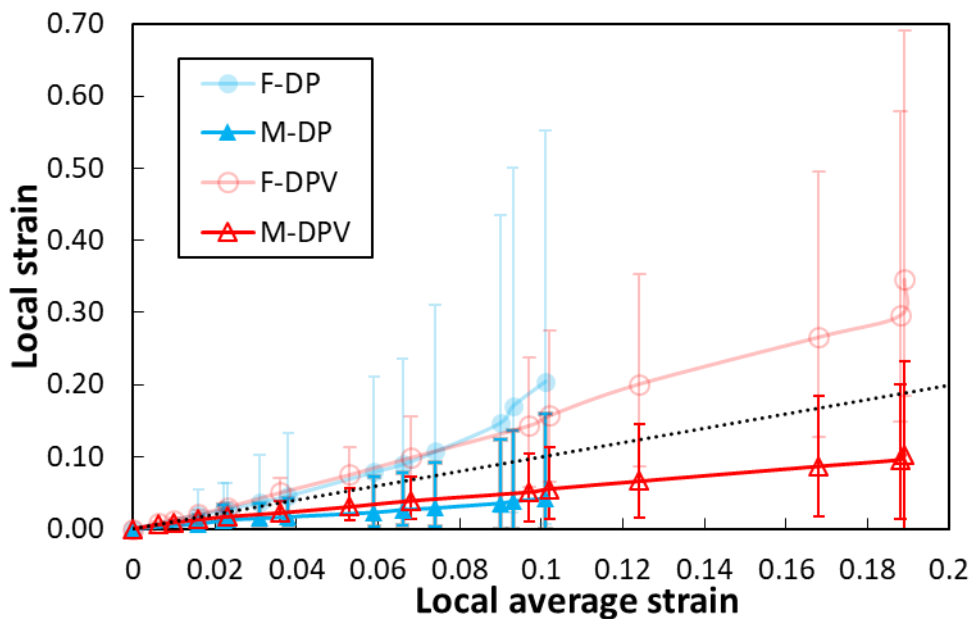
nano-hardness tests on UFG DP steels and obtained observed noticeable near α/α' interface hardening caused by the higher density of geometrical necessary dislocations close to the interface. This can explain the large scattered data here.

For all the cases, the median partitioned strain in the ferrite phase is significantly larger than that in martensite. However, despite the fact that DP-V steels are more homogeneous in terms of the strength compatibility between the two phases, the strain partitioning is similar in all cases, which is different from the results of hot-rolled steels with and without V obtained by Kamikawa et al. [81]. The difference of strain partitioning might be generated from the finer microstructure here.

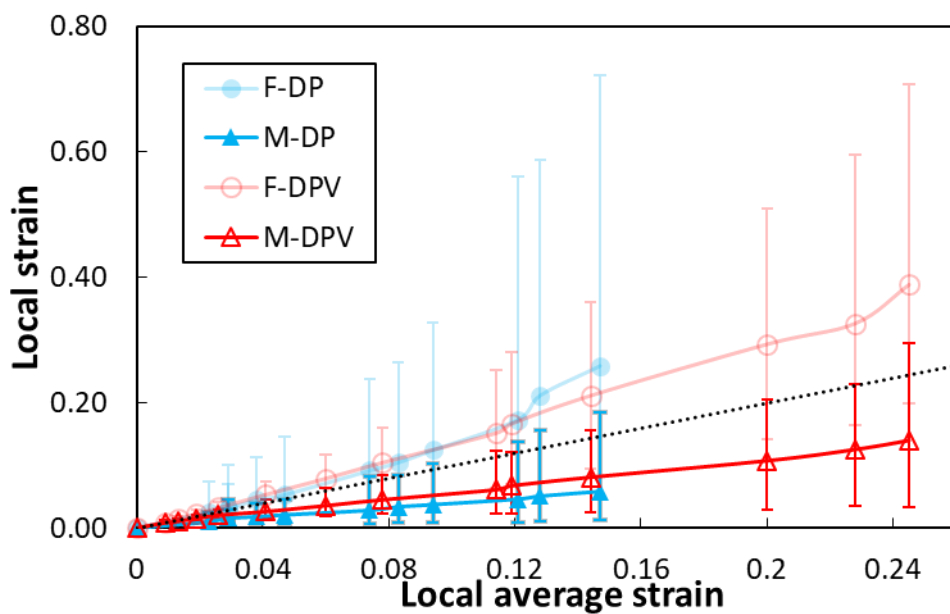
The median partitioned strain in the martensite of DP-V steels is higher than that in DP-ref steels, except ε_x along TD directions, despite the large error bars. In other words, there is more martensite deformation in DP-V steels, which indicates that α' in DP-V steels is softer than that in DP-ref steels and this is consistent to the nano-indentation results in section 5.3.2. In DP-V steels, α keeps deforming until reaching a very large strain compared to DP-ref steels.

The exception for ε_x along TD directions in Figure 5-24 can be related with the different behavior of DP-ref along TD directions in Figure 5-7. Both present a similar trend. There might be some different mechanisms in DP-ref along TD direction during tensile test.

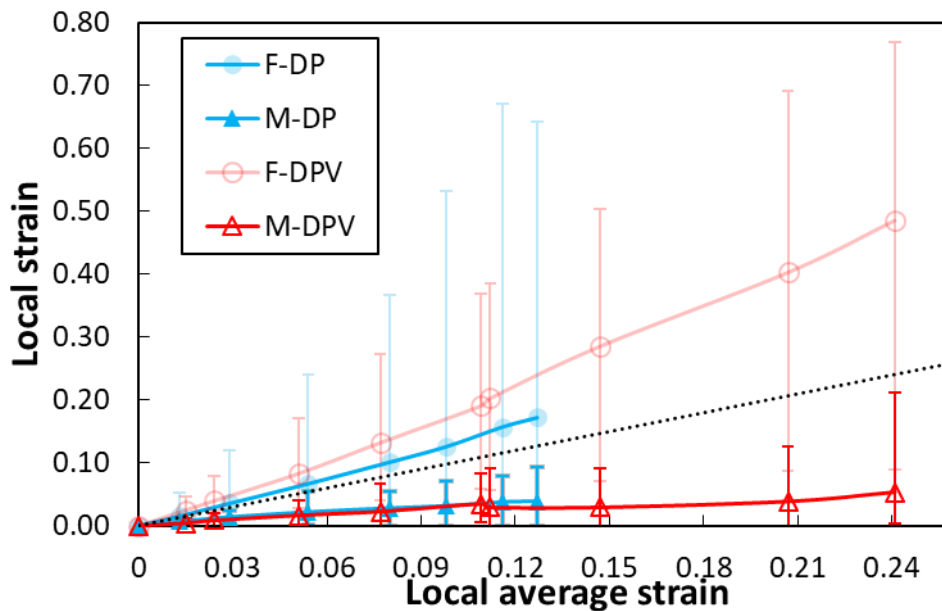
(a) ε_x along RD



(b) $\bar{\varepsilon}$ along RD



(c) ϵ_x along TD



(d) $\bar{\epsilon}$ along TD

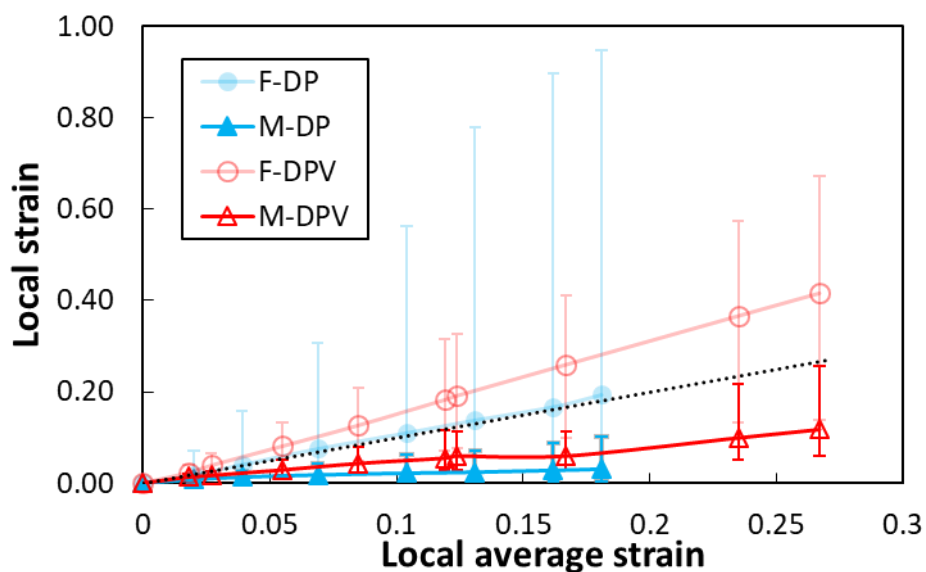


Figure 5-24 Partitioned strain between ferrite and martensite phases (median value), as a function of local average strain. Both strain along tensile directions (ϵ_x) and the von Mises equivalent strain ($\bar{\epsilon}$) are plotted.

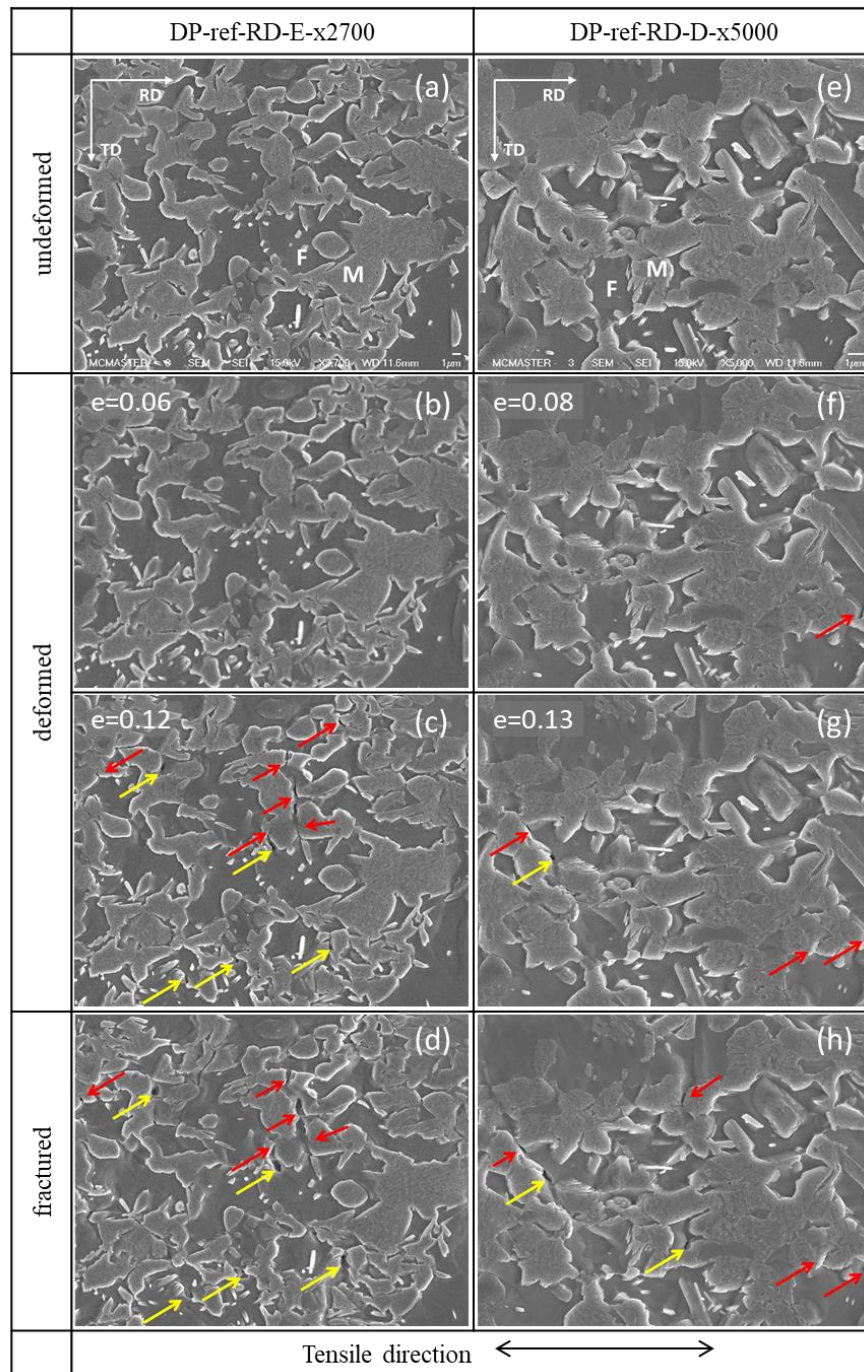
5.5 Micro-mechanisms of damage

5.5.1 Microscopic deformation characterization

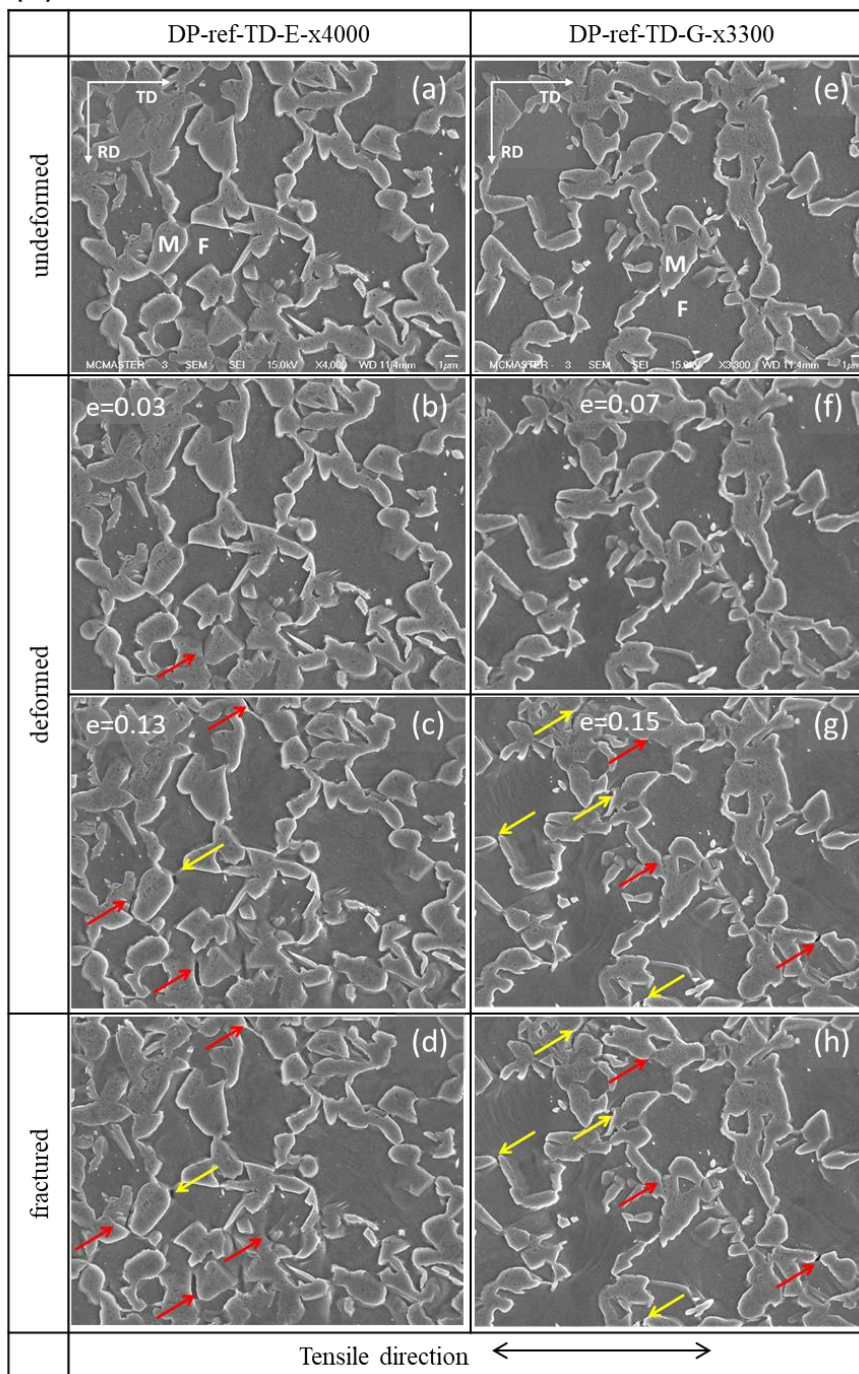
The investigated DP1300 steels failed in a ductile manner. To understand the deformation and damage mechanisms, the microscopic deformation behavior was studied.

One advantage of this project is that the whole deformation process rather than merely the microstructure after fracture is recorded throughout the experiment. Therefore, it is possible to track the entire process of microscopic deformation at various locations. Several series of SEM micrographs have been utilized to investigate the initiation and damage development in materials. Examples of microscopic deformation of DP-ref and DP-V along RD and TD directions including microstructures under deformation and after fracture are shown in Figure 5-25. Interfacial damages and martensite cracking are highlighted by yellow and red arrows, respectively. Initially, both steels deform as the strain is applied, and there is very little sign of microstructural damage from the SEM images up to the onset of necking. After reaching the necking point, microstructural damage develops rapidly. Most of the deformation occurs in ferrite grains. Martensite islands do not deform significantly until the material reaches large strain. Both interfacial voids growth and martensite cracking are found in all the scenarios while the scale of damage is smaller in DP-V steels. With the increase of applied strain, microstructural damage develops and interacts, which leads to the formation of catastrophic cracks and large voids. With the growth of voids and eventual coalescence of those cracks, the tensile specimens eventually are fractured.

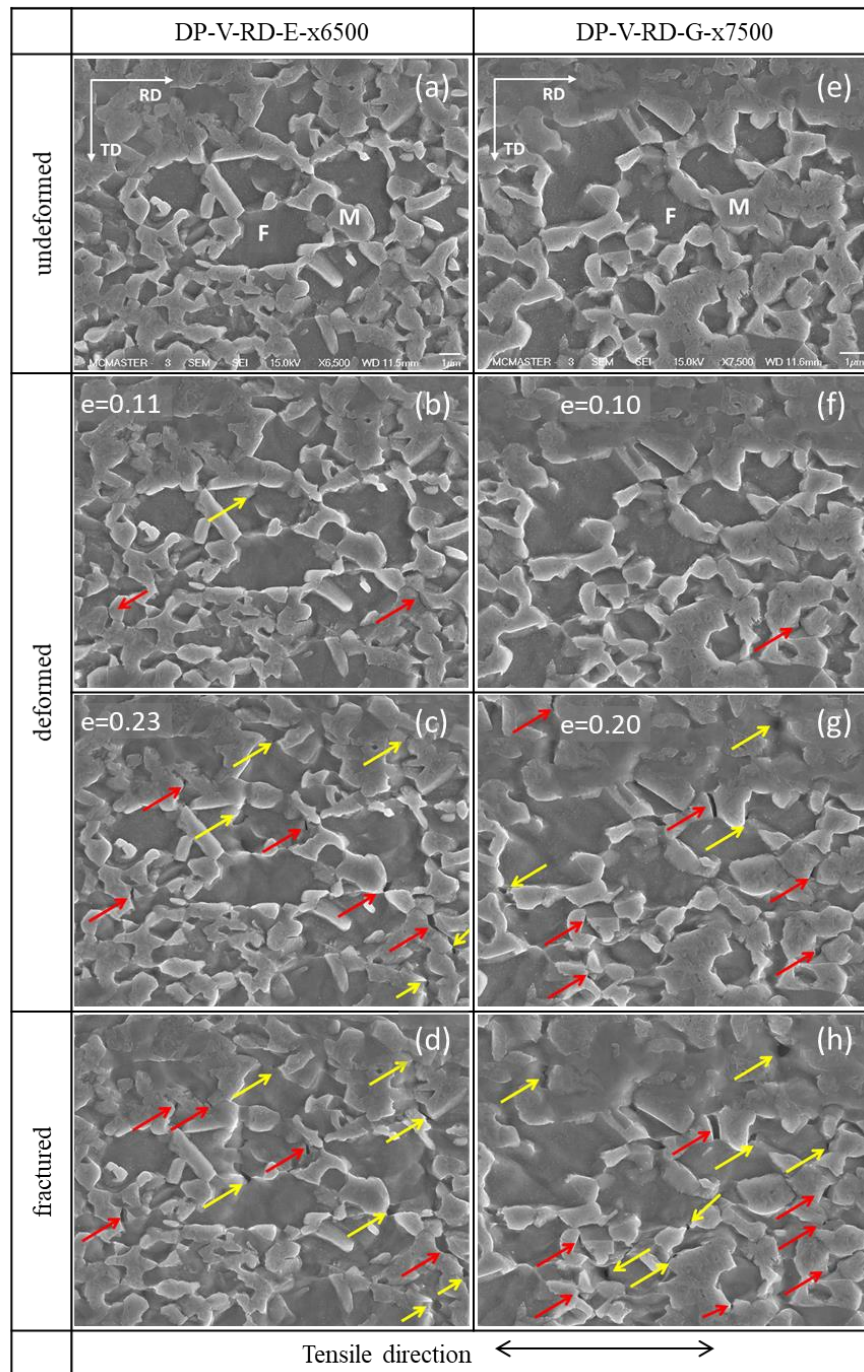
(1) DP-ref-RD



(2) DP-ref-TD



(3) DP-V-RD



(4) DP-V-TD

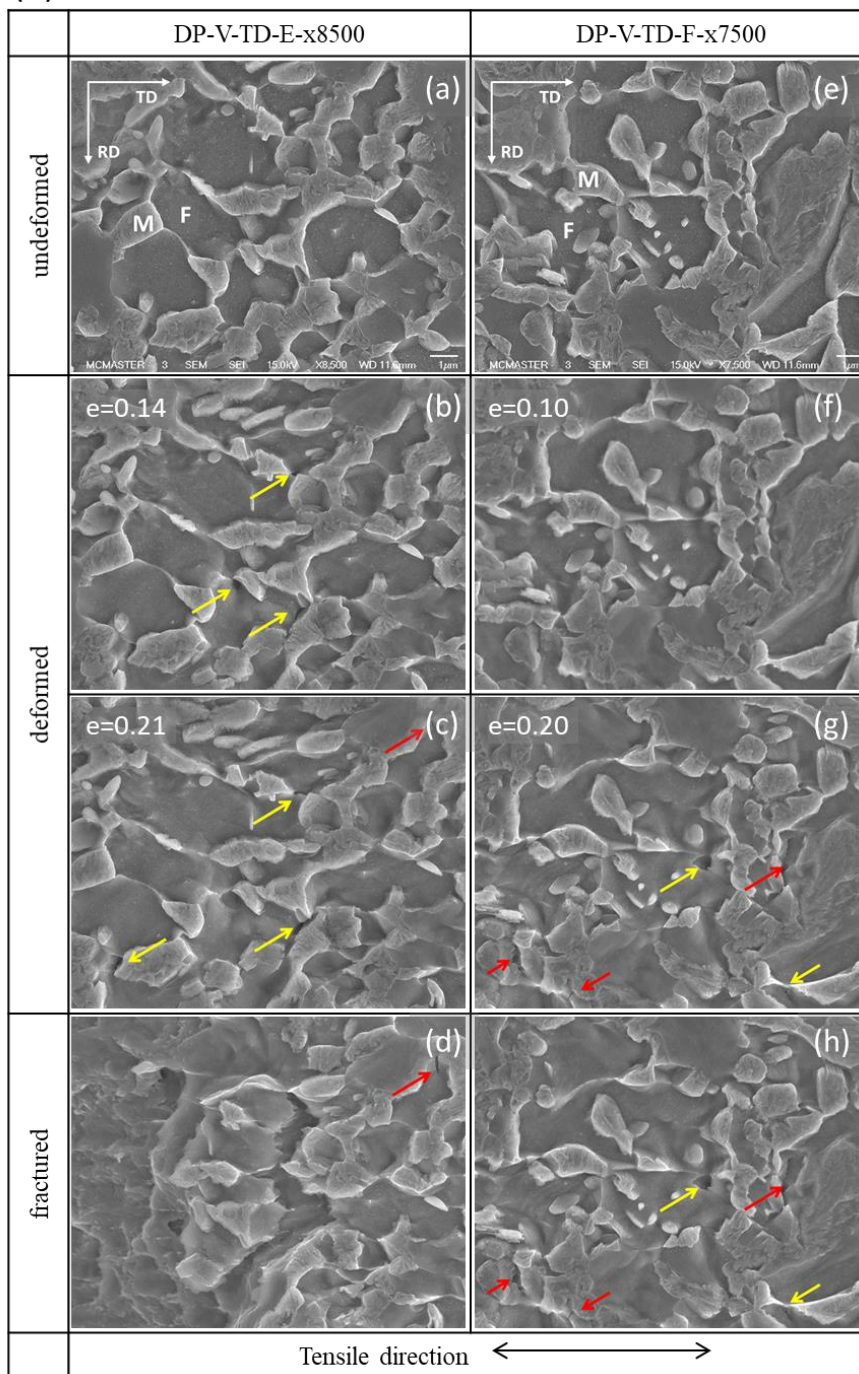


Figure 5-25 Damage accumulation process. (1) DP-ref steels along RD; (2) DP-ref steels along TD; (3) DP-V steels along RD; (4) DP-V steels along TD. Yellow arrow: interfacial damage; red arrow: martensite cracking.

In order to analyze the development of different types of microstructural damage, DP-ref steel along RD direction at a magnification of x2700 and DP-V steel along RD direction at a magnification of x7500 was selected to present the typical damage evolution process (Figure 5-26). The corresponding enlarged microstructural damage evolution in both steels are summarized in Figure 5-27.

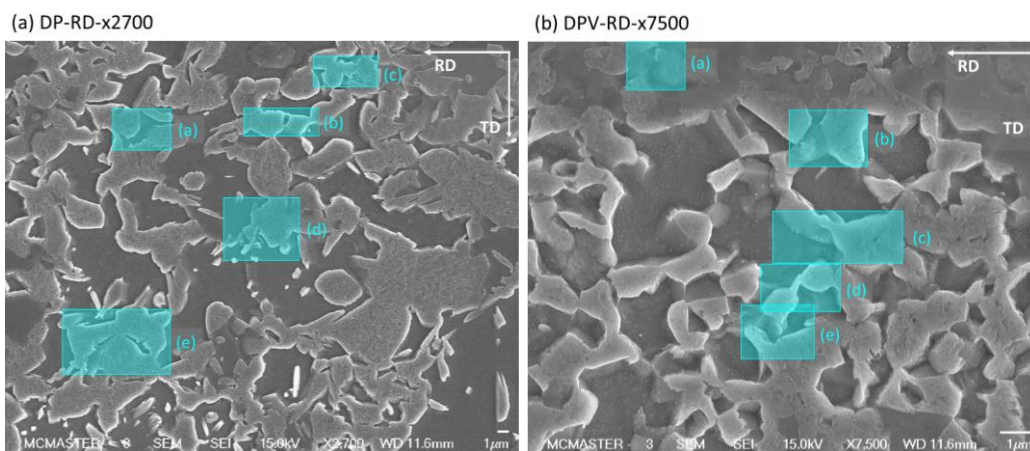


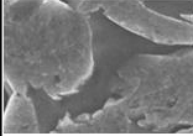
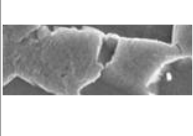
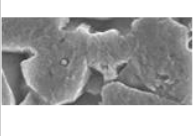
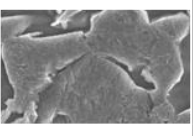
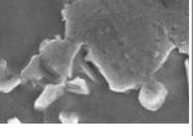
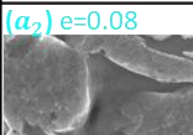
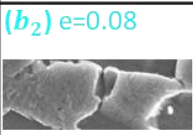
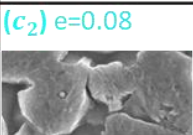
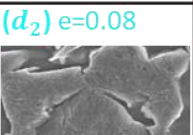
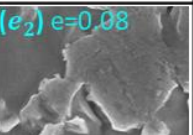
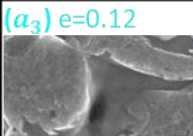
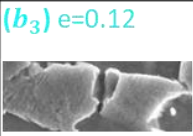
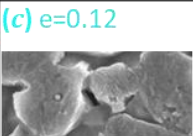
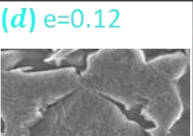
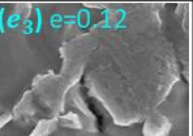
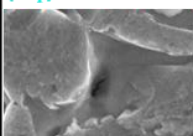
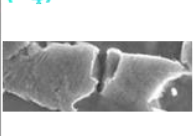
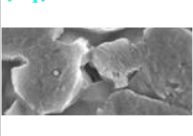
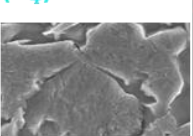
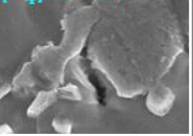
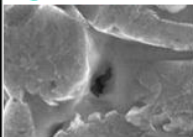
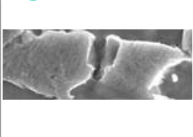
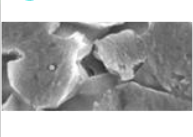
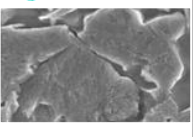
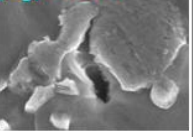
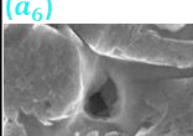
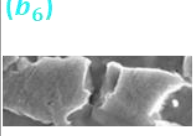
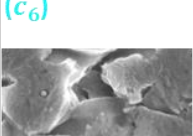
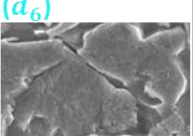
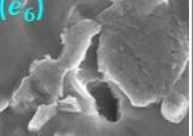
Figure 5-26 Selected locations to magnify microstructural damage evolution. (a) DP-ref steel along RD direction at a magnification of x2700; (b) DP-V steel along RD direction at a magnification of x7500. The selected locations are highlighted with blue boxes.

Interfacial voids and martensite cracking occur in both steels although the scale is much smaller in DP-V steels. The interfacial voids are formed due to the mechanical incompatibility between the martensite and ferrite phases. Those voids usually form in ferrite phases and grow bigger as the material is deformed (Figure 5-27 (1) (2) a). Martensite cracking can either occur transverse to the loading direction (Figure 5-27 (1) (2) b c) or some angle to the loading direction (Figure 5-27 (1) (2) d), which can be induced by shear localization. In addition, martensite cracking can also interact with interfacial voids. As illustrated in Figure 5-27 (1) e, the adjacent growth of

interfacial voids leads to the formation of micro-cracks throughout the martensite islands. Figure 5-27 (2) e shows that martensite cracking can result in the formation of interfacial voids in ferrite. Figure 5-27 (2) c indicates that even after martensite cracking has already occurred, the surrounding ferrite phase still undergoes very big via large deformation without forming voids.

It should be noted that micrographs merely record two-dimensional information with limited resolution. However, actual deformation of the materials is three-dimensional and those features which are very small cannot be easily identified.

(1) DP-RD

Interfacial voids growth in α	α' cracking I	α' cracking II	α' cracking III	α' cracking by tension + Interfacial voids growth	
(a ₁) e=0.03 	(b ₁) e=0.03 	(c ₁) e=0.03 	(d ₁) e=0.06 	(e ₁) e=0.06 	Small strain ↓ large strain
(a ₂) e=0.08 	(b ₂) e=0.08 	(c ₂) e=0.08 	(d ₂) e=0.08 	(e ₂) e=0.08 	
(a ₃) e=0.12 	(b ₃) e=0.12 	(c) e=0.12 	(d) e=0.12 	(e ₃) e=0.12 	
(a ₄) e=0.14 	(b ₄) e=0.14 	(c ₄) e=0.14 	(d ₄) e=0.14 	(e ₄) e=0.14 	
(a ₅) e=0.17 	(b ₅) e=0.17 	(c ₅) e=0.17 	(d ₅) e=0.17 	(e ₅) e=0.17 	
(a ₆) 	(b ₆) 	(c ₆) 	(d ₆) 	(e ₆) 	

(2) DPV-RD

Interfacial voids growth in α	α' cracking I	α' cracking II	α' cracking III	α' cracking by tension + Interfacial voids growth	
(a ₁) e=0.10	(b ₁) e=0.10	(c ₁) e=0.06	(d) e=0.10	(e ₁) e=0.10	Small strain ↓ large strain
(a ₂) e=0.11	(b ₂) e=0.11	(c ₂) e=0.10	(d ₂) e=0.11	(e ₂) e=0.11	
(a ₃) e=0.14	(b ₃) e=0.14	(c) e=0.11	(d ₃) e=0.14	(e ₃) e=0.14	
(a ₄) e=0.20	(b ₄) e=0.20	(c ₄) e=0.23	(d ₄) e=0.20	(e ₄) e=0.20	
(a ₅) e=0.28	(b ₅) e=0.28	(c ₅) e=0.28	(d ₅) e=0.28	(e ₅) e=0.28	
(a ₆)	(b ₆)	(c ₆)	(d ₆)	(e ₆)	

Figure 5-27 SEM images revealing damage development in steels. (1) DP-ref steels
 (2) DP-V steels

5.5.2 Correlation between microscopic and macroscopic deformation

As shown in Figure 5-28, the microscopic strain along the tensile direction results can be related to the macroscopic stress-strain curves of DP steels to describe the sequence of events until fracture. According to the figure, the strain required to initiate damage is higher in DP-V alloy (0.11) compared to DP-ref alloy (0.10), but the difference is not large. Despite similar damage initiation strain in both steels, DP-V steel still enjoys much higher post-uniform elongation along the RD direction, which might be the result of a slower void growth and accumulation rate in DP-V steel.

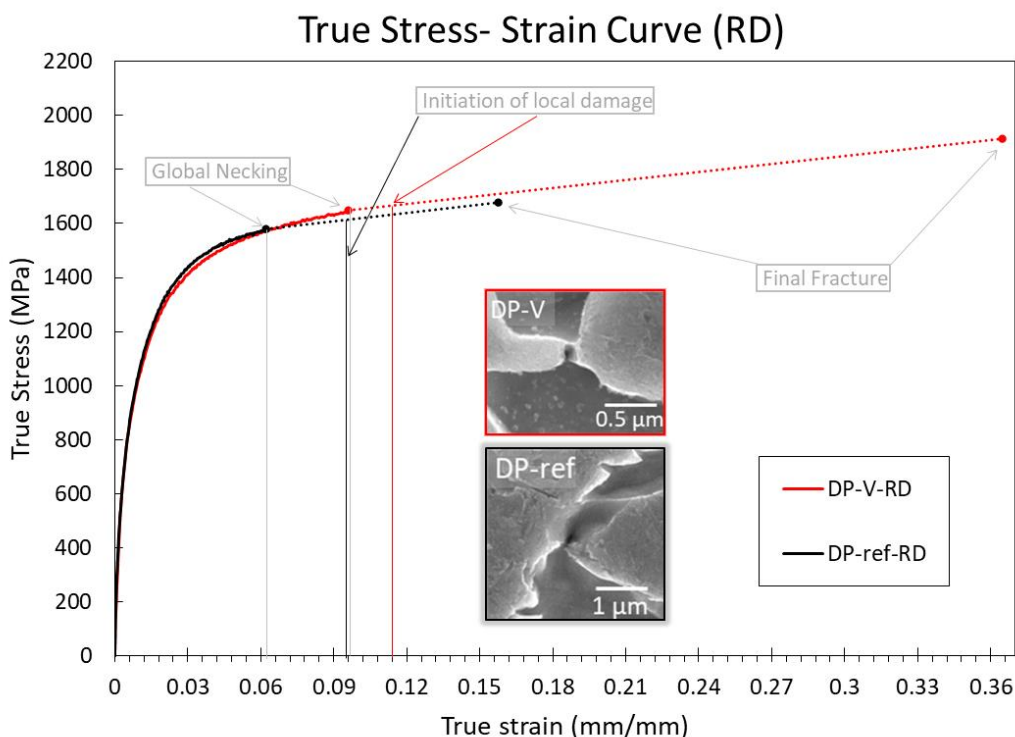


Figure 5-28 Fracture map for DP1300 along RD

5.6 Fracture Surface analysis

Fractography was carried out to understand the failure type of DP1300 steels, XCT scans were performed to analyze the void distribution quantitatively.

5.6.1 Fractography

Fracture surfaces of DP-ref and DP-V steels are shown in Figure 5-29 and Figure 5-30, respectively. The fracture surfaces of the two steels are dominated by equiaxed dimples and some quasi-cleavage fracture features were observed in the DP-ref steel (Figure 5-29 B) and DP-V steels (Figure 5-30 A and B). The dominant fracture mode of these two steels is ductile. Furthermore, the overall size of dimples is much finer in DP-V steels compared to DP-ref steels, which can be attributed to finer microstructure and larger post-uniform elongation in the DP-V steel. Figure 5-30 D reveals an example of dimples at the nano-scale, which might result from void nucleation near those V(C, N) particles and this hypothesis need to be further investigated.

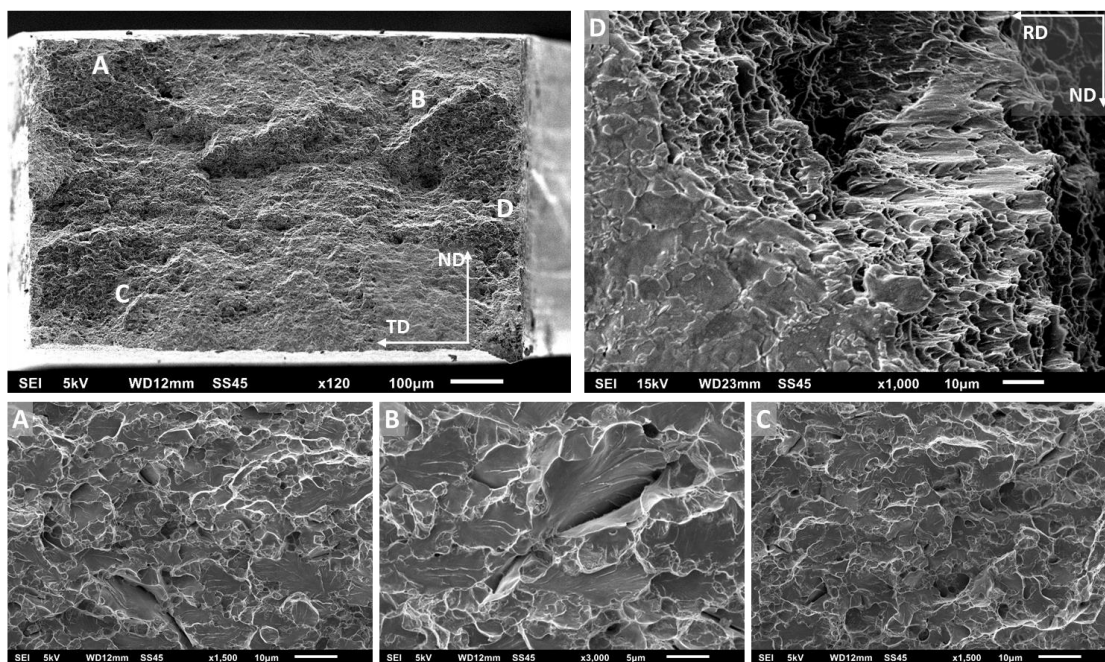


Figure 5-29 Fracture surface of the DP-ref steel.

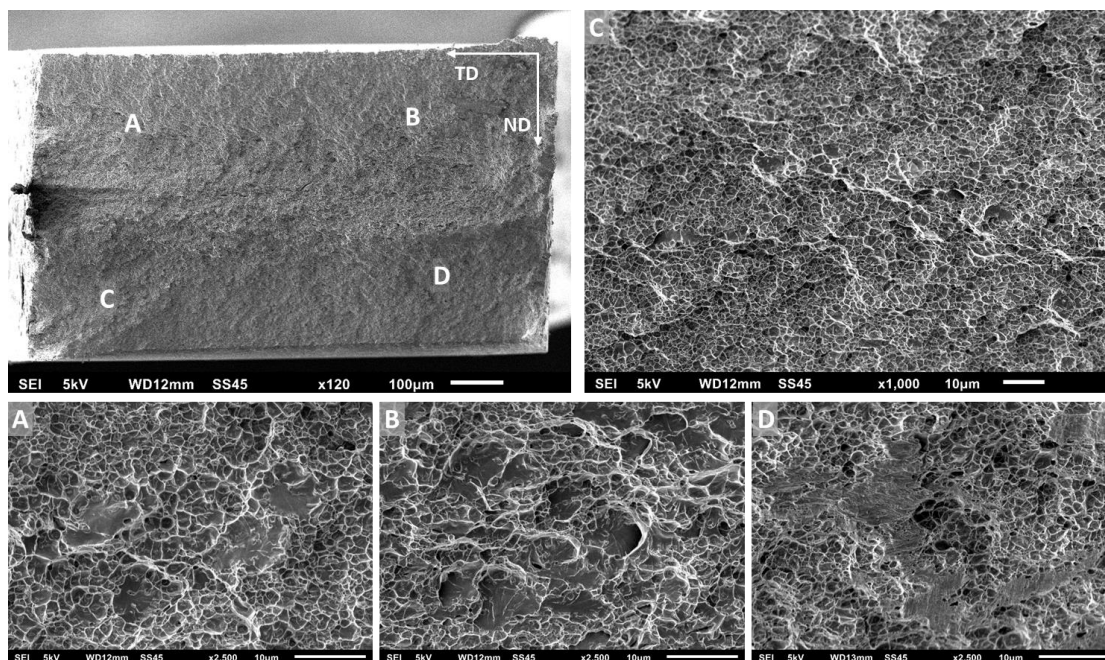


Figure 5-30 Fracture surface of the DP-V steels

5.6.2 X-ray Computed Tomography (XCT) Scans

The 3D XCT models of the fractured DP-ref and DP-V steels after fracture are provided in Figure 5-31 and Figure 5-32, respectively. Dimples (open porosity: green) on the fracture surfaces and voids (closed porosity: red) beneath the fracture surfaces are presented in the models. The models are shown from different angles for better observation. The models show that most of the voids are located just below the fracture surface.

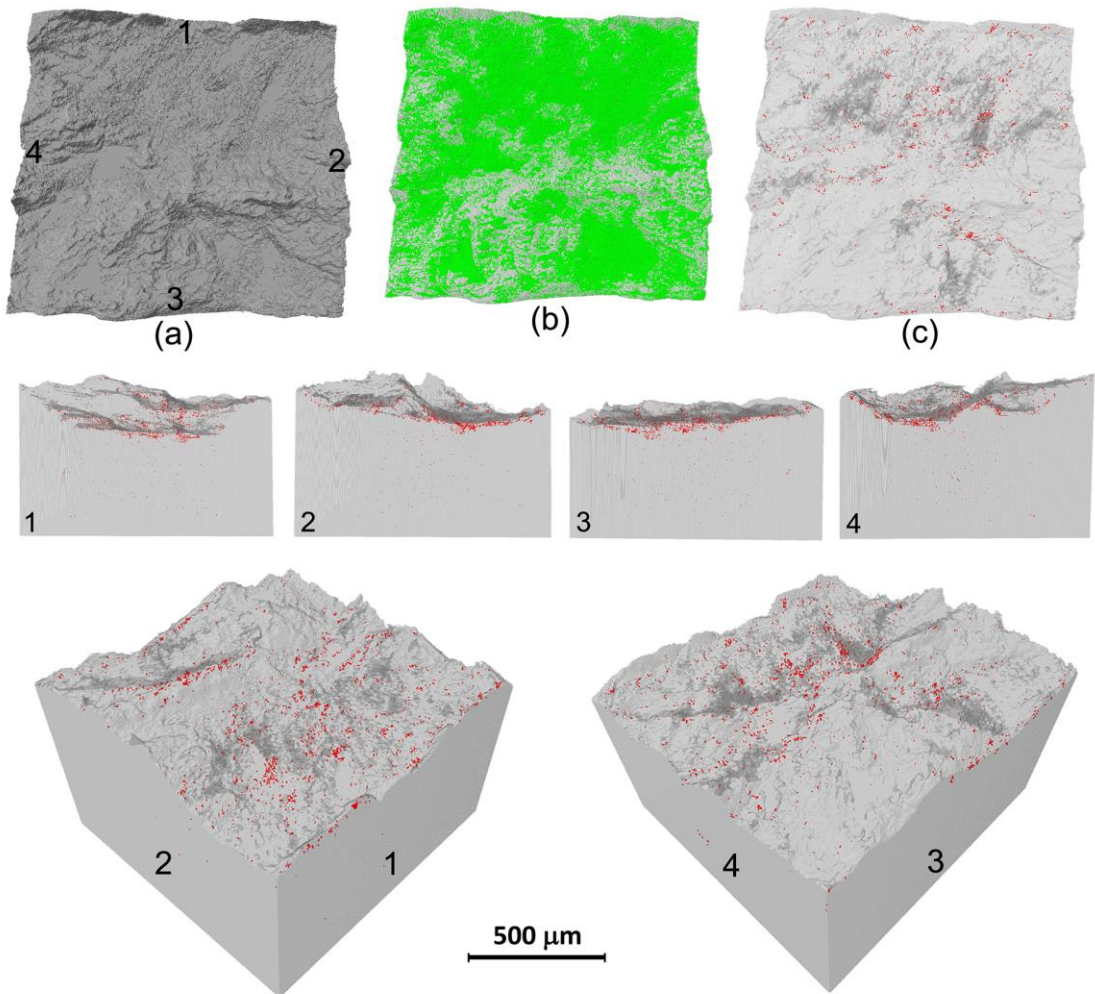


Figure 5-31 3D representation of the population of dimples or voids in fractured samples of DP-ref steel (a) fracture surface, (b) dimples on the fracture surface in green, and (c) voids beneath the fracture surface in red. The 3D model is presented from varied views in the second row and 3D perspectives are shown in the third row.

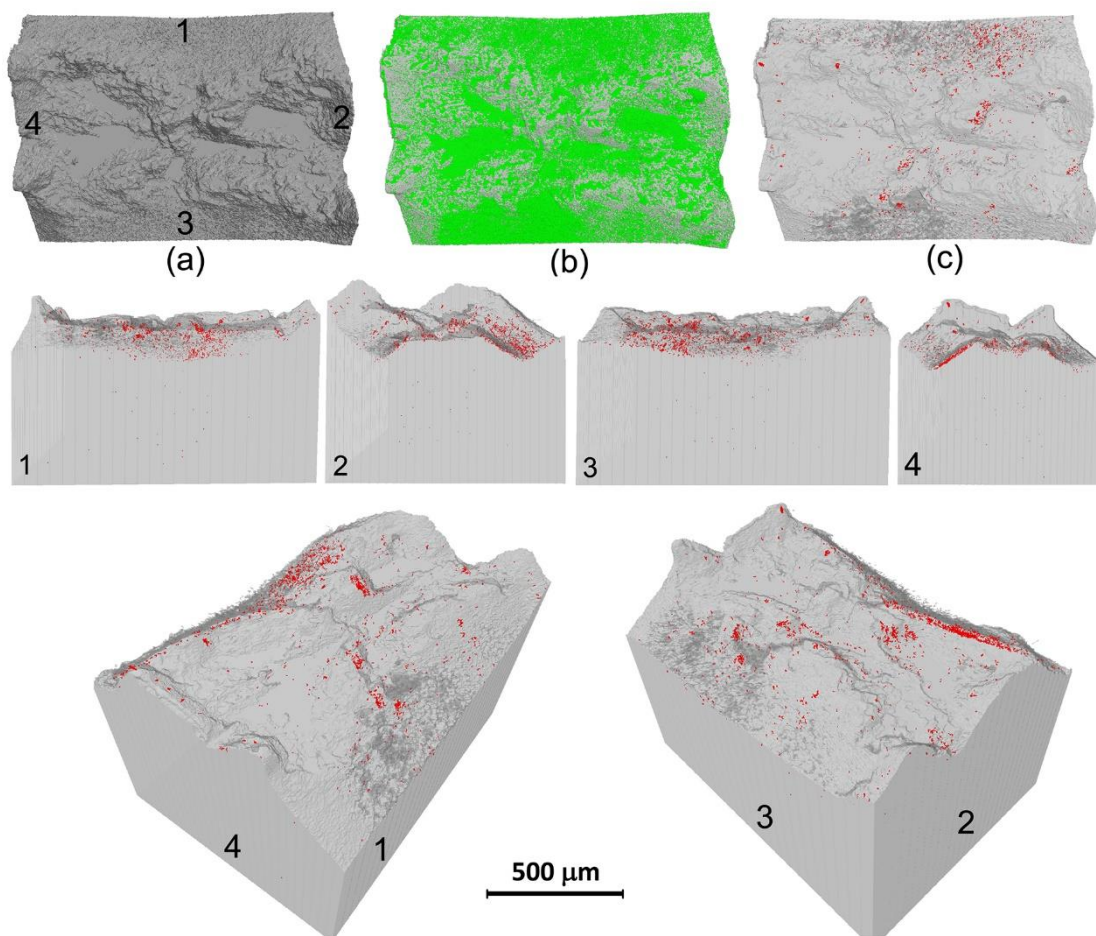


Figure 5-32 3D representation of the population of dimples or voids in fractured samples of DP-V steel (a) fracture surface, (b) dimples on the fracture surface in green, and (c) voids beneath the fracture surface in red. The 3D model is presented from varied views in the second row and 3D perspectives are shown in the third row.

Table 5-8 Quantitative data for voids and dimples obtained from XCT scans

Alloys	Voids (50 largest voids)		Dimples	
	Volume fraction (%)	Mean diameter (μm)	Area fraction (%)	Mean diameter (μm)
DP-ref	0.73	5.6	78.9	3.0
DP-V	0.42	4.9	87.7	1.7

Table 5-8 provides the quantitative information of microstructural damage obtained from XCT scans. The data is obtained from the fractured parts of both alloys. Since only the largest voids play an important role in fracture, the void mean diameter is calculated for the largest 50 voids in each steel. However, in the case of dimple mean diameter, all dimples were considered. The volume fraction of voids is 0.73% and 0.42% inside of the fractured samples of DP-ref and DP-V steels, respectively. The mean diameter of voids is 5.6 μm and 4.9 μm in DP-ref and DP-V steels, respectively. Since the initial voids volumes were similar in both steels, the XCT scans suggest that damage develops more rapidly in the DP-ref steel during the uniaxial tensile test. The quantitative analysis of voids obtained from XCT scans is presented in Figure 5-33. The data is obtained along the necked area of the fractured samples and reported as a function of true local strain in the necking region. The local true strains are calculated according to Equation (5.1.5). Figure 5-33 (a) shows that for both steels, the void area fraction increases exponentially with increasing strain and the increase in DP-ref steel is more rapid in comparison with DP-V steel. Figure 5-33 (b) illustrates the density of voids as a function of true strain. The density of voids in DP-ref is initially larger and increases slowly and linearly with the increase of strain. Combining the data in Figure 5-33 (a) and (b), it can be founded that despite the increase of voids area fraction, the density of voids remains almost constant with increasing strain. This suggests that the rate of void nucleation and coalescence are close to each other in the DP-ref steel during uniaxial tensile testing. However, the increase in density of voids in DP-V steel presents a sigmoidal shape with an inflection point at a local strain of around 0.25. Below the inflection point, the density of voids rises at an increasing rate, which can be ascribed to the accelerated nucleation of interfacial voids due to more severe ferrite/martensite interface decohesion during post-uniform deformation. Because of the finer microstructure of DP-V steel, the

higher α/α' interface area leads to a larger number of interfacial voids. Above the inflection point, the density of voids in DP-V steel keeps increasing but with a decreasing rate. This might be caused by enhanced void coalescence partly offset by continued void nucleation. The density of voids in DP-V steel is initially lower than DP-ref steel but becomes higher compared to DP-ref steel. It should be noted that higher values of void density do not necessarily mean earlier fracture. The change suggests that the rate of void coalescence in DP-V steel is lower than that in DP-ref steel. This helps to validate that refining microstructure suppresses the coalescence of voids and leads to high post uniform elongation and thus high ductility in DP-V steel. Figure 5-33 (c) shows that the void average area in DP-V steels is much smaller in the DP-ref steel. It should be noted that there is a notable proportion of voids in the DP-V steel, specifically the interfacial voids, are sub-micron and do not play a significant role in formation of larger voids, micro-cracks and occurrence of fracture.

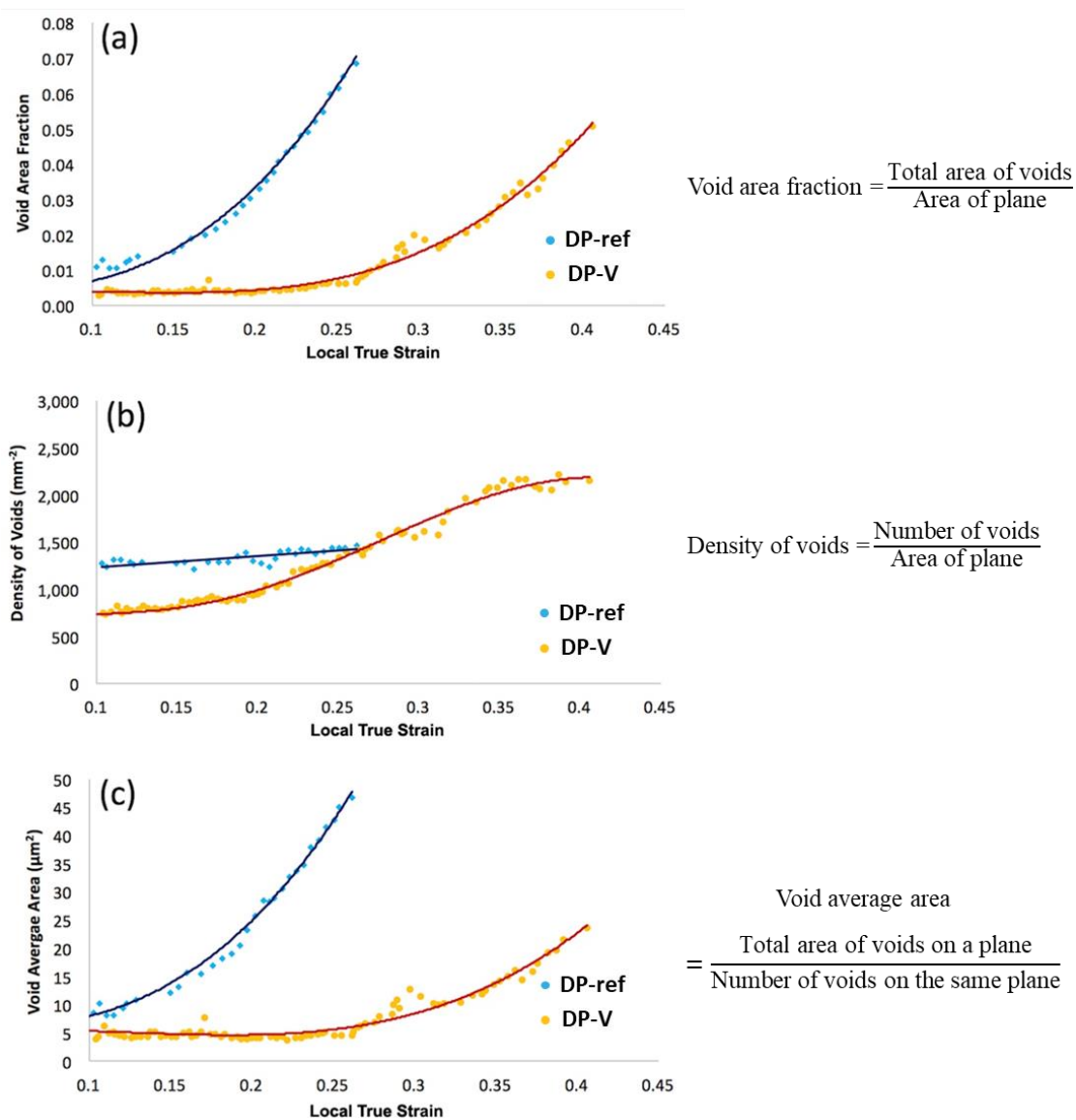


Figure 5-33 Quantitative analysis of voids in the necked area of the fractured samples obtained from XCT scans

6 Conclusions

A detailed quantitative study of the influence of vanadium on DP1300 steels using macroscopic tensile tests, nano-indentation measurements, and μ -DIC analysis coupled with SEM has been conducted. The properties of high strength UFG DP1300 steel have been determined. Compared to the reference alloy with similar martensite volume fractions of around 50% martensite, it was found that 0.14 wt% of vanadium addition lead to:

- A significant grain refinement for both ferrite and martensite (by about a factor of 3).
- A more homogeneous material in terms of the distribution of martensite.
- An increase of post-uniform elongation and an improvement of overall ductility (true strain to fracture) while maintaining similar strength.
- Ferrite phase hardening along with softening of the martensite islands, leading to an increase in mechanical homogeneity and increased deformation of the martensite.
- Suppression of the void coalescence during the post-uniform elongation stage.

This work has demonstrated that refining the microstructure of a material and improving mechanical compatibility between the two phases is a viable approach to produce high strength steels with enhanced ductility, especially in terms of post-uniform elongation and true strain to fracture. This can have important consequences for the use of such materials in automotive applications that involving bending and complex stress states.

Reference

- [1] W. Bleck, “Cold-rolled, high strength sheet steels for auto applications,” *JOM*, no. July, pp. 26–27, 1996.
- [2] O. Bouaziz, H. Zurob, and M. Huang, “Driving force and logic of development of advanced high strength steels for automotive applications,” *Steel Res. Int.*, vol. 84, no. 10, pp. 937–947, 2013.
- [3] S. Keeler, M. Kimchi, and P. J Mooney, “Advanced High-Strength Steels Application Guidelines Version 6.0,” no. September, pp. 1–314, 2017.
- [4] C. C. Tasan *et al.*, “An Overview of Dual-Phase Steels: Advances in Microstructure-Oriented Processing and Micromechanically Guided Design,” *Annu. Rev. Mater. Res.*, vol. 45, no. 1, pp. 391–431, 2014.
- [5] M. S. Rashid, “Dual Phase Steels,” *Annu. Rev. Mater. Sci.*, vol. 11, pp. 245–66, 1981.
- [6] M. Sarwar and R. Priestner, “Influence of ferrite-martensite microstructural morphology on tensile properties of dual-phase steel,” *J. Mater. Sci.*, vol. 31, no. 8, pp. 2091–2095, 1996.
- [7] J. Kadkhodapour, S. Schmauder, D. Raabe, S. Ziaei-Rad, U. Weber, and M. Calcagnotto, “Experimental and numerical study on geometrically necessary dislocations and non-homogeneous mechanical properties of the ferrite phase in dual phase steels,” *Acta Mater.*, vol. 59, no. 11, pp. 4387–4394, 2011.
- [8] C. Peng-Heng and A. G. Preban, “The effect of ferrite grain size and martensite volume fraction on the tensile properties of dual phase steel,” *Acta Metall.*, vol. 33, no. 5, pp. 897–903, 1985.
- [9] A. Ghatei Kalashami, A. Kermanpur, A. Najafizadeh, and Y. Mazaheri, “Effect of Nb on Microstructures and Mechanical Properties of an Ultrafine-Grained Dual Phase Steel,” *J. Mater. Eng. Perform.*, vol. 24, no. 8, pp. 3008–3017,

2015.

- [10] Y. Gong, “The Mechanical Properties and Microstructures of Vanadium Bearing High Strength Dual Phase Steels Processed with Continuous Galvanizing Line Simulations,” *Univ. Pittsburgh*, 2015.
- [11] T. Hayami, S., and Furakawa, “Family of High-Strength Cold-Rolled Steels.” *Proc. Conf. on Microalloying 75*, Union Carbide Corporation, New York, pp. 311–321, 1977.
- [12] W. Callister and D. Rethwisch, *Materials science and engineering: an introduction*. US: John Wiley & Sons, Inc., 2007.
- [13] J. H. Woodhead, “The Physical Metallurgy of Vanadium Steels,” *Vanadium in High-Strength Steel*. pp. 3–10, 1979.
- [14] P. S. Mitchell, “The use of vanadium,” *Use Vanadium Steel - Proc. Vanitec Symp.*, pp. 1–25, 2001.
- [15] R. J. Glodowski, “A Review of Vanadium Microalloying in Hot Rolled Steel Sheet Products,” *Int. Semin. 2005 Appl. Technol. Vanadium Flat – Roll. Steels*, pp. 43–51, 2005.
- [16] J. G. Speer, “Vanadium in Cold-rolled Sheet Steels,” *Proc. Int. Semin. Appl. Technol. Vanadium Flat*, p. 34, 2005.
- [17] H. Asahi, D. Hirakami, and S. Yamasaki, “Hydrogen Trapping Behavior in Vanadium-added Steel,” *ISIJ Int.*, vol. 43, no. 4, pp. 527–533, 2003.
- [18] K. He and D. V. Edmonds, “Formation of acicular ferrite and influence of vanadium alloying,” *Mater. Sci. Technol.*, vol. 18, no. 3, pp. 289–296, 2002.
- [19] D. Raabe, “Dual phase steels,” <http://www.dierk-raabe.com/dual-phase-steels/>.
- [20] N. Fonstein, *Advanced High Strength Sheet Steels*. Springer International Publishing Switzerland, 2015.
- [21] G. T. Koo, J., and M. Young, and, “On the Law of Mixtures and Dual-Phase

- Steels,” *Metall. Mater. Trans. A*, vol. 11, no. 5, pp. 852–854, 1980.
- [22] Z. Jiang, J. Lian, and J. Chen, “Strain hardening behaviour and its relationship to tensile mechanical properties of dual phase steel,” *Mater. Sci. Technol.*, vol. 8, no. 12, pp. 1075–1081, 1992.
- [23] W. F. Hosford, *Metal forming: Mechanics and metallurgy*, Fourth Edi. New York, 2011.
- [24] R. Rana and S. B. Singh, *Automotive Steels: Design, Metallurgy, Processing and Applications*. 2016.
- [25] G. Krauss, *Steels: Processing, Structure, and Performance*. 2015.
- [26] D. A. Korzekwa, D. K. Matlock, and G. Krauss, “Dislocation substructure as a function of strain in a dual-phase steel,” *Metall. Trans. A*, vol. 15, no. 6, pp. 1221–1228, 1984.
- [27] E. Ahmad, T. Manzoor, M. M. A. Ziai, and N. Hussain, “Effect of martensite morphology on tensile deformation of dual-phase steel,” *J. Mater. Eng. Perform.*, vol. 21, no. 3, pp. 382–387, 2012.
- [28] Y. Ling, “Uniaxial True Stress-Strain after Necking,” *AMP J. Technol.*, vol. 5, no. 1, pp. 37–48, 2004.
- [29] G. Krauss, “Martensite in steel: strength and structure,” *Mater. Sci. Eng. A*, vol. 273–275, pp. 40–57, 1999.
- [30] N. Fonstein, M. Kapustin, N. Pottore, I. Gupta, and O. Yakubovsky, “Factors that determine the level of the yield strength and the return of the yield-point elongation in low-alloy ferrite-martensite steels,” *Phys. Met. Metallogr.*, vol. 104, no. 3, pp. 315–323, 2007.
- [31] A. N. Bortsov and N. M. Fonstein, “Influence of carbon concentration on the mechanical properties of low carbon ferrite-martensite steels.” pp. 142–48, 1984.

- [32] R. G. Davies, "Influence of martensite composition and content on the properties of dual phase steels," *Metall. Trans. A*, vol. 9, no. 5, pp. 671–679, 1978.
- [33] M. F. Ashby, "Work hardening of dispersion-hardened crystals," *Philos. Mag.*, vol. 14, no. 132, pp. 1157–1178, 1966.
- [34] G. R. Speich and R. L. Miller, "Mechanical properties of ferrite-martensite steels," *Struct. Prop. dual-phase steels*, pp. 145–182, 1979.
- [35] C. a N. Lanzillotto and F. B. Pickering, "Structure-property relationships in dual phase steels," *Met. Sci.*, vol. 16, pp. 371–382, 1982.
- [36] L. F. Ramos, D. K. Matlock, and G. Krauss, "On the deformation behavior of dual-phase steels," *Metall. Trans. A*, vol. 10, no. 2, pp. 259–261, 1979.
- [37] P. Movahed, S. Kolahgar, S. P. H. Marashi, M. Pouranvari, and N. Parvin, "The effect of intercritical heat treatment temperature on the tensile properties and work hardening behavior of ferrite-martensite dual phase steel sheets," *Mater. Sci. Eng. A*, vol. 518, no. 1–2, pp. 1–6, 2009.
- [38] N. Matsumura and M. Tokizane, "Microstructure and mechanical properties of dual phase steels produced by intercritical annealing of lath martensite," *Trans. ISIJ*, vol. 24, no. April 1983, pp. 648–654, 1984.
- [39] M. Calcagnotto, D. Ponge, and D. Raabe, "Effect of grain refinement to 1 μ m on strength and toughness of dual-phase steels," *Mater. Sci. Eng. A*, vol. 527, no. 29–30, pp. 7832–7840, 2010.
- [40] R. G. Davies, "On the ductility of dual phase steels," *Formable HSLA Dual-Phase Steels*, pp. 25–39, 1979.
- [41] E. Hornbogen, "Microstructure and Mechanisms of Fracture," *Strength Met. Alloy.*, pp. 1059–1073, 1982.
- [42] A. Pineau, A. A. Benzerga, and T. Pardoen, "Failure of metals I: Brittle and

- ductile fracture,” *Acta Mater.*, vol. 107, pp. 424–483, 2016.
- [43] D. François, A. Pineau, and A. Zaoui, *Mechanical Behaviour of Materials, solid mechanics and its applications*, vol. 191. Dordrecht: Springer Netherlands, 2013.
- [44] R. Song, D. Ponge, D. Raabe, J. G. Speer, and D. K. Matlock, “Overview of processing, microstructure and mechanical properties of ultrafine grained bcc steels,” *Mater. Sci. Eng. A*, vol. 441, no. 1–2, pp. 1–17, 2006.
- [45] V. V. Stolyarov, Y. T. Zhu, T. C. Lowe, R. K. Islamgaliev, and R. Z. Valiev, “Two step SPD processing of ultrafine-grained titanium,” *Nanostructured Mater.*, vol. 11, no. 7, pp. 947–954, 1999.
- [46] R. Song, D. Ponge, D. Raabe, and R. Kaspar, “Microstructure and crystallographic texture of an ultrafine grained C-Mn steel and their evolution during warm deformation and annealing,” *Acta Mater.*, vol. 53, no. 3, pp. 845–858, 2005.
- [47] R. Song, D. Ponge, and D. Raabe, “Improvement of the work hardening rate of ultrafine grained steels through second phase particles,” *Scr. Mater.*, vol. 52, no. 11, pp. 1075–1080, 2005.
- [48] S.-H. Joo, J. K. Lee, J.-M. Koo, S. Lee, D.-W. Suh, and H. S. Kim, “Method for measuring nanoscale local strain in a dual phase steel using digital image correlation with nanodot patterns,” *Scr. Mater.*, vol. 68, no. 5, pp. 245–248, 2013.
- [49] M. Grédiac, F. Hild, A. Pineau, and A. Pineau, *Full-Field Measurements and Identification in Solid Mechanics*. UK and USA: ISTE Ltd and John Wiley & Sons, Inc. Apart, 2012.
- [50] B. Pan, K. Qian, H. Xie, and A. Asundi, “Two-dimensional digital image correlation for in-plane displacement and strain measurement: A review,” *Meas.*

- Sci. Technol.*, vol. 20, no. 6, 2009.
- [51] N. McCormick and J. Lord, “Digital image correlation,” *Mater. Today*, vol. 13, no. 12, pp. 52–54, 2010.
- [52] Y. Wang and A. M. Cuitio, “Full-field measurements of heterogeneous deformation patterns on polymeric foams using digital image correlation,” *Int. J. Solids Struct.*, vol. 39, no. 13–14, pp. 3777–3796, 2002.
- [53] W. H. Peters and W. F. Rason, “Digital imaging techniques in experimental stress analysis,” *Opt. Eng.*, vol. 21, no. 3, 1982.
- [54] M. Sutton, W. Wolters, W. Peters, W. Ranson, and S. McNeill, “Determination of displacements using an improved digital correlation method,” *Image Vis. Comput.*, vol. 1, no. 3, pp. 133–139, 1983.
- [55] U. Manual, *ARAMIS User Manual*, V6.1. GOM, 2007.
- [56] “GOM Optical Measuring Technologies,” *ARAMIS User Man. - Hardw.*, 2001.
- [57] A. Giachetti, “Matching techniques to compute image motion,” *Image Vis. Comput.*, vol. 18, pp. 247–60, 2000.
- [58] B. Pan, H. M. Xie, B. Q. Xu, and F. L. Dai, “Performance of sub-pixel registration algorithms in digital image correlation,” *Meas. Sci. Technol.*, vol. 17, no. 6, pp. 1615–1621, 2006.
- [59] J. Kang, Y. Ososkov, J. D. Embury, and D. S. Wilkinson, “Digital image correlation studies for microscopic strain distribution and damage in dual phase steels,” *Scr. Mater.*, vol. 56, no. 11, pp. 999–1002, 2007.
- [60] A. D. Kammers and S. Daly, “Small-scale patterning methods for digital image correlation under scanning electron microscopy,” *Meas. Sci. Technol.*, vol. 22, no. 12, 2011.
- [61] J. Kang, M. Jain, D. S. Wilkinson, and J. D. Embury, “Microscopic Strain Mapping Using Scanning Electron Microscopy Topography Image Correlation

- at Large Strain,” *J. Strain Anal. Eng. Des.*, vol. 40, no. 6, pp. 559–570, 2005.
- [62] H. Jin, W.-Y. Lu, and J. Korellis, “Micro-scale deformation measurement using the digital image correlation technique and scanning electron microscope imaging,” *J. Strain Anal. Eng. Des.*, vol. 43, no. 8, pp. 719–728, 2008.
- [63] M. A. Sutton, J.-J. Orteu, and H. Schreier, “Image correlation for shape, motion and deformation measurements: Basic Concepts, Theory and Applications,” *Springer*, 2009.
- [64] A. D. Kammers and S. Daly, “Digital Image Correlation under Scanning Electron Microscopy: Methodology and Validation,” *Exp. Mech.*, vol. 53, no. 9, pp. 1743–1761, 2013.
- [65] M. A. Sutton, N. Li, D. C. Joy, A. P. Reynolds, and X. Li, “Scanning electron microscopy for quantitative small and large deformation measurements Part I: SEM imaging at magnifications from 200 to 10,000,” *Exp. Mech.*, vol. 47, no. 6, pp. 775–787, 2007.
- [66] C. P. Scott, F. Fazeli, B. Shalchi Amirkhiz, I. Pushkareva, and S. Y. P. Allain, “Structure-properties relationship of ultra-fine grained V-microalloyed dual phase steels,” *Mater. Sci. Eng. A*, vol. 703, no. July, pp. 293–303, 2017.
- [67] ASTM, “Standard Test Methods for Determining Average Grain Size Using Semiautomatic and Automatic Image Analysis,” *ASTM Int.*, vol. 97, pp. 1–24, 2015.
- [68] ASTM, “Standard Test Method for Determining Volume Fraction by Systematic Manual Point Count,” *Practice*, no. C, pp. 1–7, 2011.
- [69] C. Scott, “Unpublished work by present authors.” 2018.
- [70] P. J. Goodhew, J. Humphreys, and R. Beanland, *Electron Microscopy and Analysis - Third Edition*. London and New York: Taylor & Francis, 2001.
- [71] N. E. Dowling, *Mechanical Behavior of Materials*. 2013.

- [72] C. P. Scott, B. Shalchi, F. Fazeli, I. Pushkareva, S. Y. P. Allain, and H. Azizi, “New Insights into Martensite Strength and the Damage Behaviour of Dual Phase Steels .”
- [73] M. Delincé, P. J. Jacques, and T. Pardoen, “Separation of size-dependent strengthening contributions in fine-grained Dual Phase steels by nanoindentation,” *Acta Mater.*, vol. 54, no. 12, pp. 3395–3404, 2006.
- [74] T. O. and K. T. A. L. Zhang, “Application of Nanoindentation Technique in Martensitic Structures,” in *Nanoindentation in Materials Science*, 2012, pp. 109–130.
- [75] E. J. Pavlina and C. J. Van Tyne, “Correlation of Yield strength and Tensile strength with hardness for steels,” *J. Mater. Eng. Perform.*, vol. 17, no. 6, pp. 888–893, 2008.
- [76] M. Calcagnotto, Y. Adachi, D. Ponge, and D. Raabe, “Deformation and fracture mechanisms in fine- and ultrafine-grained ferrite/martensite dual-phase steels and the effect of aging,” *Acta Mater.*, vol. 59, no. 2, pp. 658–670, 2011.
- [77] J. S. P Buessler, O Bouaziz, T LUNG, “Modelling of mechanical properties and local deformation of high- strength multi-phase steels,” in *ECSC Steel RTD Programme Report*, 2000.
- [78] M. Sutton, C. Mingqi, W. Peters, Y. Chao, and S. McNeill, “Application of an optimized digital correlation method to planar deformation analysis,” *Image Vis. Comput.*, vol. 4, no. 3, pp. 143–150, 1986.
- [79] G. Vendroux and W. G. Knauss, “Submicron deformation field measurements: Part 2. Improved digital image correlation,” *Exp. Mech.*, vol. 38, no. 2, pp. 86–92, 1998.
- [80] J. Kadkhodapour, S. Schmauder, D. Raabe, S. Ziaei-Rad, U. Weber, and M. Calcagnotto, “Experimental and numerical study on geometrically necessary

dislocations and non-homogeneous mechanical properties of the ferrite phase in dual phase steels,” *Acta Mater.*, vol. 59, no. 11, pp. 4387–4394, 2011.

- [81] N. Kamikawa, M. Hirohashi, Y. Sato, E. Chandiran, G. Miyamoto, and T. Furuhashi, “Tensile Behavior of Ferrite-Martensite Dual Phase Steels with Nano-Precipitation of Vanadium Carbides,” *ISIJ Int.*, vol. 55, no. 8, pp. 1781–1790, 2015.